Fall 2018

BIOPHYSICAL PROPERTIES OF AN ANTIFREEZE PROTEIN AND THE EFFECTS OF IONIC LIQUIDS ON THE MODEL PROTEIN GB1

Korth Wade Elliott
University of New Hampshire, Durham

BIOPHYSICAL PROPERTIES OF AN ANTIFREEZE PROTEIN AND THE EFFECTS OF IONIC LIQUIDS ON THE MODEL PROTEIN GB1

BY

KORTH WADE ELLIOTT

Bachelor of Science in Chemistry, Eastern Oregon University, 2010

DISSERTATION

Submitted to the University of New Hampshire

in Partial Fulfillment of

the Requirements for the Degree of

Doctor of Philosophy

in

Biochemistry

September 2018

This thesis has been examined and approved in partial fulfillment of the requirements for the degree of Doctor of Philosophy in Biochemistry by:

Thesis Director, Dr. Krisztina Varga, Assistant Professor of Biochemistry

Dr. Richard H. Cote, Professor and Chair of Molecular, Cellular & Biomedical Sciences

Dr. Feixia Chu, Associate Professor of Biochemistry

Dr. John G. Tsavalas, Associate Professor of Chemistry and Materials Science

Dr. Marc A. Boudreau, Assistant Professor of Chemistry

On July 26, 2018

Original approval signatures are on file with the University of New Hampshire Graduate School.

DEDICATION

I would like to dedicate the thesis to my wife, Danielle, and thank her for all her love, patience and support throughout the course of my graduate education. None of this would have been possible without her. I would also like to thank my parents, Korth and Joan, and my siblings, Chris, Nicola and Rashe, for their continued love and support. I would also like to thank my college advisor, Dr. Jeff Woodford, for getting me interested in research early on. I would also like to thank my friends Joe and Franzi for their support and friendship.

ACKNOWLEDGEMENTS

I would thank my advisor, Dr. Kriszitna Varga, first and foremost for her guidance throughout the entirety of this project and my time as a graduate student. I have been fortunate to have an advisor who is both patient and ambitious to help keep me focused and on track. I would like to also thank my committee members, Dr. Rick Cote, Dr. Feixia Chu, Dr. John Tsavalas and Dr. Marc Boudreau, for their participation, flexibility with their time and being so accommodating throughout this process.

I would like to acknowledge former Varga group members, Dr. Suzanne Farver Lukjan and Dr. Shelby Follett, their input and help with the project. I would like to thank Mr. Christopher Nordyke and Ms. Colleen Ricci for their assistance in the initial stages of the antifreeze protein expression and purification. I would also like to thank Dr. Pei Zhang for her help with the collection of AFP thermal hysteresis data. I would like acknowledge Mr. Jon Sreter and Ms. Katarina Jovic for their help the project.

Finally, I would like to thank the following collaborators for their help with this research: Dr. John Tsavalas (thermal hysteresis data collection) at the University of New Hampshire, Dr. James Aramini (AFP NMR) at the City University of New York, Dr. Daniel Levy and Dr. Predrag Jevtic (cryopreservation of frog eggs) at the University of Wyoming, Dr. Irena Kratochvilova (cryopreservation of human skin fibroblasts) at the Academy of Sciences of the Czech Republich, Dr. Lisa Warner (ionic liquid NMR) at Boise State University, Dr. Erica Gjersing (ionic liquid NMR) at Los Alamos National Laboratory and Dr. Sergei Dzyuba (ionic liquid synthesis) at Texas Christian University.

This research supported in part by grants from the National Science Foundation (CHE-1740399 and DGE-0948027), the National Institute of General Medical Sciences

at the National Institutes of Health (P20GM103432) and the National Aeronautics and Space Administration’s Established Program to Stimulate Competitive Research (80NSSC18M0034).

Table of Contents

LIST OF FIGURES

LIST OF TABLES

ABSTRACT

BIOPHYSICAL PROPERTIES OF AN ANTIFREEZE PROTEIN AND THE EFFECTS OF IONIC LIQUIDS ON THE MODEL PROTEIN GB1

by

Korth Wade Elliott

University of New Hampshire, September 2018

Antifreeze proteins (AFPs) are a unique class of protein characterized by their ability to depress the freezing point of water sufficient to prevent the formation of ice crystals by adsorbing to the surface of ice crystals. This unique ability allows organisms (e.g. plants, fish, insects, etc.) which live in extremely cold climates to survive. Because of these proteins' ability to prevent and slow the rate of ice crystal formation, they have great potential in the application of cryopreservation in medicine, agriculture and food science. Antifreeze proteins have been known for over five decades, however, their exact mechanism of action is still under investigation. In this study, we have characterized the antifreeze protein *Ap*AFP752 from the beetle *Anatolica polita* to better understand method of action of antifreeze activity of insect antifreeze proteins and to identify it potential applications in cryoprotection. We found the protein to have a β-helix secondary structure, similar to other known insect antifreeze proteins. Additionally, the protein was found to confer some cryoprotection to cellular systems.

We have also investigated the effects of ionic liquids on protein biophysics. Ionic liquids are highly viscous liquids at room temperature comprised entirely of ions, which makes it challenging to study their interactions with protein by traditional NMR methods. It has been proposed that ILs can be tuned to alter the structural and biophysical

properties of biomacromolecules. In this study, the effect of an ionic liquid (1-butyl-3-methylimidazolium bromide, [C_4-mim]Br) on the structure and dynamics of the model protein GB1 was investigated using high-resolution magic angle spinning (HR-MAS) NMR spectroscopy. HR-MAS NMR proved to be a viable tool for the elucidation of the molecular mechanism of ionic liquid – protein interactions.

PROJECT AIMS AND HYPOTHESIS

This thesis can be divided into two projects, and the aims are summarized here:

Project I. Characterization of the antifreeze protein ApAFP752

Effective cryoprotection is an important unsolved practical problem in medicine, the pharmaceutical and food industries, and agriculture. Nature employs a variety of compounds and strategies for freeze avoidance and freeze tolerance that enhance the survival of certain organisms in extreme cold environments. Antifreeze proteins are produced in certain types of fish, insects, bacteria, and plants that live in cold climates and contribute to their resistance to freezing. Antifreeze proteins are thought to irreversibly bind to the surface of ice crystals and inhibit their growth. The exact mechanism of ice-binding and ice-growth inhibition at the molecular level is not fully understood despite considerable efforts over the past decades. This is an important problem, as the lack of understanding of ice-binding and ice-growth inhibition has hindered development of effective cryoprotection techniques and applications of antifreeze proteins.

In order to contribute to a better fundamental understanding of ice binding and ice-growth inhibition and potential applications of antifreeze proteins, we have set out to structurally characterize a hyperactive antifreeze protein, ApAFP752, from the beetle *Anatolica polita* and test its potential as a cryopreservation agent. While the best studied class of antifreeze proteins are from fish (as these were discovered first in the 1960s), insect antifreeze proteins have very different structures and thermal hysteresis, ice recrystallization, and ice crystal shaping activities, which offer different potential for their applications. The goals of the project were accomplished in the following specific aims:

Aim 1: Structural characterization of ApAFP752 antifreeze protein by solution NMR spectroscopy. We hypothesized that the structure of ApAFP752 would show good surface complementarity to ice.

Aim 2: Investigate the cryoprotective mechanism ApAFP752 in live cells. Our hypothesis was that ApAFP752 can confer cryoprotection to live cells that are otherwise sensitive to freezing.

Project II. Ionic liquid interactions with proteins

Ionic liquids are synthetic materials comprised entirely of ions with phase transitions at or below room temperature. Recent reports have described the ability of ionic liquids to modulate intermolecular and intramolecular interactions of small molecules. Ionic liquids offer unique environments that can be tuned to alter the structural and biophysical properties of biomacromolecules. To advance the fundamental understanding of how ionic liquids influence native protein secondary structure and function, we have chosen to study the effect of 1-butyl-3-methylimidazolium bromide ([C4-mim]Br) on the structure of GB1, an immunoglobulin binding domain B1 of streptococcal protein G. Due to the inherent difficulties of studying proteins in highly viscous media by solution NMR, we have utilized high resolution magic angle spinning (HR-MAS) NMR spectroscopy, which can reduce NMR linewidths in semi-solid samples through the application of magic angle spinning (MAS). We were also motivated to use this as a test case to probe whether HR-MAS could be used for studying an antifreeze protein (Project I) in viscous environment (e.g. live cells). The goals of the project were accomplished in the following specific aims:

Aim 1: Utilize high resolution magic angle spinning (HR-MAS) NMR spectroscopy to characterize a protein site specifically in highly viscous environment. We hypothesized that HR-MAS NMR spectroscopy was a viable tool to study proteins at the atomic level in a highly viscous environment.

Aim 2: Investigate whether ionic liquids have the ability to stabilize protein fold. We hypothesized that the ionic liquid [C4-mim]Br could stabilize structure of the GB1 protein.

CHAPTER 1

INTRODUCTION TO ANTIFREEZE PROTEINS

Antifreeze proteins (AFPs) are a subset of ice binding proteins that have the capacity to depress the freezing point of liquid water and prevent the formation of and growth of ice crystals. The formation of ice crystals in biology can be harmful to organisms and can result cellular death. Antifreeze proteins have the ability to mitigate the damaging effects of ice by preventing ice crystals from expanding past the point of a microcrystal. Antifreeze proteins have been discovered in numerous species of plants, animals, insects, fungi and bacteria, enabling them to survive in very cold temperatures[1,2]. Organisms that have AFPs are classified as freeze tolerant or freeze avoidant[3-5]. Freeze tolerant organisms are those that can survive ice formation in their extracellular fluids. Freeze avoidant organisms are organisms that can survive in freezing conditions but do not survive formation of ice in their cells. These adaptive mechanisms have ensured the survival of species that live in areas of extreme cold or have climates with enormous temperature fluctuations within a single day. Because of AFPs' ability to lower the freezing point of water, this class of protein has become an area of increased interest within the scientific community. The potential applications for this class of protein span a large spectrum, ranging from food science to agro-science to medicine[6-10].

The first antifreeze protein discovered was an antifreeze glycoprotein (AFGP) in 1960s by Art DeVries[11]. It was discovered in Antarctic Notothenioids (winter flounder). Several other AFPs have since been identified throughout the world. While each of these

antifreeze proteins has a similar function, there is a remarkable amount of sequence and structural diversity among these proteins. This diversity is due to antifreeze proteins evolving independently of each other. Antifreeze proteins have been subclassified according to their sequence homology and thermal hysteresis properties.

I. Fish Antifreeze Proteins

Fish antifreeze proteins are the most studied class of antifreeze protein and can be subclassified as types I, II, III, IV and antifreeze glycoproteins. Type I antifreeze proteins are most commonly found in arctic and Antarctic fish (see Figure 1A). The HPLC6 isoform of the winter flounder was the first AFP to have its atomic structure determined. Type I antifreeze proteins are typically small, α-helical proteins[12]. They contain three repeats comprised of Thr-Ala-Ala-X-Ala-X-X-Ala-Ala-X-X, where X represents any given amino acid[13,14]. This series of repeats is quite significant with respect to its ice binding mechanism[15].

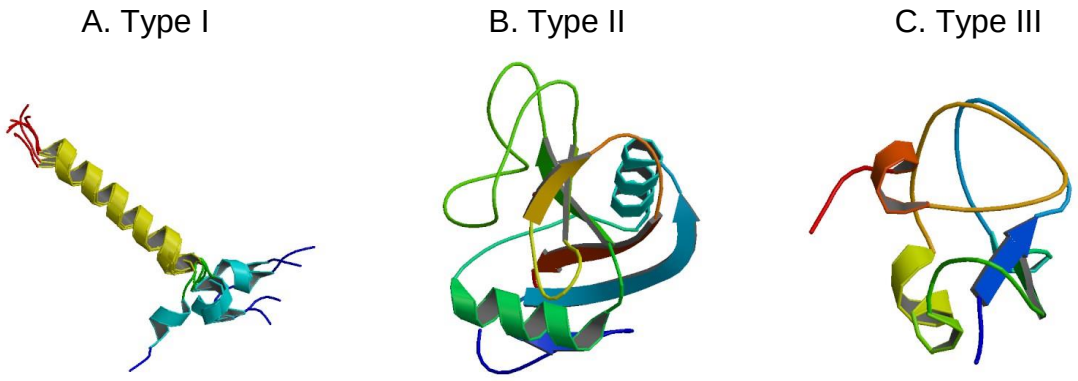

Figure 1: Antifreeze proteins have very broad structural diversity due to their independent evolutionary roots. They are classified into subgroups based on their structure. Here we show an example of type I AFP from sculpin[16] (A), type II AFP from longsnout poacher[17] (B), type III AFP from eel pout[18] (C).

Type II antifreeze proteins are another subset of AFPs commonly found in fish (see Figure 1B). These proteins are typically larger than their type I counterpart, averaging a size of approximately 20-kDa. It has been found that some type II AFPs (those that contain Ca^{2+}) have a high homology to the carbohydrate recognition domain of lectins, which use Ca^{2+} to bind sugars[19]. This subtype of AFP was the first type discovered to have disulfide bonds. Since then other subtypes of AFP have been discover which also contain disulfide bonds[14]. Type II AFPs have been found to contain a combination of α-helix and β-sheet residues.

Type III antifreeze proteins are a subset of AFPs which contain very little sequence similarities within its own subtype (see Figure 1C). They are also commonly found in fish. Currently there has been no identified sequence associated with the ice binding surface of the protein[14,20,21]. It has been found that type III antifreeze proteins contain a combination of α-helix and β-sheet residues. Type IV antifreeze proteins have been identified in fish. They are thought to contain four amphipathic α-helices folded into a four-helix bundle. These proteins have been found to have sequence similarities to plasma apolipoproteins and also have a similar helix bundle structure[14]. However, due to the concentration of type IV AFPs found in the blood of fish and their differences in expression pathway from apolipoproteins, type IV AFPs are distinct from apolipoproteins[22].

Antifreeze glycoproteins (AFGPs) were the first ice-binding proteins found in fish. AFGPs are classified according to their size with AFGP1 being the longest and AFGP8 being the shortest with their relative molecular masses ranging from 33.7-kDa to 2.6-kDa. All AFGPs consist of repeats of Ala-Ala-Thr joined with the disaccharide β-D-

galactopyranosyl-(1,3)α-*N*-acetyl-D-galactosamine at the hydroxyl oxygen of the Thr residue[14,23] (see Figure 2).

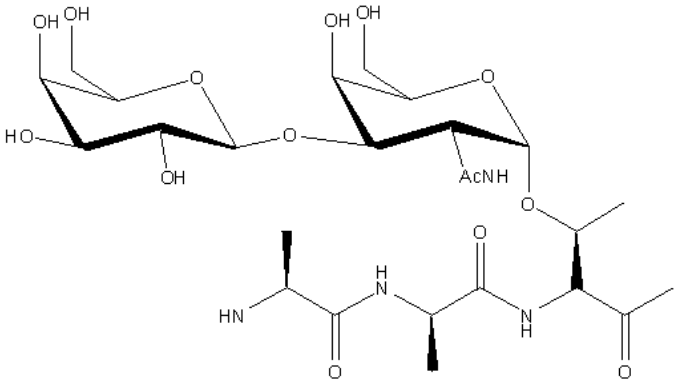

Figure 2: Typical antifreeze glycoprotein chemical formula depicting the AAT repeats joined with a dissacharide[14].

II. Insect Antifreeze Proteins

Insect antifreeze proteins are a more recently discovered subtype of AFP. These proteins are typically small proteins around 9-kDa in size. The most extensively studied insect antifreeze protein is found in the beetle *Tenebrio molitor* (yellow fire beetle)[24-26]. It has been found that insect AFPs are primarily hyperactive, meaning that they can depress the freezing point of water further than the average antifreeze protein[27]. These proteins are known to have a series of Thr-Cys-Thr repeats where the cysteine residues are disulfide bonded creating a β-helix and the threonine residues point outward to interact with water[28].

III. Plant Antifreeze Proteins

Plant antifreeze proteins are a less well studied subset of antifreeze proteins. There are currently two well studied plant AFPs: *Lolium perenne* (LpAFP) and *Dacus*

carrotova (DcAFP)[14,29]. While these two antifreeze proteins have been discovered in plants, they contain very different sequences associated with ice binding. LpAFP contains repeats of X-X-Asn-X-Val-X-Gly. The current model for this protein is a β-roll containing an additional sequence repeat of Thr-X-Thr similar to that of insect AFPs. Even though this protein contains similarities to insect AFPs, the Thr-X-Thr repeat is not as well conserved in LpAFP.

DcAFP is a leucine rich antifreeze protein. It contains a repeat of the following twenty-four residues: Pro-X-X-X-X-X-Leu-X-X-Leu-X-X-Leu-X-Leu-Ser-X-Asn-X-Leu-X-Gly-X-Ile. The structure of this protein is comprised of a ten coil β-helical folds consisting of two β-strands and a 3_{10} helix[14]. This results in a structure similar to an insect AFP β-helix. Unlike most β-helical AFPs, this protein contains multiple highly conserved Asn residues between the β-strands indicating that the ice binding surface is opposite to the flat surface of the protein.

IV: Thermal Hysteresis Glycolipids

Some organisms have developed adaptive mechanisms outside of producing antifreeze proteins in order to survive freezing temperatures. The beetle *Upis ceramboides* produces glycolipids and polyols as its primary mechanism of freeze tolerance[30]. These biomolecules are found in high concentrations in the hemolymph of this beetle during periods of cold temperature. Similar thermal hysteresis glycolipids have also been found in other organisms including insects, fish and frogs[23].

V: Antifreeze Protein Properties

All antifreeze proteins have the same three properties: thermal hysteresis activity, ice crystal shaping and ice recrystallization inhibition activity. The extent of these properties varies among and within AFP classes. Antifreeze proteins have also been commonly referred to as thermal hysteresis proteins. Thermal hysteresis is defined as the difference between a sample's freezing point and melting point (Figure 3)[1,27]. AFPs inhibit the growth of ice crystals by decreasing the freezing point of water, creating a gap between the freezing point and melting point of water. The magnitude of thermal hysteresis is used to qualify an antifreeze protein as either moderately active or hyperactive[1,31].

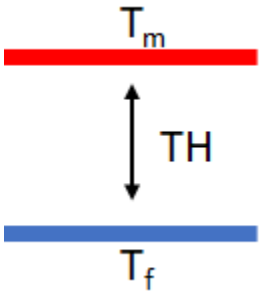

$$TH = T_m - T_f$$

Figure 3: Thermal hysteresis (TH) is defined as the difference between the melting point (T_m) and the freezing point (T_f) of water. This property is different from freezing point depression associated with salts, where salt freezing point depression is a function of osmolarity.

Though AFPs' thermal hysteresis activities are quantitatively characterized, the activity of these proteins can be correlated to their ice binding mechanisms and the planes of ice to which the protein binds. Ice contains two planes, the basal and prism planes (Figure 4).

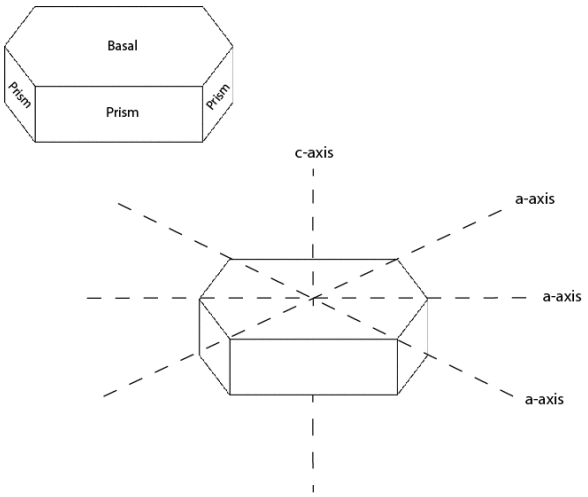

Figure 4: A representation of the planes of ice. Each plane is affiliated with a designated axis.

Antifreeze proteins bind to the surface of ice and mechanically prevent additional waters from attaching to the ice crystal's surface. The plane or planes to which the AFP binds dictates the shape the ice crystal will take. Moderate antifreeze proteins bind to the prism surface of ice along the *c*-axis. This results in the formation of a single bipyramidal ice crystal (Figure 5A). Hyperactive antifreeze proteins bind to the basal and prism surfaces of ice along the *a*-axis and *c*-axis[32]. This binding results in the formation of a single hexagonal disc or lemon shaped ice crystal (Figure 5B)[31,33-35]. The formation of these single micro crystals is essential in the prevention of the growth of ice crystals and is the primary mechanism by which antifreeze proteins prevent the formation of larger ice crystals. Due to the binding characteristics of these proteins, Moderate antifreeze proteins, such as many fish AFPs, require 10 to 100 times the protein concentration to achieve the same thermal hysteresis activity as their hyperactive AFP counterparts[31,36].

A B

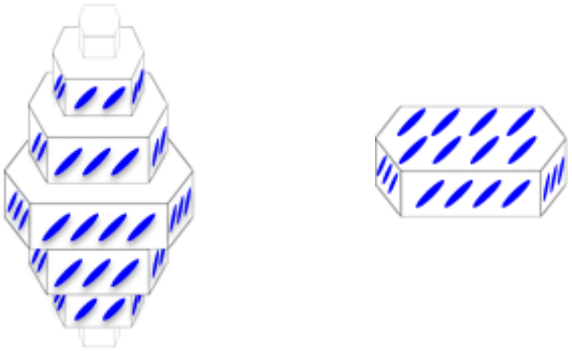

Figure 5: Ice crystal shaping effects of antifreeze proteins. (A) Moderate active antifreeze protein binding along the c-axis of ice resulting in a hexagonal bipyramidal crystal shape. (B) Hyperactive antifreeze protein binding along both the a- and c-axes of ice resulting in a hexagonal disk crystal shape.

Antifreeze proteins are thought to irreversibly bind to the surface of ice[27]. Because of this characteristic, AFPs can prevent the fusion of smaller ice crystals into larger ice crystals during melting. This ability to prevent this fusion from occurring is known as ice recrystallization inhibition. This property is extremely important when considering cells that experience freeze/thaw cycles[37]. As cells thaw small ice crystals fuse together resulting in larger ice crystals, which results in an increase in intracellular pressure. This increase in pressure can damage cellular components rendering the cell non-viable. An AFPs ice recrystallization inhibition properties help to prevent this occurrence[27].

VI: Ice Binding Theories

Over the years there have been many theories as to the exact mechanism of action behind antifreeze protein ice binding. Initially, it was thought that hydrogen bonding was the culprit behind AFP ice binding. As previously stated, type I antifreeze proteins contain

repeats comprised of Thr-Ala-Ala-X-Ala-X-X-Ala-Ala-X-X[13]. Studies found the distance between the hydroxyl groups in the Thr residues in these repeats is 16.5 Å and the distance between the oxygen atoms in the water molecules in the ice plane is 16.7 Å[14]. Due to how close these two distances are, it was assumed that the Thr hydroxyls in the AFP and the oxygen atoms in water molecules aligned properly to facilitate a strong hydrogen bonding interaction, thus creating an ice binding interface.

It has since been demonstrated that hydrogen bonding is not solely responsible for AFP ice binding. A series of point mutation studies performed on type I antifreeze proteins showed that hydrogen bonding plays a much smaller role in ice binding than originally thought[14,38]. This was demonstrated by inserting Ser residues in place of the Thr residues in order to mimic the hydrogen bonding capabilities[14]. The study showed that this mutation resulted in an almost complete loss of antifreeze activity. Additional studies were performed substituting amino acids containing hydrophobic side chains in place of the Thr residues. Unexpectedly, the substitutions with Ala and Val both resulted in a very small loss of thermal hysteresis activity[13,39]. These studies showed that the presence of hydrogen bonding capable residues was much less important than originally assumed and showed that the presence of hydrophobic residues may play a significant role in ice binding and antifreeze activity. This theory was further substantialized by the study of type III antifreeze proteins which demonstrated that hydrophobic residues are not solely responsible for the thermal hysteresis activity, but they are additive to the thermal hysteresis properties due to van der Waals forces[14].

Currently the most accepted theory behind the ice binding mechanism of antifreeze proteins is the anchored clathrate model. In this theory, ice-like waters form a clathrate

(also known as a water cage) around the γ-methyl of the Thr residues. This clathrate is anchored to the protein via hydrogen bonds to the main chain nitrogen atoms and the hydroxyl groups on the Thr residues. The clathrate creates a quasi-liquid membrane around the protein which binds to the ice surface and allows the protein to prevent further growth of the ice crystal[31,40,41]. The proposed spacing of the Thr hydroxyls in the insect antifreeze protein ApAFP752 compared to the spacing of water molecules in ice lends further evidence to the importance of the position of the Thr in antifreeze proteins activity as the TCT spacing between the neighboring Thr are 4.5 Å along the a-axis plane of ice and the TCT spacing between adjacent Thr is 7.5 Å along the c-axis, both of which are ideal matches to the spacing of water molecules in ice[35].

VII: ApAFP752

The Varga lab is currently studying the antifreeze protein ApAFP752 (Figure 6A). ApAFP752 is an 8.9-kDa hyperactive insect antifreeze protein found in the desert beetle *Anatolica polita*. *A. polita* is found in the Xinjiang province of China in the Gurbantunggut Desert as well as other part of central Asia. This area of the world has temperatures that can fluctuate up to 40 °C in a single day with temperatures reaching as low as -40 °C[35,42,43]. These climate pressures have resulted in an antifreeze protein with very high thermal hysteresis activity. The activity of this protein as a fusion protein has been previously demonstrated with the use of differential scanning calorimetry. Similar to other insect antifreeze proteins, ApAFP752 is thought to have a β-helical secondary structure (Figure 6B). This protein is thought to be a right-handed parallel β-helix consisting of six repetitive 12-amino acid loops. It has very high homology to the well-studied antifreeze

protein from the beetle *Tenebrio molitor* (TmAFP) which is also a β-helical protein[25]. Like other insect antifreeze proteins, ApAFP752 contains repeats of Thr-X-Thr, where X is a cysteine residue. These cysteine residues are disulfide bonded to create the flat ice binding surface necessary for the protein's thermal hysteresis activity.

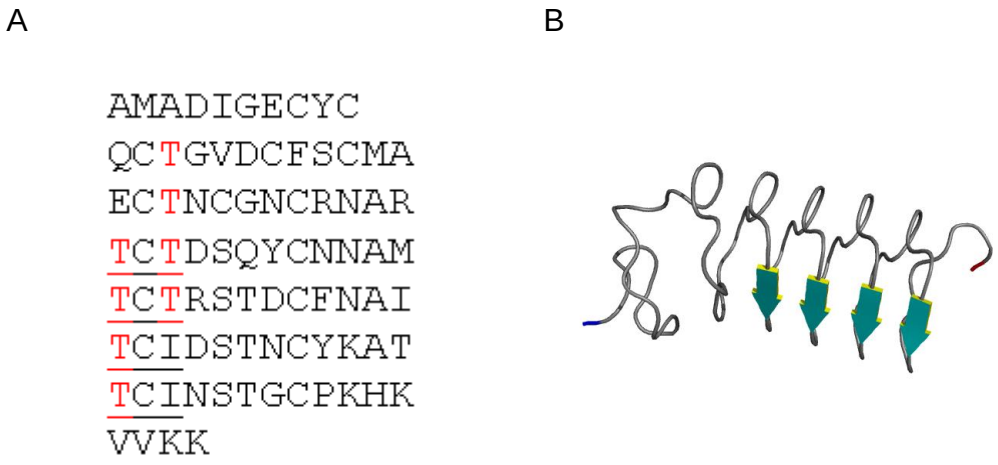

Figure 6: (A) Sequence of ApAFP752. (B) Representation of a protein having a β-helix secondary structure. Threonines are highlighted in red indicating the potential ice-binding surface.

The gene coding for the ApAFP752 protein sequence was cloned into an *E. coli* expression vector, and the antifreeze protein was expressed and purified as a fusion protein with thioredoxin-A (TrxA), termed TrxA-ApAFP752, in all prior literature reported studies[35,43,44]. TrxA participates in the catalysis of dithiol-disulfide exchange reactions[45]. In our work, we have chosen to work both with the TrxA-ApAFP752 fusion protein and ApAFP752 (without the TrxA fusion partner). In the following chapters, we will describe the characterization of the antifreeze activity of both proteins, the structural characterization of ApAFP752 by nuclear magnetic resonance (NMR) spectroscopy, and the application of the TrxA-ApAFP752 fusion protein in cryopreservation studies.

CHAPTER 2

EXPRESSION AND PURIFICATION OF ApAFP752

The expression and purification of the ApAFP752 joined with thioredoxin (Trx) as a fusion protein (TrxA-ApAFP752) was reported in the literature by Ji Ma and coworkers at Xinjiang University[35,43,44], and the initial expression of this protein was carried out in the Varga lab in accordance with previously published reports[35,43,44]. While utilization of the published method did result in the expression of the fusion protein, in order to carry out nuclear magnetic resonance (NMR) spectroscopy and cryopreservation studies, the ApAFP752 protein must be available in milligram quantities and in high purity. For NMR structural studies, the protein also had to be enriched with NMR active isotopes (*e.g.* ^{13}C and ^{15}N) and the expression was established in minimal medium. The protocols were optimized in order to maximize the yield and purity of the fusion protein utilizing various *E. coli* cell lines and purification protocols.

While the fusion protein was reported to have antifreeze activity[35,43,44], our aim was also to characterize the ApAFP752 without the thioredoxin fusion, which was not published before and proved to be experimentally challenging. We have explored different routes for producing pure ApAFP752, including the expression and purification of ApAFP752 (without the TrxA fusion) and also the cleavage of purified TrxA-ApAFP752 followed by a purification step. The protein is challenging to be expressed in *E. coli* because of the high number of Cys residues, and we were unable to produce well-folded

ApAFP752 when expressed without the TrxA fusion. We were successful however to produce ApAFP752 by cleaving the purified purified TrxA-ApAFP752.

I. Optimization of the expression of TrxA-APAFP752 fusion protein

Optimization of *E. coli* cell line for the expression of TrxA-ApAFP752 fusion protein

The recombinant plasmid, pET32a-*Apafp752*, for the fusion protein TrxA-ApAFP752 was a gift from Ji Ma at Xinjiang University[35,43,44]. As previously stated, TrxA-ApAFP752 is thought to be a heavily disulfide bonded β-helix containing 16 Cys residues. Because of the high number of suspected disulfide bonds, various *E. coli* strains were tested in order to identify the one best suited for this protein. While *E. coli* strains such as BL21 (DE3) pLysS are commonly used for recombinant protein expression, they are not typically well suited for proteins with a high number of disulfide bonds. To address this, the following *E. coli* strains were each tested individually to assess their proficiency in expressing and folding the protein: BL21 (DE3) pLysS (Promega), Rosetta-gami™ 2(DE3) (Novagen) and Origami™ B(DE3) (Novagen). Rosetta-gami™ 2(DE3) and Origami™ B(DE3) were tested because their claimed increased capacity for expressing and folding disulfide bonded proteins. The transformed cells were plated onto Luria-Bertani medium agar plates containing 100 μg mL^{-1} ampicillin and incubated at 37 °C overnight for 14 hours. 30 mL cultures of Luria-Bertani (LB) medium (Fisher Scientific) containing 100 μg mL^{-1} ampicillin were inoculated each with a single transformed colony and cultured overnight in an orbital shaker at 37 °C, 225 rpm for 12 hours. 4 mL of the overnight culture was transferred into 1 L of fresh LB medium and grown in an orbital shaker at 37 °C, 225 rpm until the optical density at 600 nm (OD_{600}) reached 0.65 to 0.70. The OD_{600} was measured

using an Agilent 8453 UV-Vis spectrometer. Once the specified OD_{600} was reached, the transformed cells were harvested via centrifugation at 9559 x *g*, 4 °C for 20 minutes. The cells were resuspended in a minimal growth medium containing ^{15}N enriched (>99%) ammonium chloride (NH_4Cl) at a 1:1 LB broth to minimal growth medium. The cells were then incubated at 25 °C, 225 rpm for 45 minutes. Overexpression of the protein was induced with the addition 1 mL of 400 mM (final concentration 0.4 mM) isopropyl β-D-1-thiogalactopyranoside (IPTG) and incubated at 25 °C, 225 rpm for 8 hours[46]. The cells were harvested via centrifugation at 9559 x *g*, 4 °C for 25 minutes. The cell pellets were either used right away or frozen at -80 °C for long term storage.

Purification of TrxA-AFP752 fusion protein

The cell pellets were resuspended in a lysis buffer containing 50 mM sodium phosphate, 150 mM NaCl, 1% v/v Halt™ Protease Inhibitor Cocktail (Thermo Scientific), pH 8.0. The cells were lysed four times via French Press at 1500 psi. The lysate was centrifuged at 20,217 x *g*, 4 °C for 30 minutes and the supernatant was then collected. Fast protein liquid chromatography (FPLC; GE Healthcare ÄKTA purifier 900) was performed in duplicate using Ni-affinity columns to take advantage of the 6xHis tag engineered into the protein sequence. The protein was eluted from the FPLC using 500 mM imidazole and dialyzed into a buffer containing 50 mM potassium phosphate, 20 mM NaCl, pH 8.0.

Fast protein liquid chromatography revealed expression of the protein in each of the cell lines (Figures 7-9). Sodium dodecyl sulfate polyacrylamide gel electrophoresis (SDS-PAGE) stained with Coomasie brilliant blue revealed high purity protein from each cell line, suggesting successful purification using Ni-affinity methods (Figure 10). In some

cases, Ni-affinity methods provided insufficient purity. In such cases, Ni-affinity chromatography was supplemented with anion exchange chromatography and size-exclusion chromatography in order to achieve the desire protein purity.

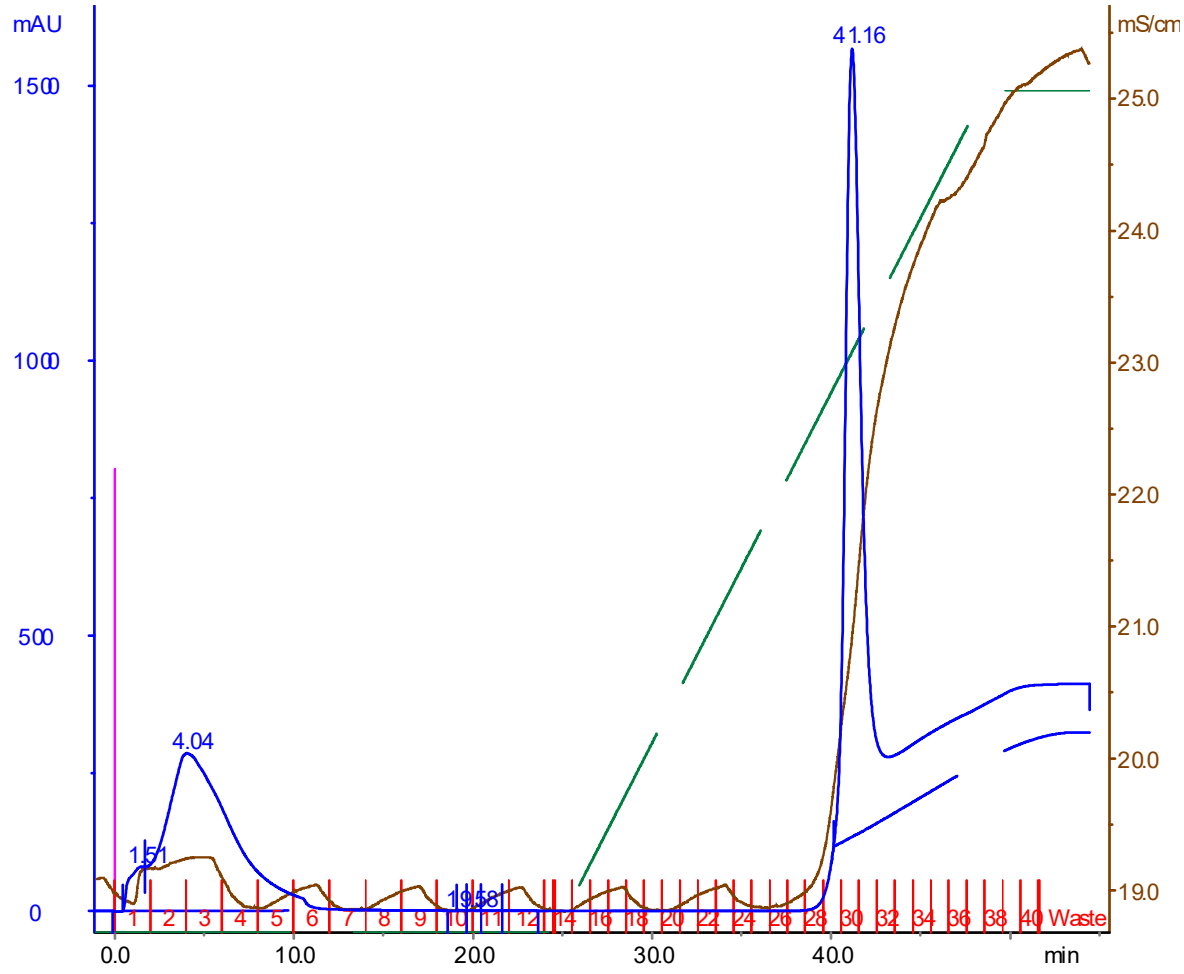

Figure 7: Purification chromatogram of TrxA-ApAFP752 expressed in the *E. coli* cell line Rosetta-gami™ 2(DE3). The various colored lines are representative of the following measurements: (Blue) absorption at 280 nm; (Green) percent concentration of elution buffer relative to the starting imidazole concentration; (Brown) solution/sample conductivity in units of mS cm^{-1}. The peak appearing at fraction 28 is consistent with the elution of TrxA-ApAFP752 fusion protein. Peaks prior to fraction 14 are consistent with non-6xHis proteins and heavily aggregated proteins.

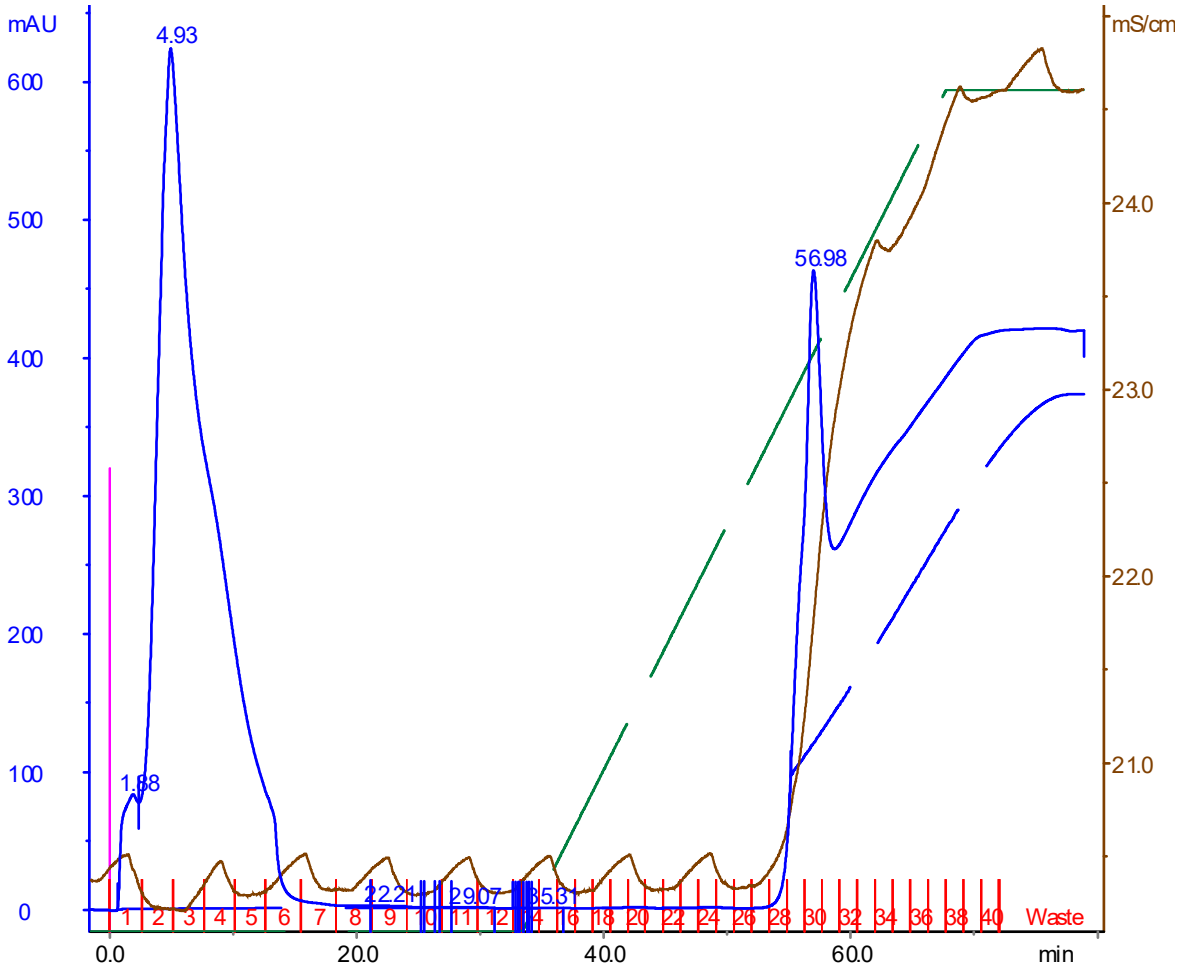

Figure 8: Purification chromatogram of TrxA-ApAFP752 expressed in the *E. coli* cell line Origami™ B(DE3). The various colored lines are representative of the following measurements: (Blue) absorption at 280 nm; (Green) percent concentration of elution buffer relative to the starting imidazole concentration; (Brown) solution/sample conductivity in units of mS cm^{-1}. The peak appearing at fraction 28 is consistent with the elution of TrxA-ApAFP752 fusion protein. Peaks prior to fraction 14 are consistent with non-6xHis proteins and heavily aggregated proteins.

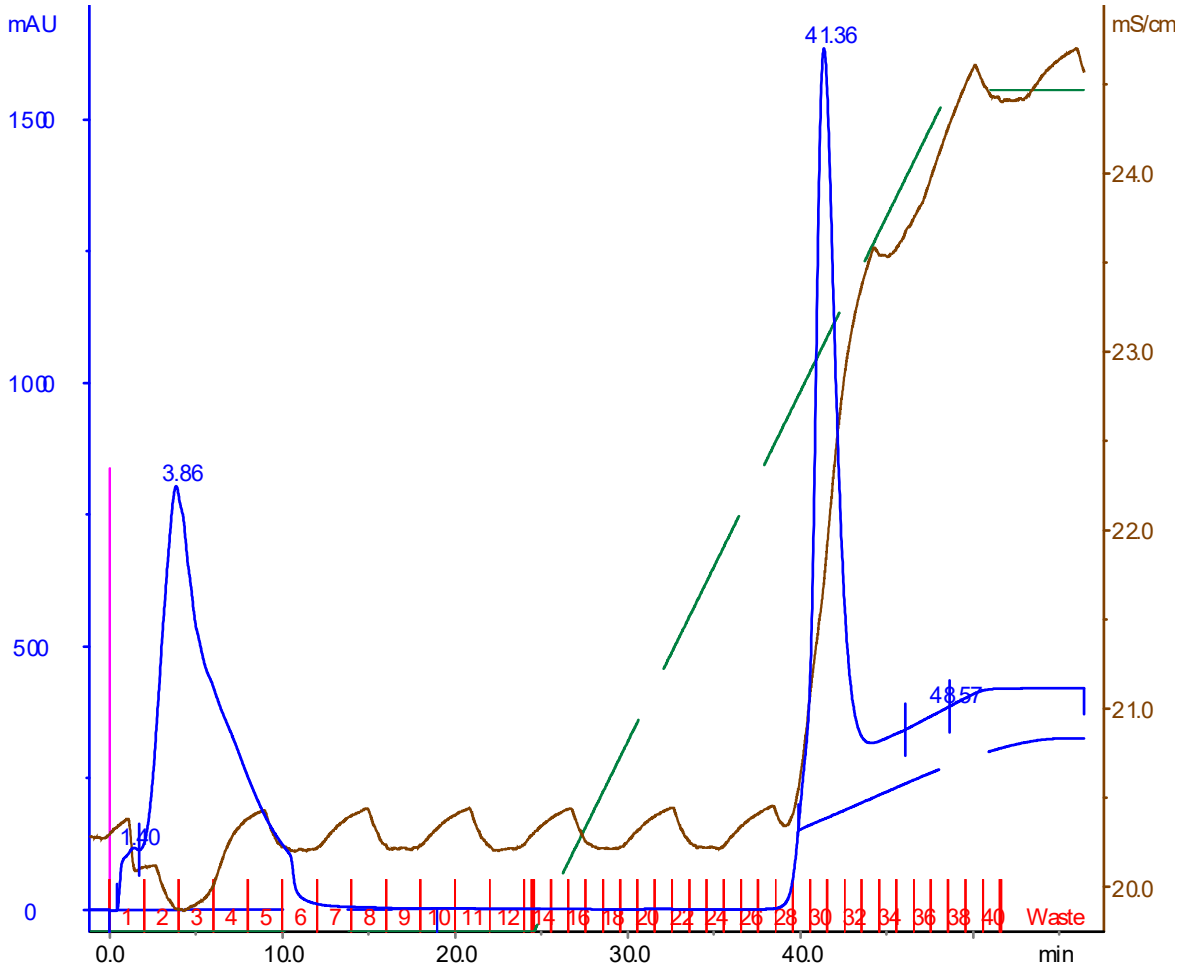

Figure 9: Purification chromatogram of TrxA-ApAFP752 expressed in the *E. coli* cell line BL21 (DE3) pLysS. The various colored lines are representative of the following measurements: (Blue) absorption at 280 nm; (Green) percent concentration of elution buffer relative to the starting imidazole concentration; (Brown) solution/sample conductivity in units of mS cm^{-1}. The peak appearing at fraction 28 is consistent with the elution of TrxA-ApAFP752 fusion protein. Peaks prior to fraction 14 are consistent with non-6xHis proteins and heavily aggregated proteins.

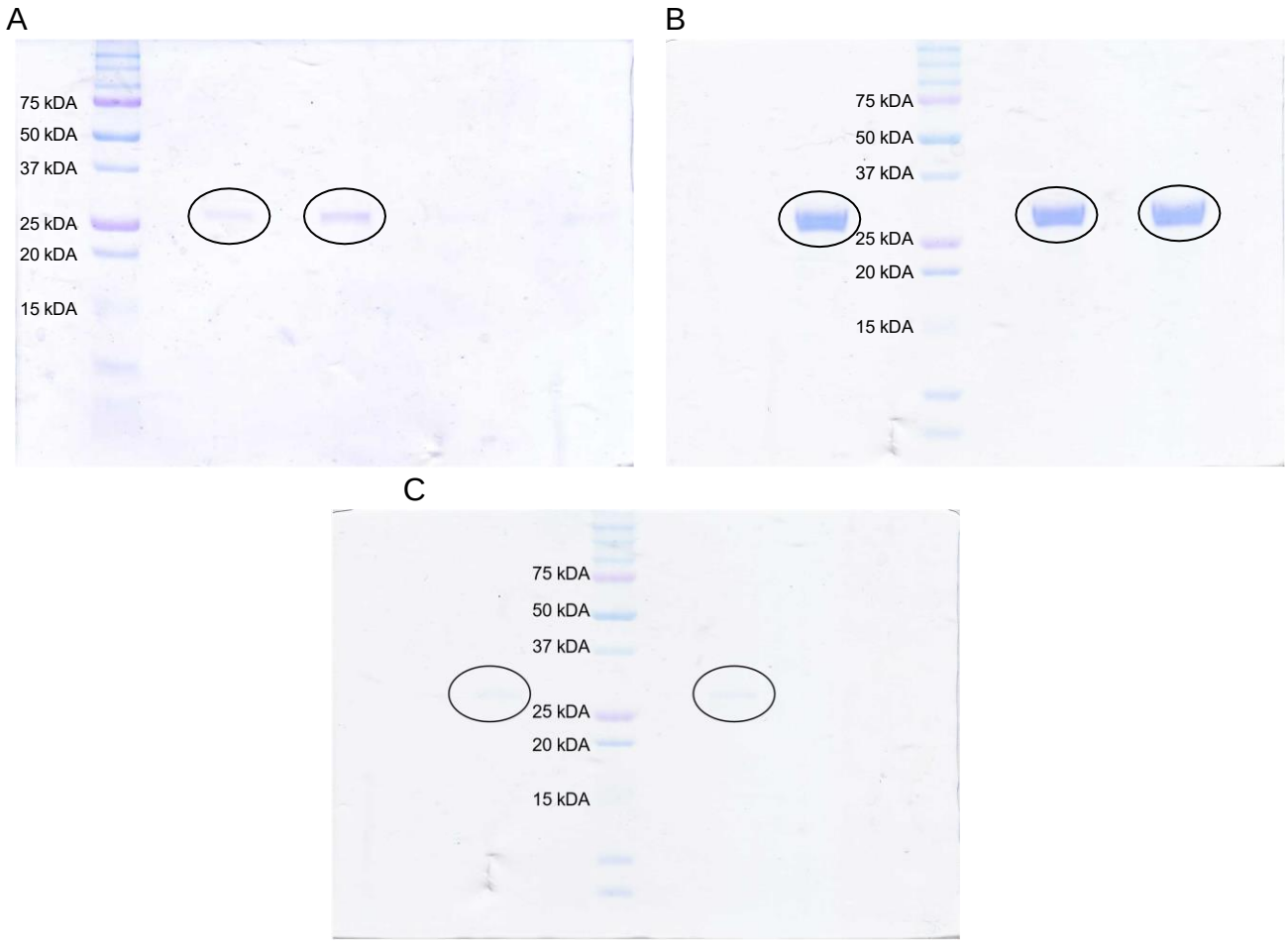

Figure 10: SDS-PAGE of 12% Tris-Tricine gels stained with Coomasie brilliant blue R-250. (A) TrxA-ApAFP752 from the *E. coli* cell line Rosetta Gami™ 2(DE3); (B) TrxA-ApAFP752 from the *E. coli* cell line BL21 (DE3) pLysS; (C) TrxA-ApAFP752 from the *E. coli* cell line Origami™ B(DE3). Protein bands appear in each expression slightly above 25-kDa. This is consistent with the 26.4-kDa molecular weight of TrxA-ApAFP752.

Each protein sample was then concentrated to a volume of 270 µL in preparation for NMR studies, as the 5 mm Shigemi® NMR tubes have an approximately 300 µL sample volume. The protein concentrations were calculated using UV-Visible spectroscopy at an absorbance of 280 nm[47]. The protein's molar absorptivity was calculated to be 19,575 M^{-1} cm^{-1} using the ExPASy ProtParam tool[48]. It was found that the concentrations of the fusion protein from Rosetta Gami™ 2(DE3), Origami™ B(DE3) and BL21 (DE3) pLysS

were 47 µM, 96 µM and 31 µM, respectively (Figure 11). From these concentrations the protein yield for each expression vector was determined to be 62 µg L^{-1}, 41 µg L^{-1} and 96 µg L^{-1}, respectively.

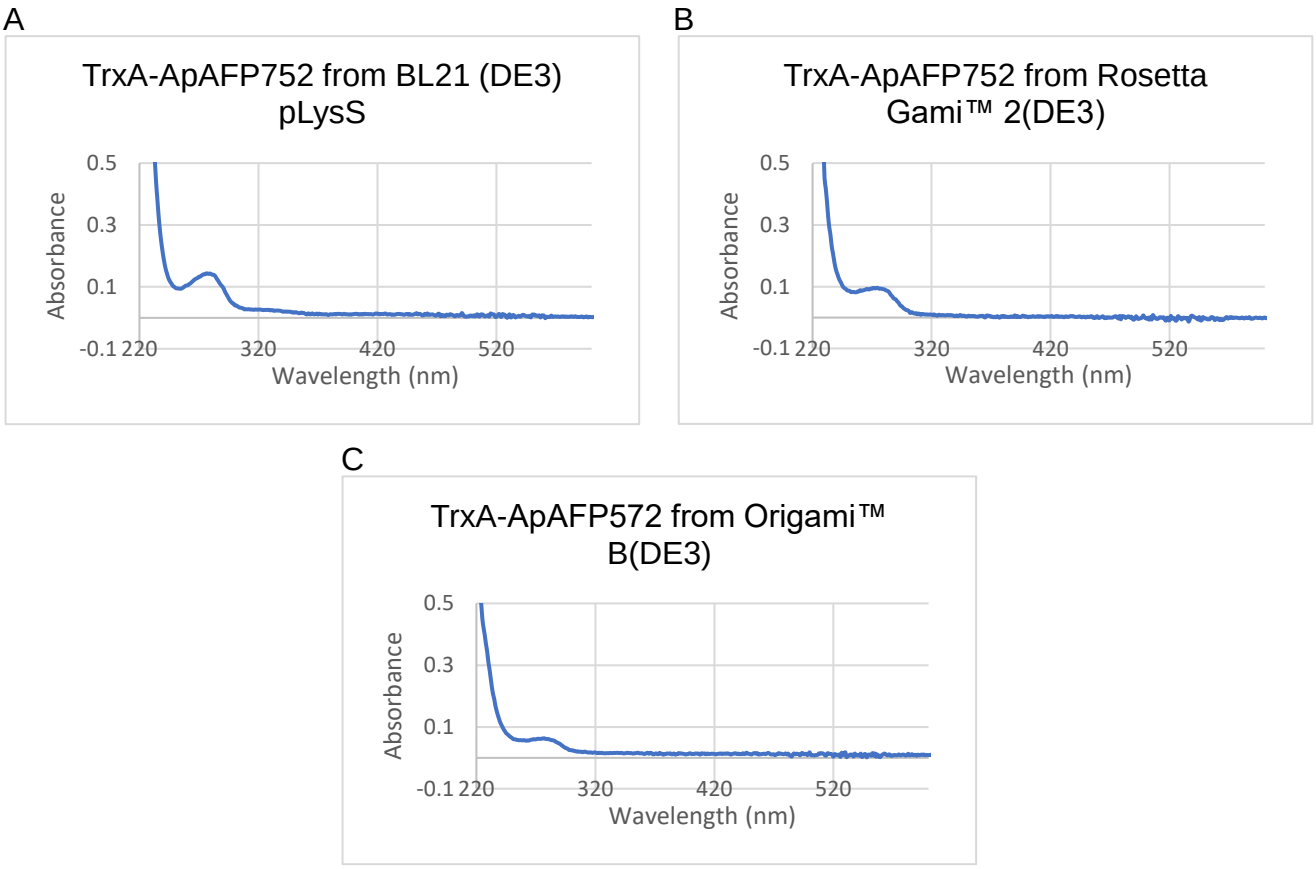

Figure 11: UV-Vis absorption spectra of TrxA-ApAFP752 from each expression vector. Spectra were collected at a 10-fold dilution of the protein. A_{280} was found to be (A) 0.142, (B) 0.0916 (C) 0.0611.

<u>NMR sample preparation</u>

Each sample was mixed with deuterium oxide (D_2O), 4,4-dimethyl-4-silapentane-1-sulfonic acid (DSS) and sodium azide (NaN_3) to a final concentration of 10% v/v D_2O, 200 µM DSS and 1 mM NaN_3 in preparation for NMR studies. D_2O is used for sample locking in the NMR spectrometer. DSS is commonly used as an internal reference in aqueous

solution NMR experiments. NaN_3 is a known biocide and is used in protein NMR samples as a method of inhibiting bacterial growth in the sample during experiments. 1-dimensional (1D) ^{1}H and 2-dimensional (2D) ^{1}H-^{15}N heteronuclear single quantum coherence (HSQC) NMR experiments were acquired for each sample to evaluate the protein fold. Spectra were acquired on a Bruker Avance III 600 MHz NMR spectrometer equipped with a BBO probe at 25 °C and referenced to DSS (internal reference)[49]. ^{1}H-^{15}N HSQC spectra for the fusion protein expressed in *E. coli* cell lines Rosetta gami™ 2(DE3) and BL21 (DE3) pLysS exhibited well-defined peaks with even dispersion and signal intensities (Figures 12). The ^{1}H-^{15}N HSQC spectrum for the sample expressed in *E. coli* cell line Origami™ B(DE3) exhibited poor signal intensity with poorly defined peaks and a lack of peak dispersion (Figure 13A). Further evaluation of the ^{1}H spectrum showed only 3 distinct peaks at 8.44 ppm, 7.90 ppm and 7.18 ppm indicating improper folding or aggregation of the protein (Figure 13B). Because of these results, no further expression or experimentation was performed using Origami™ B(DE3) cells.

A

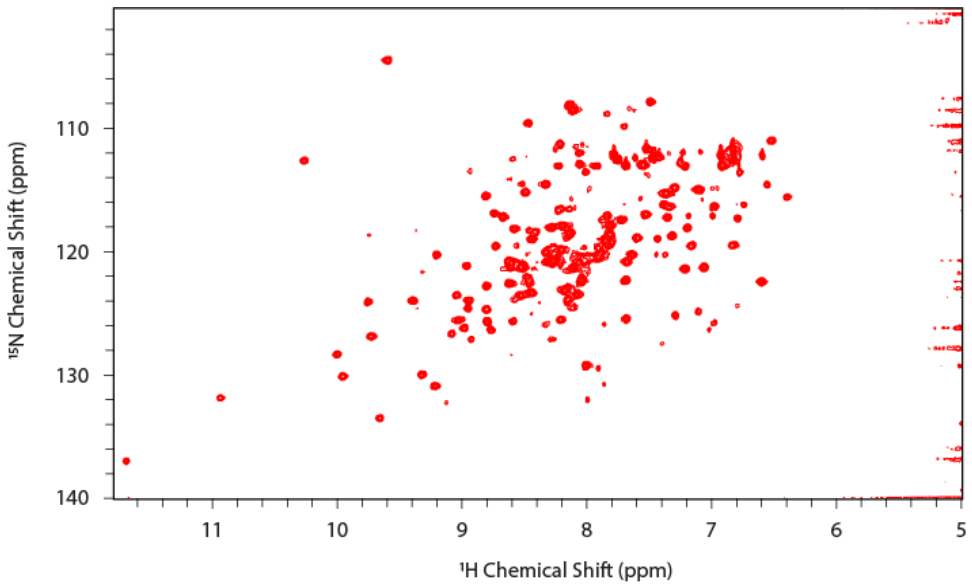

B

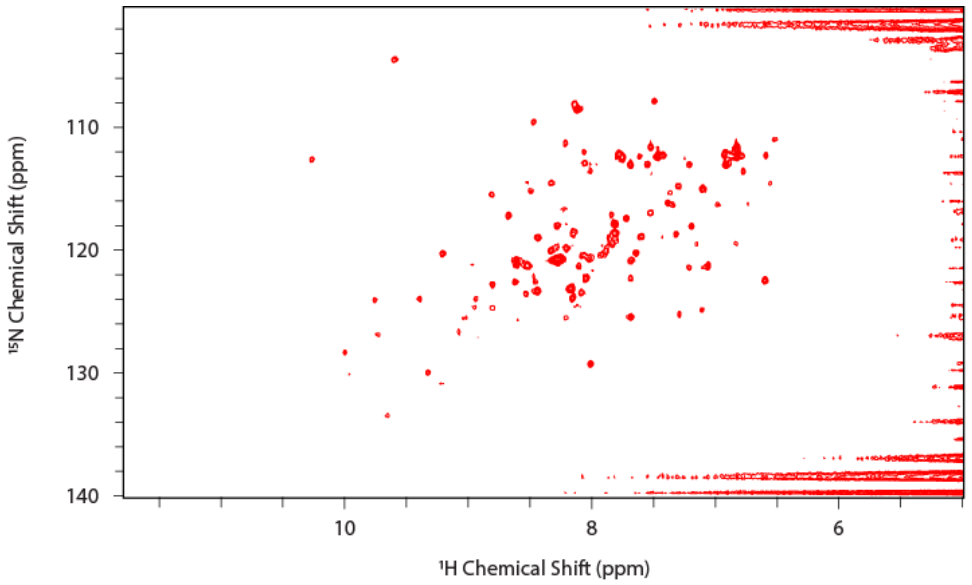

Figure 12: ^{1}H-^{15}N HSQC NMR spectra of TrxA-ApAFP752 from *E. coli* cell lines (A) BL21 (DE3) pLysS and (B) Rosetta gami™ 2(DE3). Both spectra exhibit a well folded protein. *Note:* the concentration of TrxA-ApAFP752 in spectrum A is more than double of spectrum B, resulting in a much stronger signal.

A

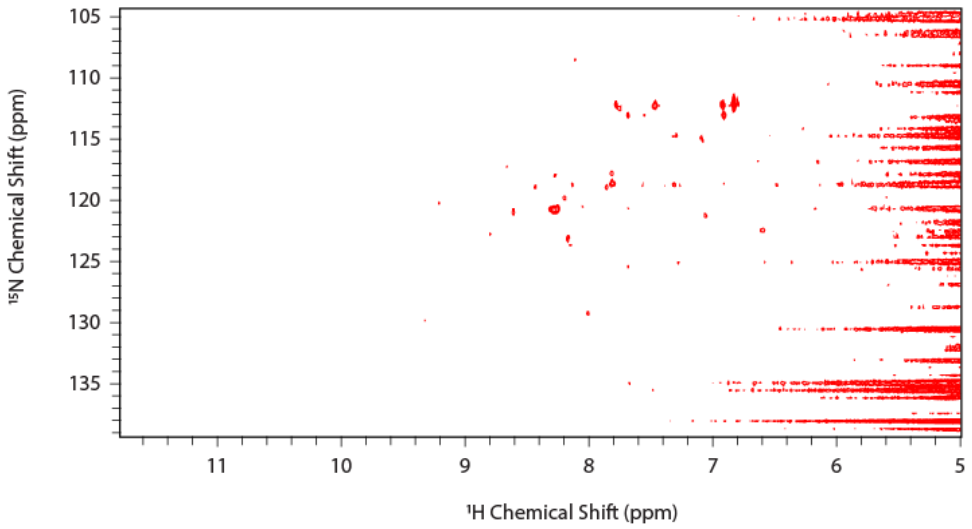

B

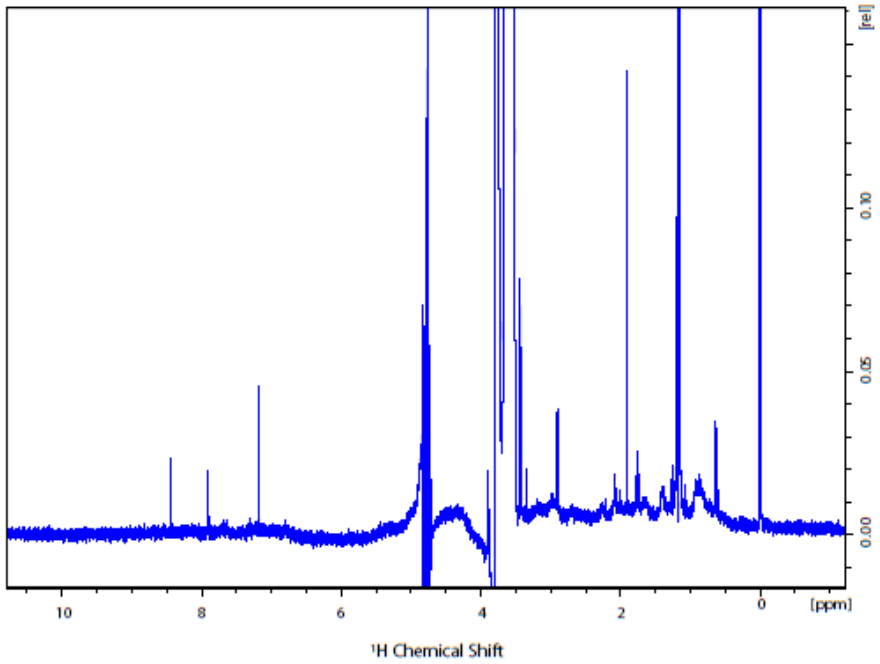

Figure 13: NMR spectra of TrxA-ApAFP752 from *E. coli* cell line Origami™ B(DE3). (A) ^{1}H-^{15}N HSQC spectrum illustrates a lack of proper fold. (B) ^{1}H-1D containing 3 distinct peaks at 8.44 ppm, 7.90 ppm and 7.18 ppm indicative improper folding or aggregation of the protein.

Optimization of expression of isotopically enriched TrxA-ApAFP752 protein in *E. coli* cell line BL21 (DE3) pLysS

The expression of the TrxA-ApAFP752 was further optimized using *E. coli* BL21 (DE3) pLysS, as this expression vector resulted in the highest protein yield. Due to the poor yield of the protein in the labeled minimal growth medium, the ratio of resuspension of the cells from LB broth to labeled minimal growth medium was changed from 1:1 to 4:1, effectively increasing the cell density during the overexpression stage by a factor of four[50]. Additionally, the temperature of the overexpression phase was lowered from 25 °C to 15 °C to facilitate folding of the protein. Optimization of the fusion protein expression was performed by sampling the minimal growth medium, post induction, at hours 6 through 22 at 2-hour increments. Samples were centrifuged at 4,500 x *g* for 20 minutes and the resultant cell pellets were stored at -80 °C until utilized.

The frozen cell pellets were thawed in the previously described lysis buffer containing 1 mM ethylenediaminetetraacetic acid (EDTA) and 10 mg mL^{-1} lysozyme (Sigma Aldrich) at 37 °C. Freeze-thaw cycles were implemented in triplicate to ensure complete lysis of the cells. The fusion protein was isolated from the cells via centrifugation, with the supernatant being collected. Samples were run through SDS-PAGE and analyzed via western blotting. Evaluation of the western blots showed a 12-hour induction time resulted in the strongest band intensity, indicating the highest protein concentration and protein yield (Figure 14).

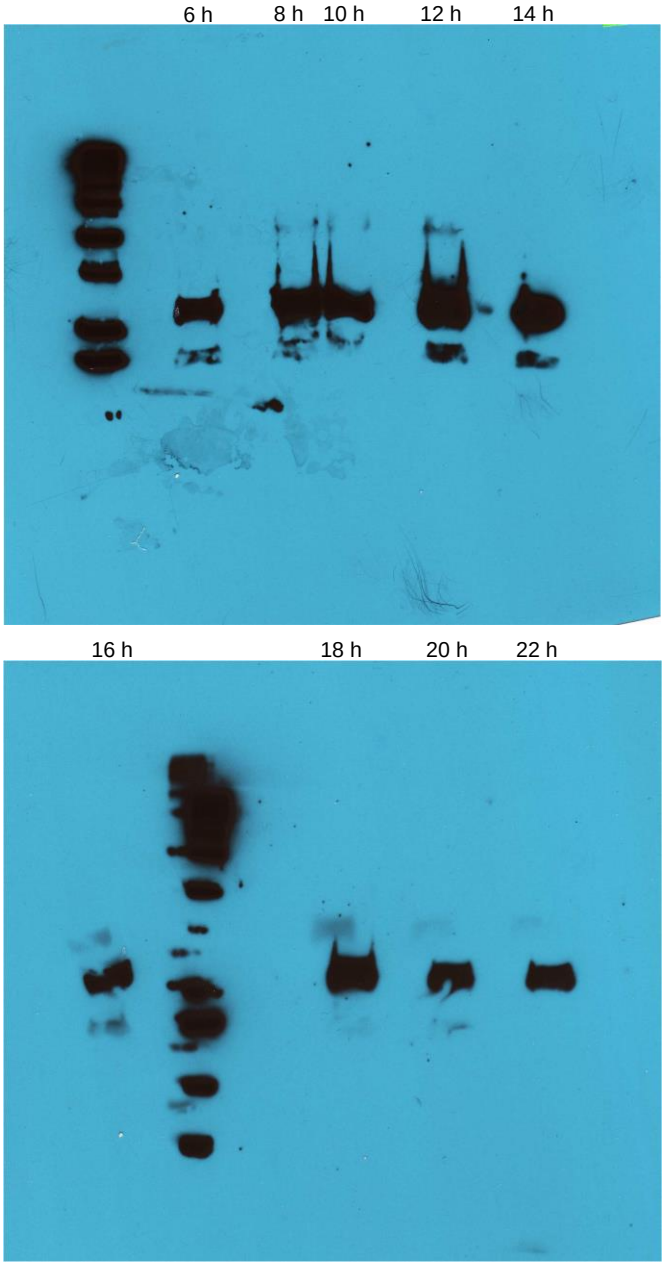

Figure 14: Western blots TrxA-ApAFP752 expressed in BL21 (DE3) pLysS sampled during the overexpression stage from hours 6 to 22 at 15 °C temperature and 225 rpm shaking. The strongest protein band was exhibited at the 12-hour expression time, which was determined to be optimal time under these experimental conditions and was used in further experiments.

II. Isolation of ApAFP752 from TrxA-ApAFP752

In order to study the antifreeze protein in its naturally occurring form, ApAFP752 was removed from the fusion protein via proteolytic cleavage using bovine His-enterokinase (Prospec-Tany). TrxA-ApAFP752 cleavage was performed in 50 mM potassium phosphate, 20 mM NaCl, pH 8.0. A small-scale cleavage test was performed with an enzyme to protein mixture ratio of 1 IU bovine His-enterokinase to 400 ug TrxA-ApAFP752 for six hours at 25 °C. Samples were taken every two hours. SDS-PAGE was performed and stained with Coomasie brilliant blue (Figure 15).

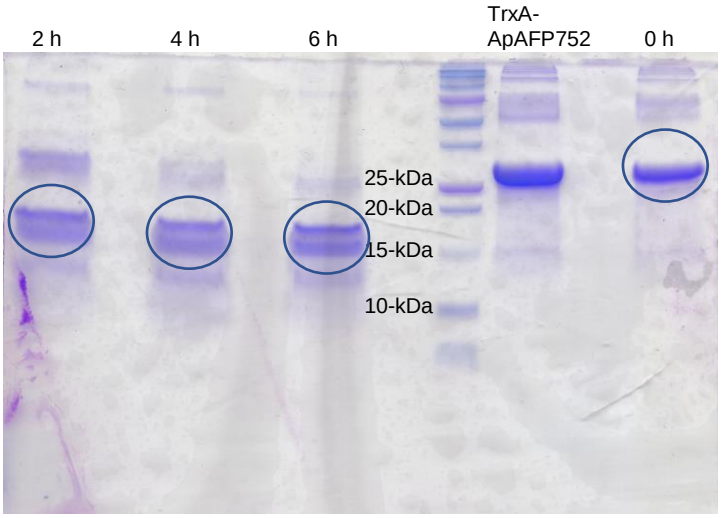

Figure 15: Cleavage of TrxA-ApAFP752 with bovine His-enterokinase. Degradation of the fusion protein becomes noticeable at 2 hours. TrxA appears at approximately 17-kDa. At 6 hours the cleavage appears to be complete.

A band for ApAFP752 was not found in the gel, however, the optimal cleavage time was determined by the degradation of the TrxA-ApAFP72 band and the appearance of the TrxA band at approximately 17-kDa. Six hours was found to be an optimal cleavage time at this protein-enzyme ratio and a full scale was performed using these conditions. The

post-cleavage samples were purified using FPLC Ni-affinity. Due to the 6xHis-tag being positioned on the TrxA side of the cleavage site, the FPLC flow-through contained the ApAFP752, while the Ni-affinity elution contained the TrxA and the bovine His-enterokinase (Figure 16). SDS-PAGE was performed on the isolated ApAFP752 sample and silver staining was used to identify the protein (Figure 17). The molar absorptivity of ApAFP752 was calculated to be 5,400 M^{-1} cm^{-1} using the ExPASy ProtParam tool[48]. Due to the lack of tryptophan, the absorbance of tyrosine at 275 nm was used to calculate the concentration of ApAFP752 protein samples.

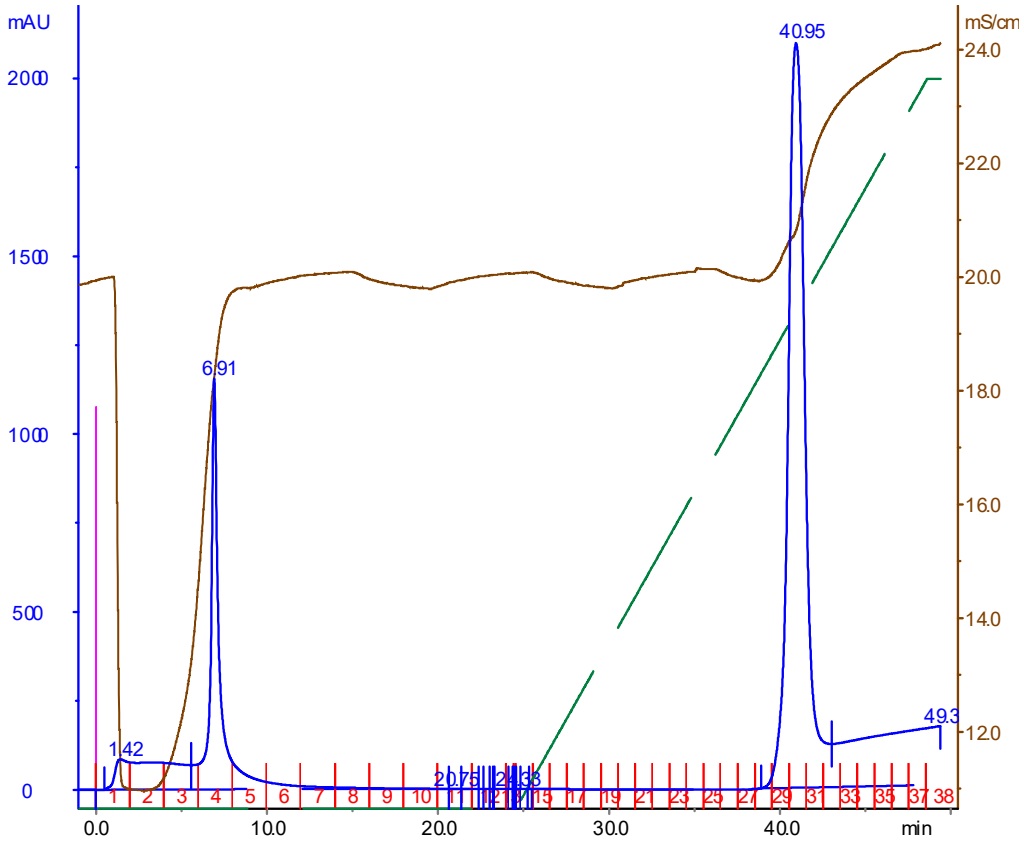

Figure 16: Ni-affinity chromatography of post-cleavage TrxA-ApAFP752 fusion protein. The peak appearing at fraction 4 is the elution of ApAFP752 protein in the flow-through. The peak at fraction 29 is consistent with the elution of TrxA and bovine His-enterokinase.

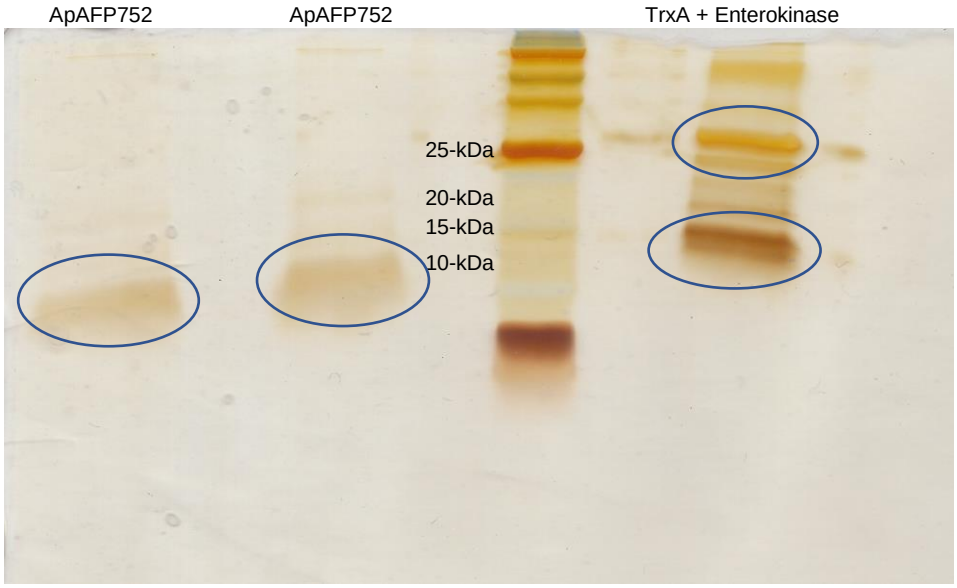

Figure 17: Silver stain of 16.5% tris-tricine SDS-PAGE of TrxA-ApAFP752 fusion protein biproducts. Left two lanes show a band just below 10-kDa which is consistent with 9.4-kDa molecular weight of ApAFP752. Right lane contains a strong band just above 15-kDa (TrxA) and just 25-kDa (enterokinase).

To simplify the complex processes in expressing, cleaving and isolating ApAFP752 from the fusion protein, the sequence for ApAFP752 was cloned into the pET23a plasmid construct. The plasmid was transformed into *E. coli* BL21 (DE3) pLysS cells, and the protein was expressed under the conditions listed above. The protein was harvested using French press and centrifugation in the same manner used for TrxA-ApAFP752. The sample was purified with Ni-affinity chromatography by FPLC and the concentration of the purified protein was analyzed by UV-Vis spectrophotometry (Figure 18A). The sample was prepared for NMR spectroscopy experiments as listed above. NMR data was acquired on a Bruker Avance III 600 MHz spectrometer. The NMR data showed a very weak protein signal with few discernable peaks (Figure 18B). This information, coupled

with the strong signal intensity seen in the UV-Vis spectrum for the same sample, indicates that the sample was either heavily aggregated or improperly folded.

A

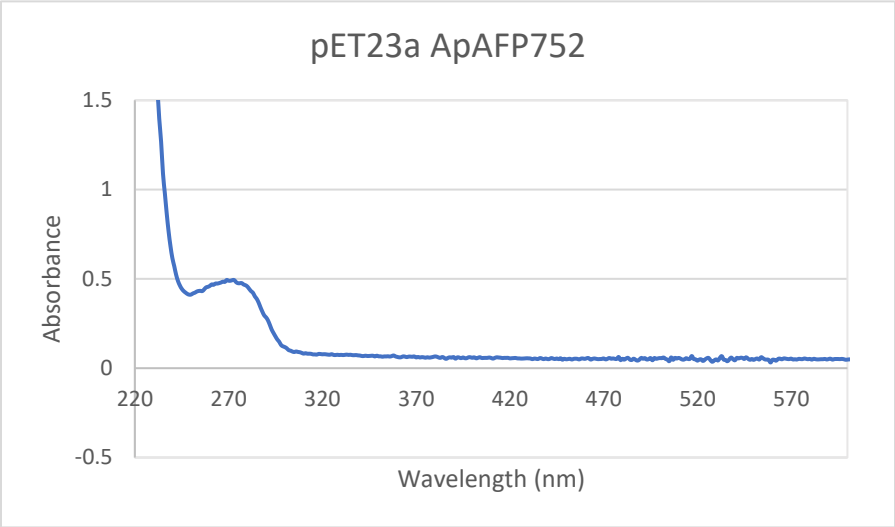

B

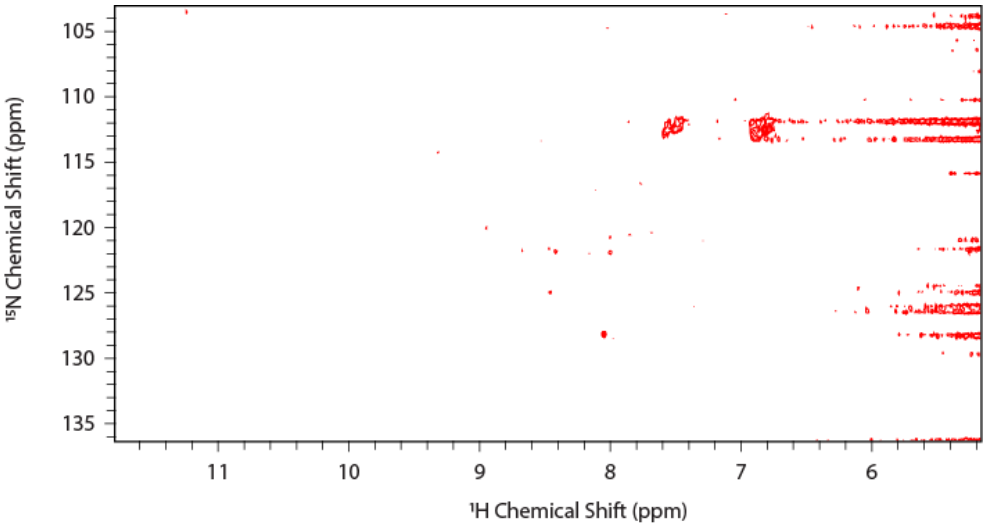

Figure 18: ApAFP752 from the pET23a plasmid expressed in *E. Coli* BL21 (DE3) pLysS cells. A) UV-Vis spectrum showing absorbance signal at 275 nm. B) ^{1}H-^{15}N HSQC NMR spectrum of the same protein sample as in Figure A. A conglomeration of peaks associated with Gln and Asn side-chain N-H correlations are observable along with a few other peaks. The NMR spectrum indicates the sample is not a well-folded protein.

Additional steps were taken in attempt to denature then refold the protein into its native structure. ApAFP752 was first denatured and the disulfide bonds were reduced in a solution of 8 M guanidine-HCl, 100 mM Tris-HCl (pH 8.5), 1mM ethylenediaminetetraacetic acid (EDTA) and 12 mM 2-mercaptoethanol, and the solution was slowly mixed at 22 °C for 1 hour[25]. The protein sample was then added to a cold solution of 50 mM K_2HPO_4, 1 mM EDTA, 2 mM 2-mercaptoethanol and 100 mM NaCl at pH 10.7. The solution was mixed for 16 hours at 15 °C, after which the sample was dialyzed in 10 mM Tris-HCl, 1 mM EDTA and 100 mM NaCl at pH 8.0 for 48 hours. The sample was then left to oxidize and refold via slow agitation for 6 weeks. The resulting sample was then concentrated to 270 μL, and the concentration was checked using UV-Vis spectrophotometry. The UV-Vis spectrum for the re-oxidized sample showed no discernable protein signal, indicating that the refolding was unsuccessful and may have resulted in degradation of the protein (Figure 19).

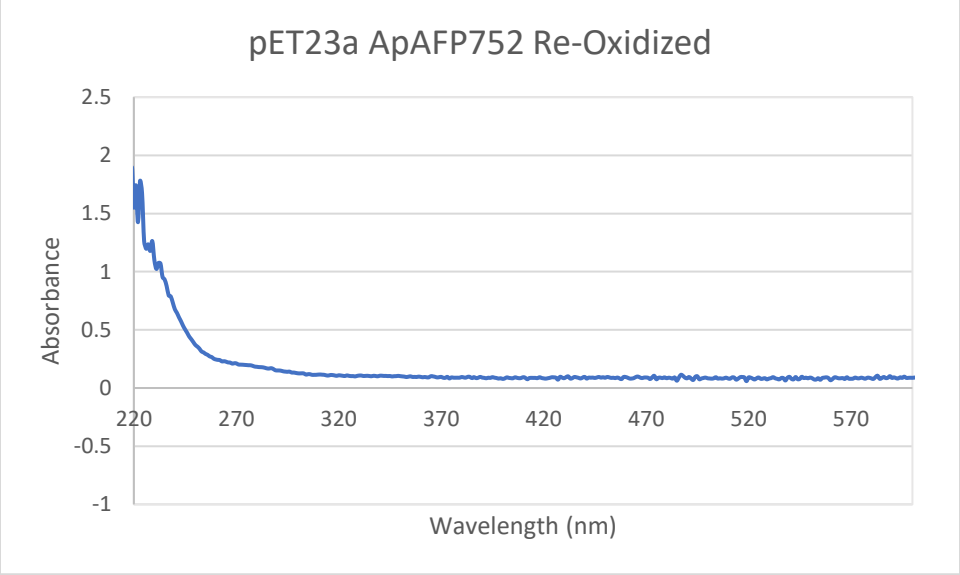

Figure 19: UV-Vis spectrum of ApAFP752 from the pET23a plasmid expressed in *E. coli* BL21 (DE3) pLysS cells. No discernable protein signal is observed at 275 nm.

III. Confirmation of ApAFP752 by Mass Spectrometry

Mass spectrometry was performed on a lyophilized ^{15}N-labeled ApAFP752 sample by Dr. Feixia Chu at the University of New Hampshire in order to confirm the sequence of the protein post-cleavage. The lyophilized protein was resuspended in 6M guanidine hydrochloride to a final concentration of 5-10 μM. The protein was reduced by DTT (10 mM final concentration) at 56 °C for 45 minutes, then alkylated by iodoacetamide (25 mM final concentration) in darkness at room temperature for 1 hour. The protein solution was diluted with 25 mM ammonium carbonate to 0.5-1 μM, immediately followed by the addition of trypsin (2% protein weight). In-solution digestion was carried out at 37 °C for 2 hours, before LC-MS/MSMS analysis[51]. Briefly, 1 μl aliquot of the digestion mixture was injected into a Dionex Ultimate 3000 RSLCnano UHPLC system with an autosampler (Dionex Corporation, Sunnyvale, CA, USA), and the eluant was connected directly to a nanoelectrospray ionization source of an LTQ Orbitrap XL mass spectrometer (Thermo Fisher). LC-MS data were acquired in an information-dependent acquisition mode, cycling between a MS scan (m/z 310-2000) acquired in the Orbitrap, followed by low-energy CID analysis in the linear ion trap.

Though the incorporation of ^{15}N is higher than 90%, the presence of ^{14}N makes it difficult to determine the monoisotopic masses for effective database search. Therefore, we inspected the MSMS spectra of five high abundance peptides acquired in the LC-MS/MSMS run, with m/z values at 663.27^{2+}, 846.97^{5+}, 1004.34^{2+}, 1097.41^{2+} and 1167.45^{3+} (Figure 20). Except for peptide 846.97^{5+}, high quality MSMS spectra were acquired for all peptides for the conclusive identification of the antifreeze protein.

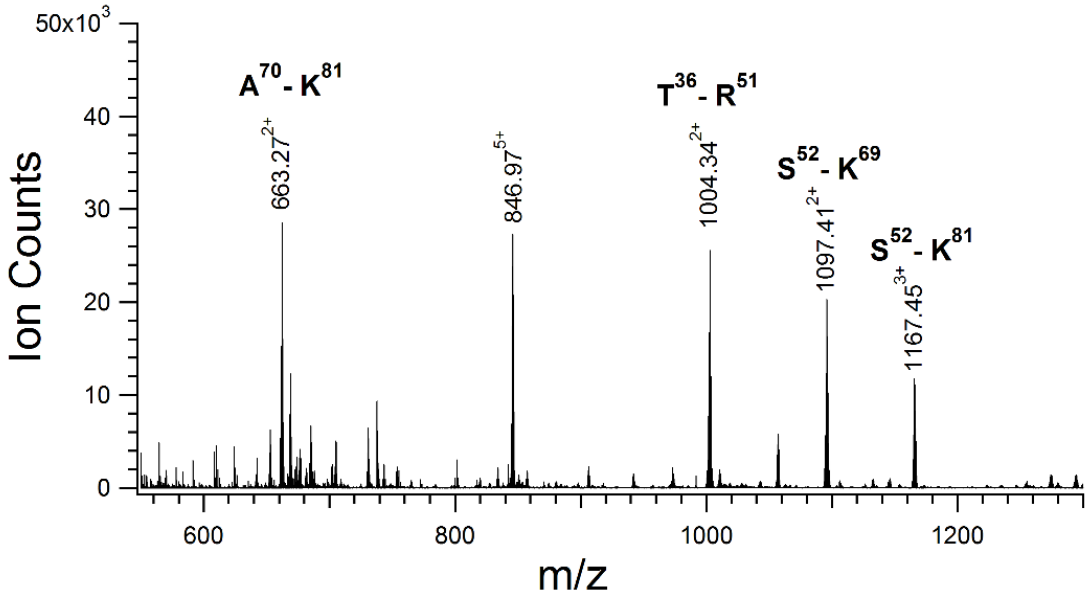

Figure 20: Spectrum of anti-freeze protein ApAFP752, averaged through the peptide elution window from the LC-MS/MSMS analysis.

Figure 21 shows a representative MSMS spectrum for peptide Ala^{70}-Lys^{81}. The nearly complete C-terminal containing fragment series (y ions) provides sufficient information on this peptide sequence. As expected, the mass of a y ion matches to the mass of unlabeled counterpart and the number of nitrogen atoms in the fragment. Based on the identification of four high abundance peptides, we can conclude that anti-freeze protein ApAFP752 is the dominant protein component in the sample.

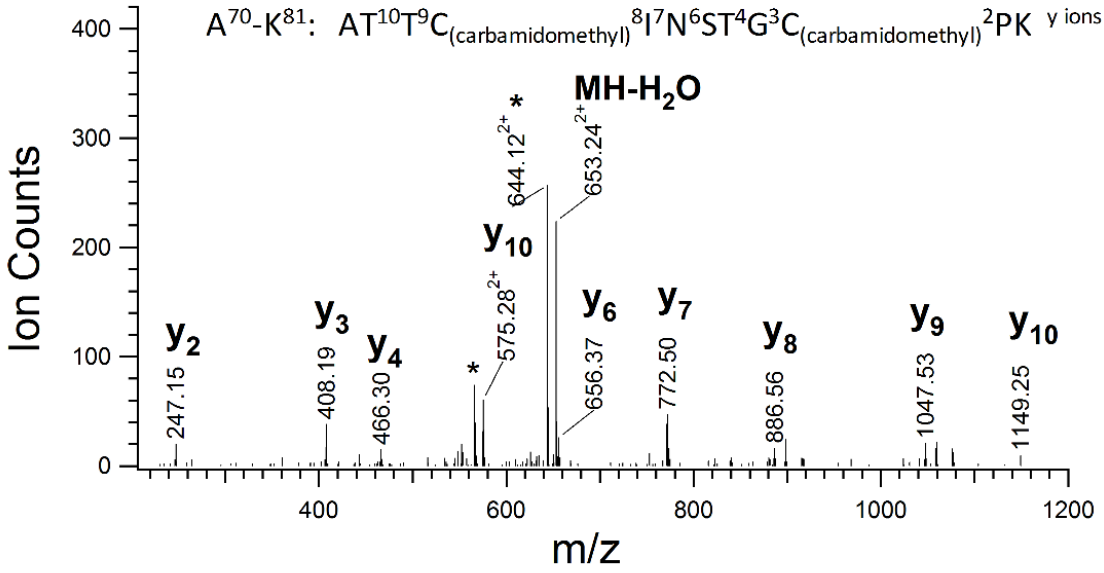

Figure 21: Representative MSMS Spectrum of the anti-freeze protein, ApAFP752, peptide, Ala70-Lys81. The almost complete C-terminal containing y ions series provides conclusive identification of the peptide. Cysteine residues were carbamidomethyl modified through reduction and alkylation.

IV. Conclusion

TrxA-ApAFP752 has been successfully expressed and purified. BL21 (DE3) pLysS was the most proficient bacterial vector for expressing a well folded fusion protein, which was confirmed and NMR spectroscopy. Ni-affinity chromatography by FPLC was found to be sufficient for the purification of the fusion protein in most cases. In situations where Ni-affinity was insufficient, supplemental purifications were performed using anion exchange chromatography and size-exclusion chromatography. Stable isotope labeling for NMR spectroscopy was optimized and confirmed with western blots, SDS-PAGE and NMR spectroscopy. Lysis of purified TrxA-ApAFP752 with recombinant bovine enterokinase-His resulted in a well folded, non-fusion form of the antifreeze protein. Isolation of the protein, ApAFP752, was achieved with Ni-affinity chromatography via

FPLC by collecting the flow through. Protein stability was confirmed by NMR spectroscopy and the protein sequence was confirmed by mass spectrometry.

CHAPTER 3

CHARACTERIZATION OF ANTIFREEZE PROTEIN PROPERTIES

As discussed in Chapter 1 (in section "V: Antifreeze Protein Properties"), antifreeze proteins can be characterized by their thermal hysteresis, ice recrystallization, and ice crystal shaping activity. Thermal hysteresis studies of the fusion protein, TrxA-ApAFP752, were first reported by Ji Ma and coworkers in 2010 and 2011[35,43]. Data collected using differential scanning calorimetry (DSC) and osmometry provided the first insight into the thermal hysteresis activity (THA) of this protein. Using osmometry, they reported ice crystals in the shape of hexagonal disks consistent with ice crystal shaping properties associated with the AFP binding both the prism and basal planes of ice. This study indicates that TrxA-ApAFP752 is a hyperactive antifreeze protein. In order to achieve **Project 1, Aim 2: Investigate the cryoprotective mechanism ApAFP752 in live cells**, we further investigated the antifreeze properties of the fusion protein, TrxA-ApAFP752, and the isolated antifreeze protein, ApAFP752, and their potential as cryoprotectants.

I. Thermal Hysteresis Activity of TrxA-ApAFP752 and ApAFP752

The thermal hysteresis activity of both the fusion protein, TrxA-ApAFP752, and ApAFP752 where studied using differential scanning calorimetry (DSC). Samples of TrxA-ApAFP752 were evaluated at concentrations of 1 mg mL^{-1}, 3 mg mL^{-1} and 5 mg mL^{-1}. Samples were tested in a buffer consisting of 50 mM potassium phosphate, 20 mM NaCl. An aliquot of 10 μL of each sample was loaded into Tzero® aluminum hermetic pans (TA

Instruments) cooled to -30.0 °C at a rate of 1 °C min^{-1} and held at this temperature for 10 minutes. Samples were then heated at 1 °C min^{-1} up to -1.0 °C, held at this temperature for 5 minutes and cooled to -30.0 °C at 1 °C min^{-1}. This freeze-thaw cycle was repeated from -1.0 °C to +0.5 °C in increments of 0.1 °C in order to vary the percentage of ice present in the sample[43,52] (See Appendix: Materials and Methods – Differential Scanning Calorimetry). The percentage of ice was estimated to be $\left|[1-\left(-{}^{\Delta H_r}/_{\Delta H_m}\right)]\right| \times 100\%$, where ΔH_m is the enthalpy of melting and ΔH_r is the enthalpy of refreezing. Thermal hysteresis activity data was collected on a TA Instruments Q2000 Differential Scanning Calorimeter.

Each sample showed some amount of thermal hysteresis activity. The greatest activity was seen in the 5 mg mL^{-1} TrxA-ApAFP752 sample with a hysteresis of -0.39 °C (Figure 22). Both the 1 mg mL^{-1} and the 3 mg mL^{-1} samples exhibited lower activity at -0.30 °C (Figure 23) and -0.36 °C (Figure 24) respectively. The ice fractions for each sample were calculated to be 10.8 % at 1 mg mL^{-1}, 10.5 % at 3 mg mL^{-1} and 14.0 % at 5 mg mL^{-1} (Table 1). While the 1 mg mL^{-1} and 3 mg mL^{-1} samples shared similar ice fractions there was still a noticeable increase in the thermal hysteresis activity as the concentration increased. This overall trend of increase in activity with respect to increase in concentration is to be expected.

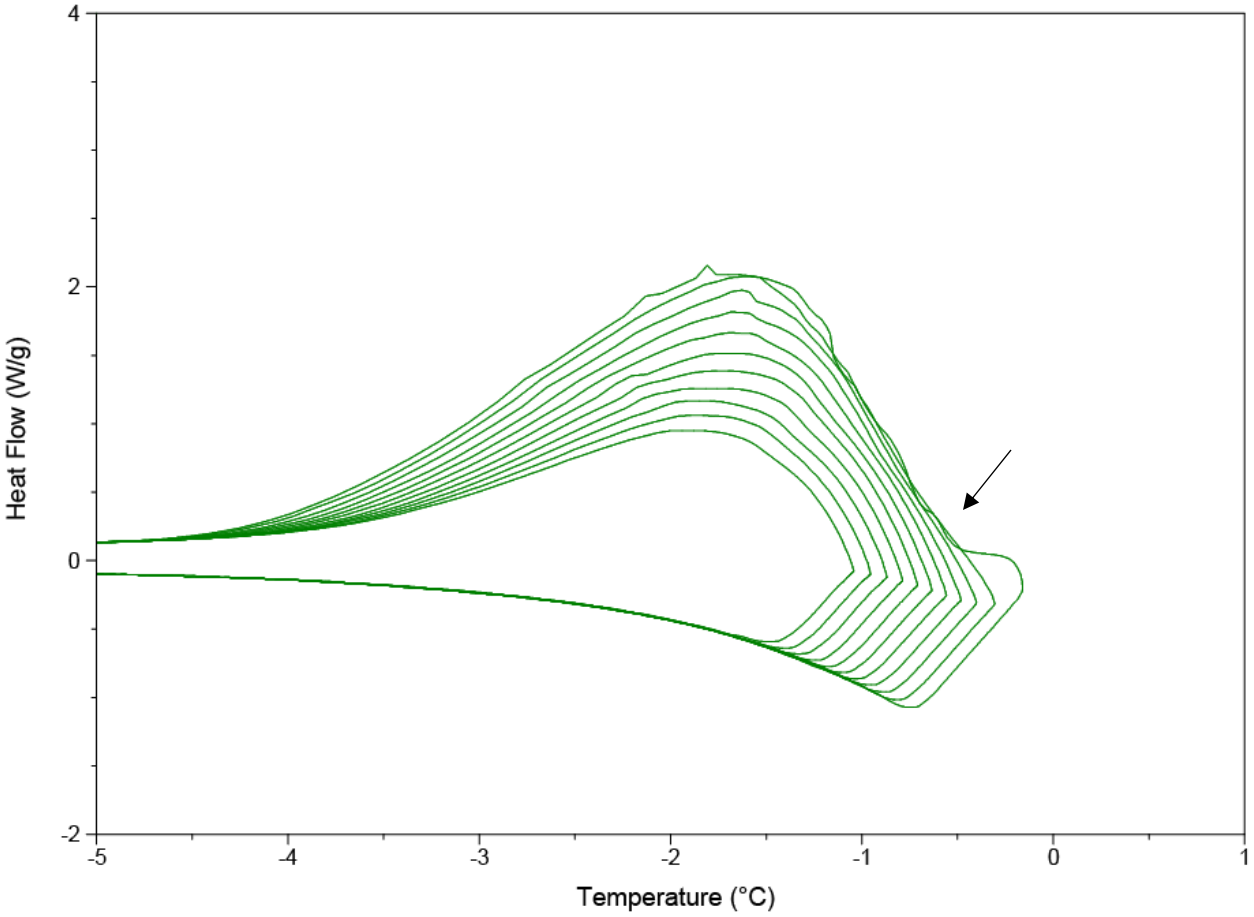

Figure 22: DSC curves of the fusion protein, TrxA-ApAFP752, at 5 mg mL^{-1} concentration. The black arrow indicates the onset of freezing in the sample. The thermal hysteresis activity was found to be -0.39 °C at an ice fraction of 13.8%.

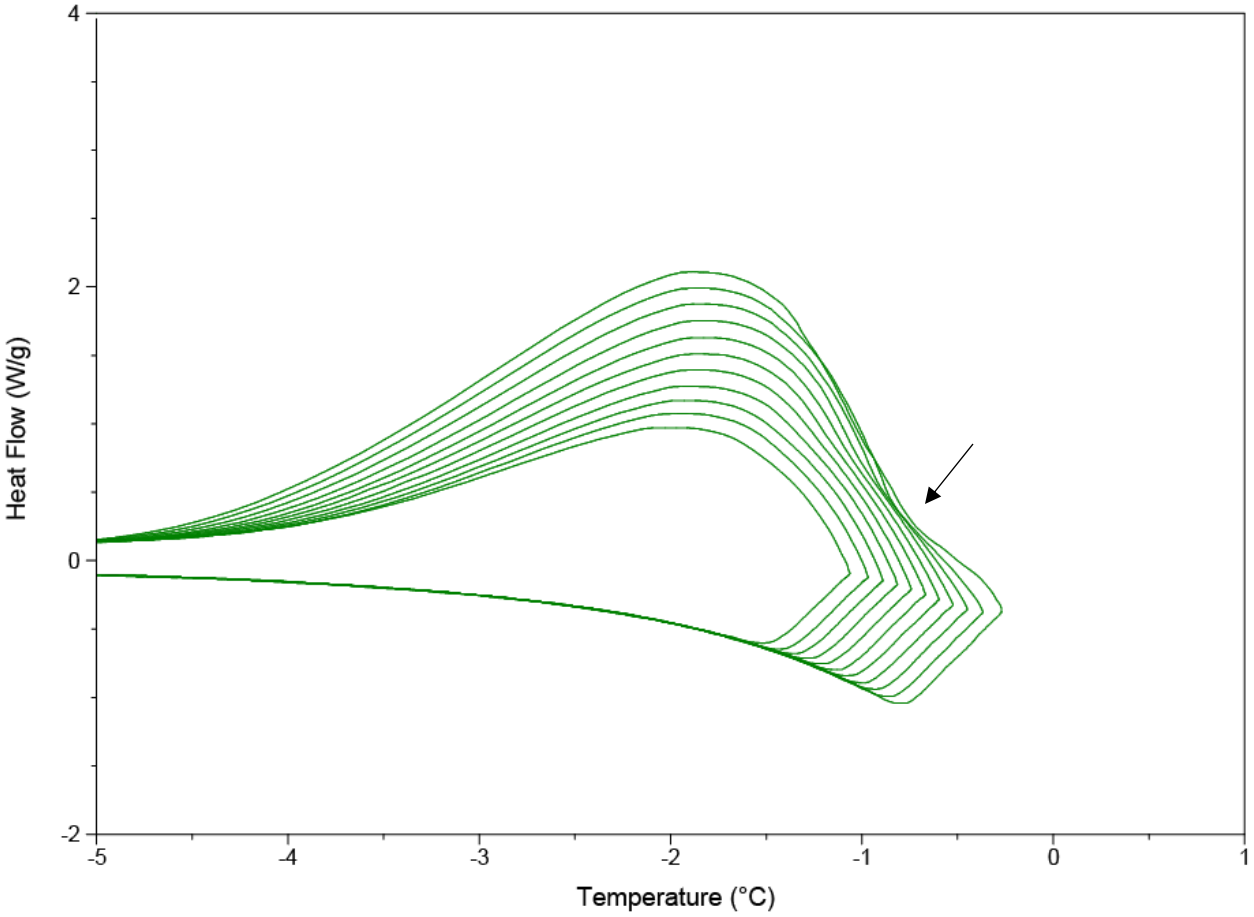

Figure 23: DSC curves of the fusion protein, TrxA-ApAFP752, at 1 mg mL^{-1} concentration. The black arrow indicates the onset of freezing in the sample. The thermal hysteresis activity was found to be -0.30 °C at an ice fraction of 10.8%.

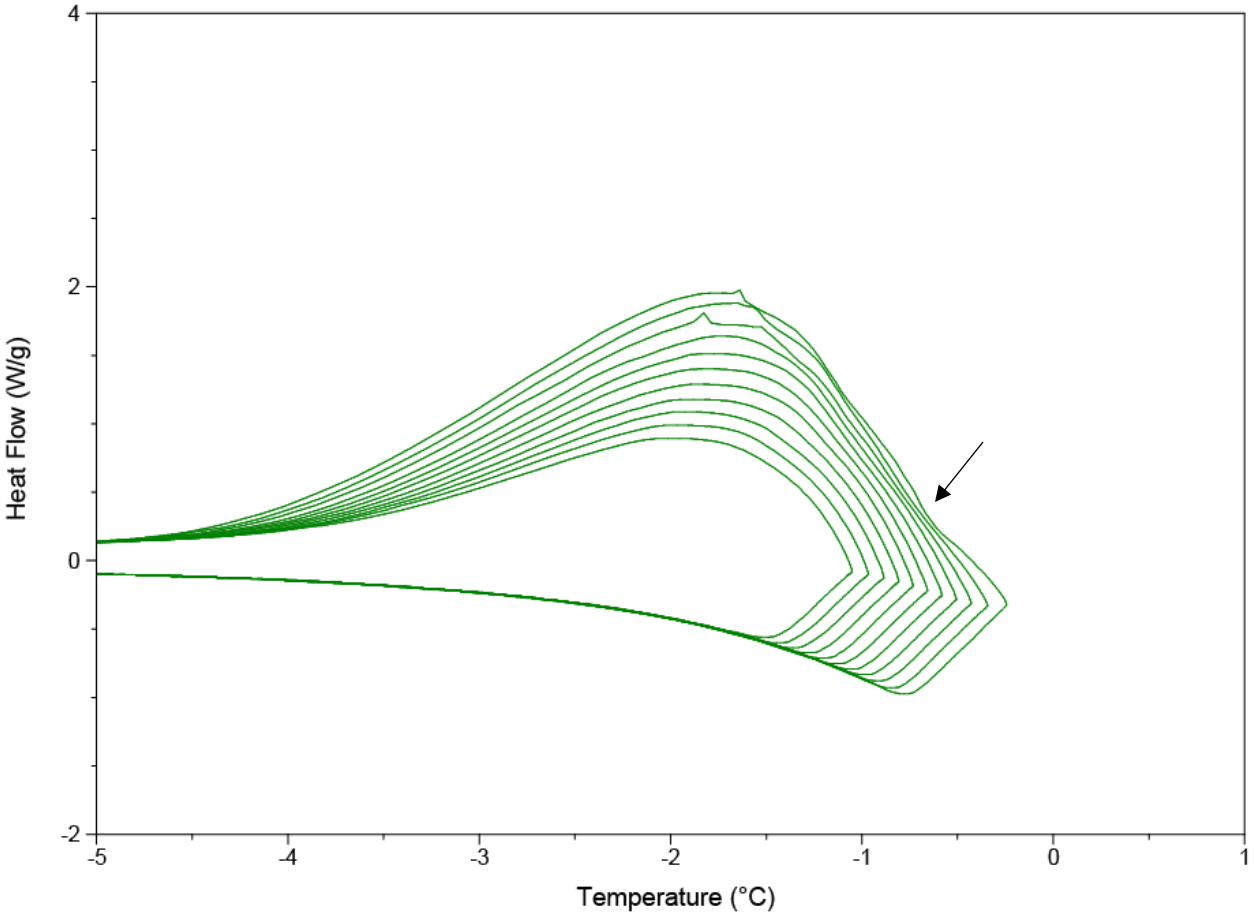

Figure 24: DSC curves of the fusion protein, TrxA-ApAFP752, at 3 mg mL^{-1} concentration. The black arrow indicates the onset of freezing in the sample. The thermal hysteresis activity was found to be -0.36 °C at an ice fraction of 10.5%.

Table 1: Results of DSC thermal hysteresis experiments on TrxA-ApAFP752. A concentration of 5 mg mL^{-1} yielded the highest thermal hysteresis activity. The sample was also found to have the largest ice fraction of all the samples. A smaller ice fraction may result in a greater activity.

Concentration (mg mL^{-1})	Concentration (μM)	ΔH_r (J/g)	ΔH_m (J/g)	THA (°C)	Ice Fraction (%)
1	37.9	-332.8	300.4	-0.30	10.8
3	113.6	-325.3	294.4	-0.36	10.5
5	189.39	-305.5	268.4	-0.39	14.0

An additional study was carried out on a TrxA-ApAFP752 sample to study the role the protein's tertiary structure plays in thermal hysteresis activity. A TrxA-ApAFP752 sample at a concentration of 3 mg mL^{-1} was heated to 85.0 °C for 10 minutes in order to denature the protein. DSC data was collected on the heat-denatured fusion protein using the same method describe above. The heat-denatured sample showed no signs of thermal hysteresis activity (Figure 25), indicating that the fold of the protein plays a critical role its ability to interact with ice, thereby affecting its thermal hysteresis activity.

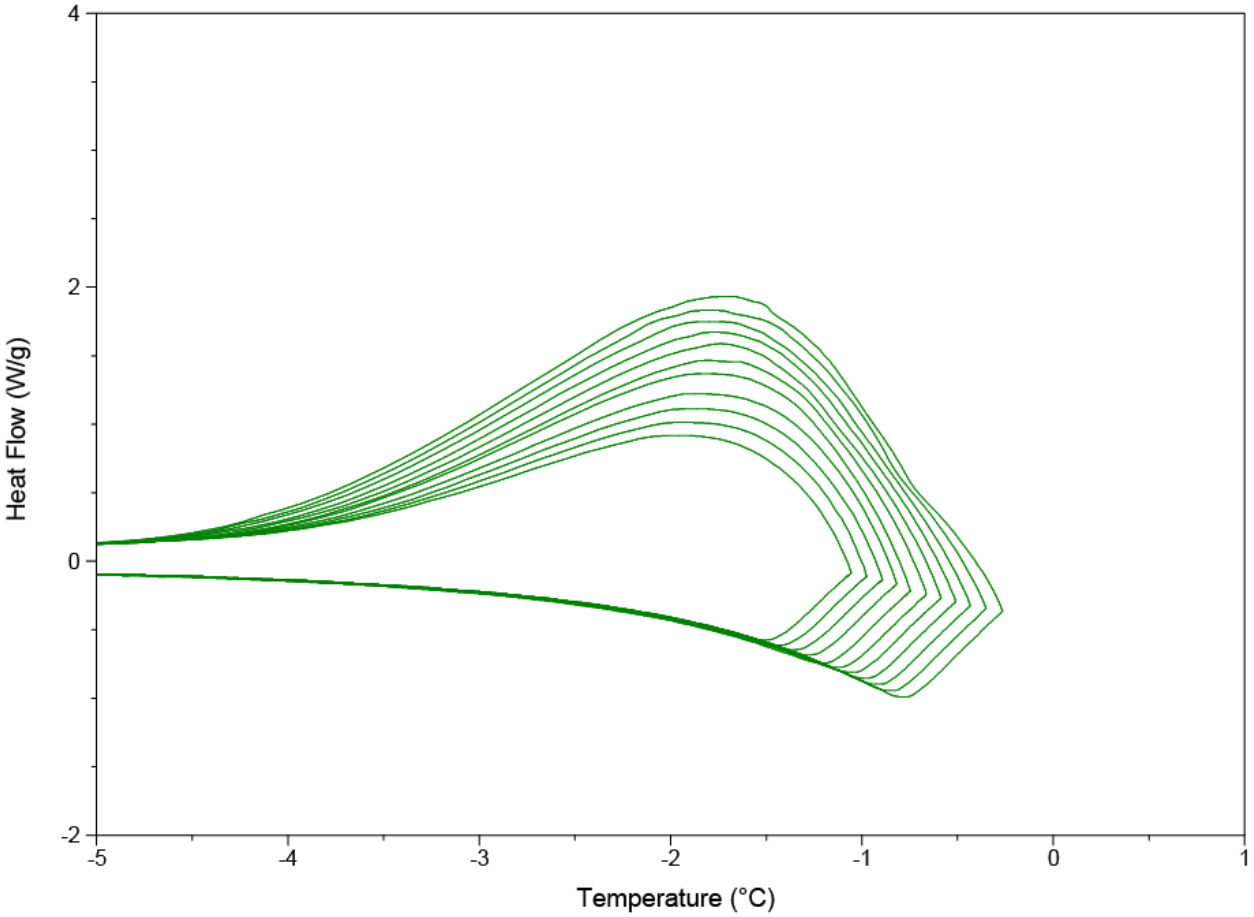

Figure 25: DSC curves for a heat denatured sample of TrxA-ApAFP752 at 3 mg mL^{-1} treated at 85 °C for 10 minutes. The sample exhibits no thermal hysteresis activity.

Thermal hysteresis activity experiments were also carried out on samples of the non-fusion form of the antifreeze protein ApAFP752. Samples of ApAFP752 at

concentrations of 1 mg mL^{-1} (106.4 µM) and 3 mg mL^{-1} (319.2 µM) were tested to identify potential differences in thermal hysteresis activity compared to the fusion protein TrxA-ApAFP752. It was found that ApAFP752 at the concentrations of 1 mg mL^{-1} and 3 mg mL^{-1} resulted in thermal hysteresis activities of -0.52 °C (Figure 26) and -0.50 °C (Figure 27), respectively. The percent ice present in each sample was once again calculated using the using the enthalpies of melting and refreezing (See Appendix: Materials and Methods – Differential Scanning Calorimetry), which can be found in Table 2.

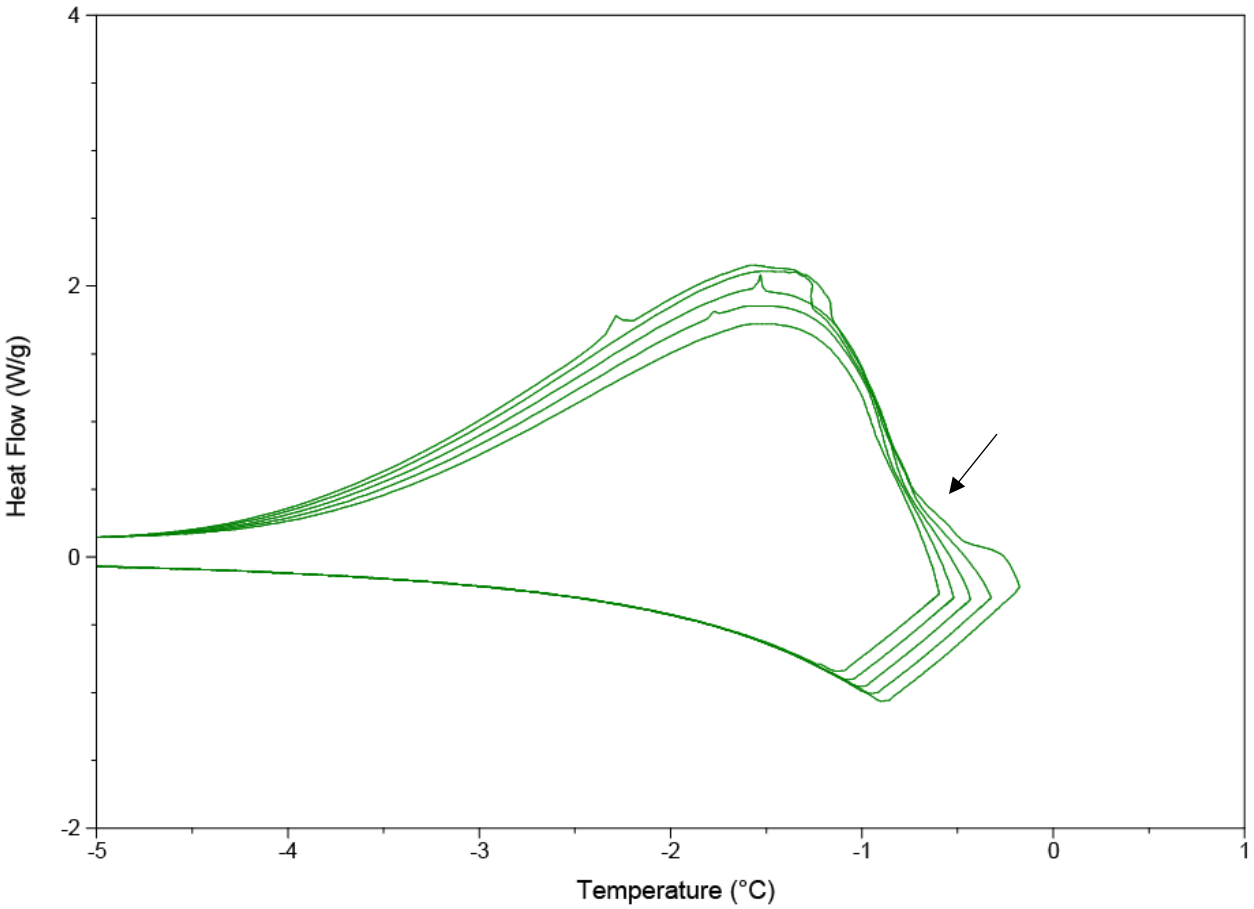

Figure 26: DSC curves for ApAFP752 at 1 mg mL^{-1} (106.4 µM) concentration. The black arrow indicates the onset of freezing in the sample. The thermal hysteresis activity was found to be -0.52 °C at an ice fraction of 15.4%.

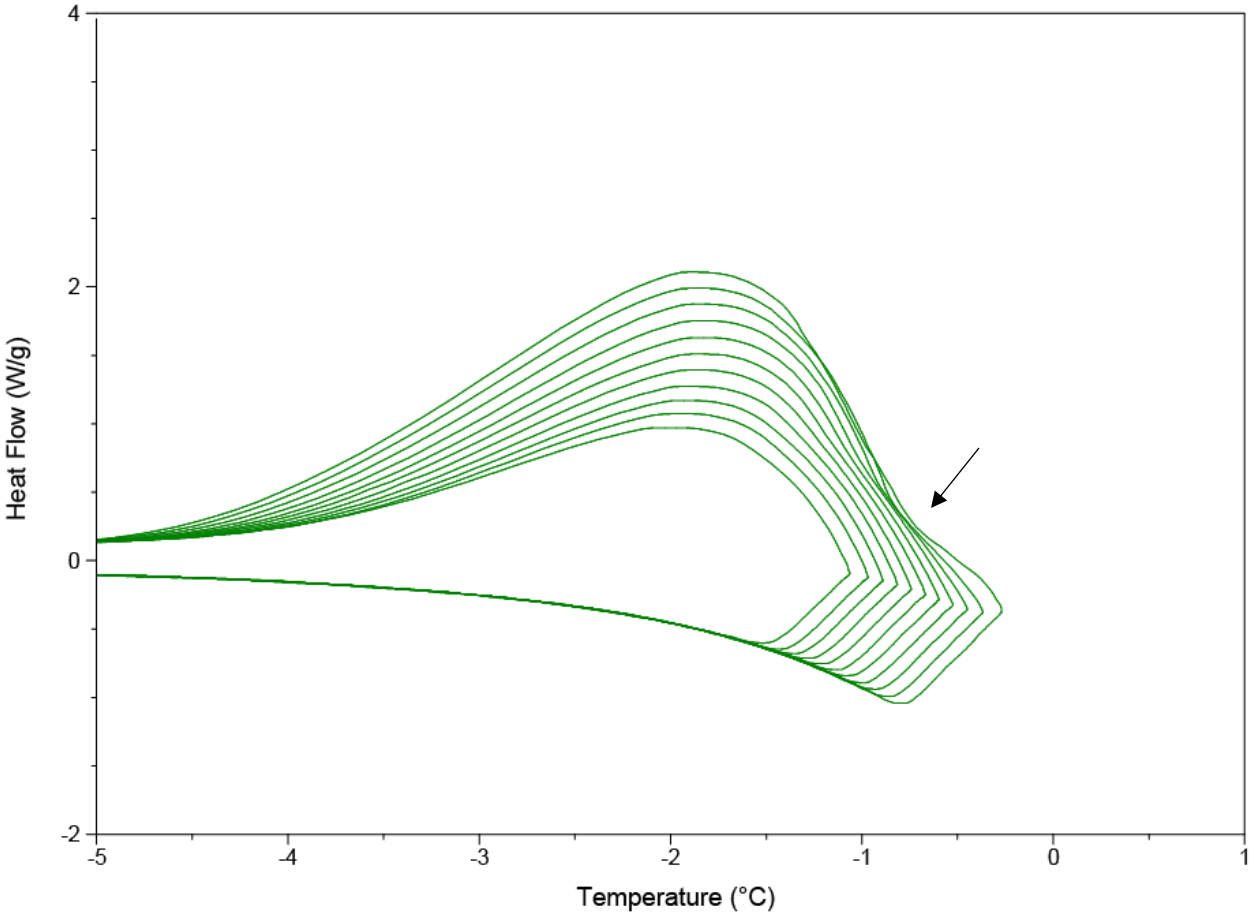

Figure 27: DSC curves for ApAFP752 at 3 mg mL^{-1} (319.2 µM) concentration. The black arrow indicates the onset of freezing in the sample. The thermal hysteresis activity was found to be -0.50 °C at an ice fraction of 18.3%.

Table 2: Results of DSC thermal hysteresis experiments on ApAFP752. A concentration of 1 mg mL^{-1} yielded the highest thermal hysteresis activity. The sample was also found to have the smaller ice fraction of the two samples.

Concentration (mg mL^{-1})	Concentration (µM)	ΔH_r (J/g)	ΔH_m (J/g)	THA (°C)	Ice Fraction (%)
1	106.4	-340.8	295.3	-0.52	15.4
3	319.1	-373.1	315.4	-0.50	18.3

A sample control consisting of 3 mg mL^{-1} concentration bovine serum albumin (Santa Cruz Biotechnology) in the previously described protein buffer was tested as a negative control to verify that the hysteresis activity observed was not due to osmolarity effects. This sample was tested under same conditions as described above. It was found that the bovine serum albumin (BSA) sample exhibited no thermal hysteresis activity (Figure 28). This finding is consistent with published data[43] showing that BSA has no thermal hysteresis activity or antifreeze properties.

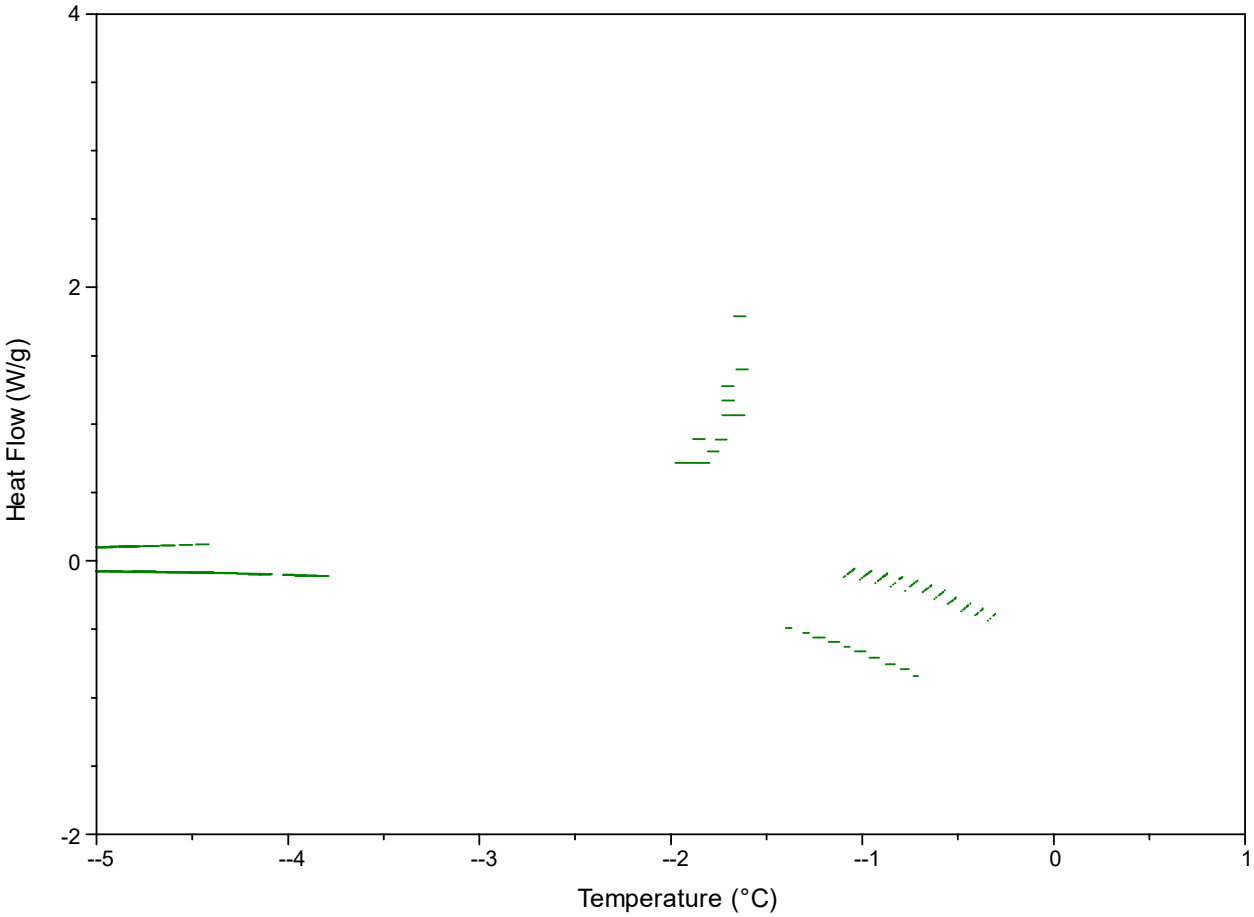

Figure 28: DCS curves for bovine serum albumin prepared at 3 mg mL^{-1}. The sample exhibits no thermal hysteresis activity.

II. Ice Recrystallization Inhibition

As previously stated, in addition to thermal hysteresis, antifreeze proteins possess the ability to inhibit the recrystallization of ice. TrxA-ApAFP752's ice recrystallization inhibition activity was tested in collaboration with Dr. Paul Baures at Keene State College. In order to test the activity, a small amount of sample was loaded into microcapillary tubes and exposed to freeze-thaw cycles. The antifreeze protein containing samples were compared with a protein buffer control of 50 mM potassium phosphate, 20 mM NaCl, pH 8.0 and a non-antifreeze protein control of 100 μM bovine serum albumin (BSA). Ice recrystallization inhibition assays were tested at TrxA-ApAFP752 concentrations of 100 μM, 50 μM and 12.5 μM. Samples were completely frozen and then slowly thawed to be able to visibly monitor the amount of granulation and ice fusion occurring.

It was shown that neither the control samples of buffer or 100 μM BSA showed evidence of ice recrystallization inhibition activity (Figure 29). These results were as expected as neither phosphate salt buffers or BSA are known to have any ice recrystallization inhibition properties. Each of the TrxA-ApAFP752 samples showed some ice recrystallization inhibition activity, with the 100 μM TrxA-ApAFP752 sample exhibiting the greatest activity of the test group. This result was not unexpected as the higher concentration of antifreeze protein results in a higher percentage of nascent ice crystals being bound by the antifreeze protein during freezing and preventing the fusion of these crystals during melting[27,53].

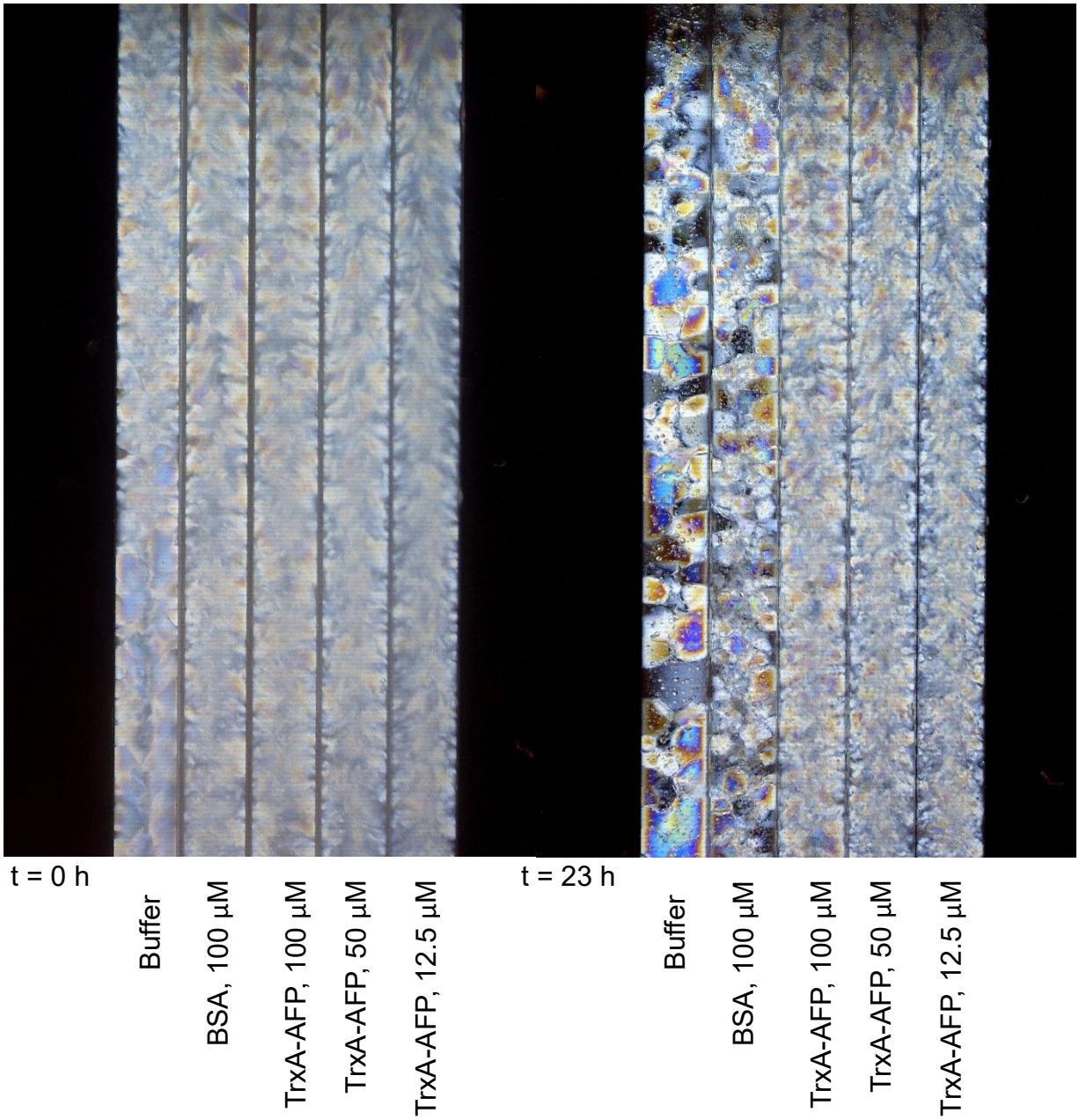

Figure 29: Ice recrystallization inhibition study on the fusion protein, TrxA-ApAFP752. The left figure set shows all 5 samples at the initial freezing where sample is completely frozen. The right figure set shows each sample during the thawing cycle at 23 hours. Both the buffer and BSA samples show no ice recrystallization inhibition. Each TrxA-ApAFP752 sample shows inhibition activity.

III. Cryoprotection of Cells with the Fusion Protein, TrxA-ApAFP752

Since the discovery of antifreeze proteins, several studies have been performed to assess their application as cryoprotectants and cryopreservatives in medicine, agriculture and food[54-57]. In collaboration with Dr. Daniel Levy and Dr. Predrag Jevtic at the University of Wyoming, we investigated the cryoprotective effects of an insect AFP on *Xenopus laevis* eggs and embryos. *X. laevis* is a model organism that has provided fundamental insights into cell and developmental biology and is relatively easy to maintain in the laboratory environment. *X. laevis* eggs and embryos were chosen because they are large (i.e. 1-1.2 mm), easily manipulated by microinjection (e.g. with DNA, mRNA, or protein), and provide an ample source of biochemically active cytoplasmic extracts. Frog embryos develop externally, which allows for experiments to be performed prior to and directly following fertilization. *Xenopus* shares a common evolutionary history with mammals and can serve as an excellent model organism to provide insights into human conditions and diseases[58]. While *Xenopus* eggs and embryos are relatively easy to work with in the laboratory, there have not been any successful reports involving their cryopreservation. Studies have investigated intra- and extracellular ice formation with *Xenopus* oocytes to gain insight into cryopreservation[59,60]. In another study, ectopic expression of the aquaporin-3 channel in *Xenopus* oocytes resulted in plasma membrane permeability to glycerol, ethylene glycol, and propylene glycol[61]. While these studies suggest that cryopreservation of *Xenopus* oocytes and eggs may be possible, effective approaches do not currently exist. Development of cryopreservation protocols would be of great interest to *Xenopus* investigators, allowing for long-term storage of oocytes and eggs (not currently possible) and facilitating studies with single clutches of oocytes and eggs, thereby eliminating

batch-to-batch variability.

Both fertilized and unfertilized *X. laevis* eggs were injected with 50 nL of purified recombinant TrxA-ApAFP752 to a final intracellular concentration of ~5 µM. For control experiments, eggs were microinjected with an equivalent volume of buffer[62]. Microinjected eggs were exposed to a freeze/thaw cycle and imaged. Egg viability was judged based upon post freeze/thaw physical appearance. Eggs exhibiting a white, puffy appearance are those that were damaged during freeze/thaw and did not survive[63-69].

Results of the study show eggs injected with TrxA-ApAFP752 had an increase in survival rate compared to those injected with buffer. Unfertilized eggs showed a 96.0% survival when injected with the antifreeze protein, while the buffer injected eggs only exhibited a 13.2% survival rate (Figure 30). Fertilized eggs injected with the antifreeze protein had an 80.0% survival rate, while the buffer injected had a 30.0% rate of survival (Figure 31).

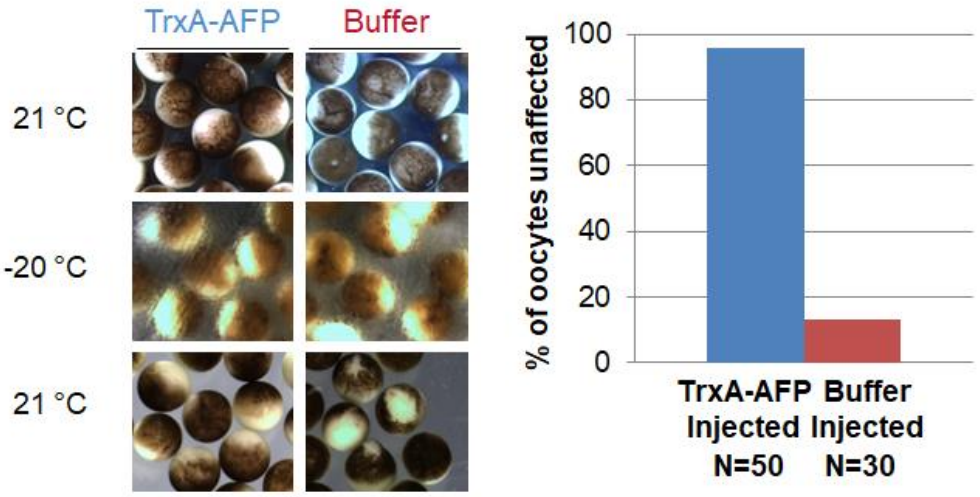

Figure 30: Unfertilized microinjected eggs from *X. laevis*. Eggs injected with TrxA-ApAFP752 had a survival rate of 96.0%. Buffer injected eggs had a survival rate of 13.2%, 7.27 times lower than that of the antifreeze protein study.

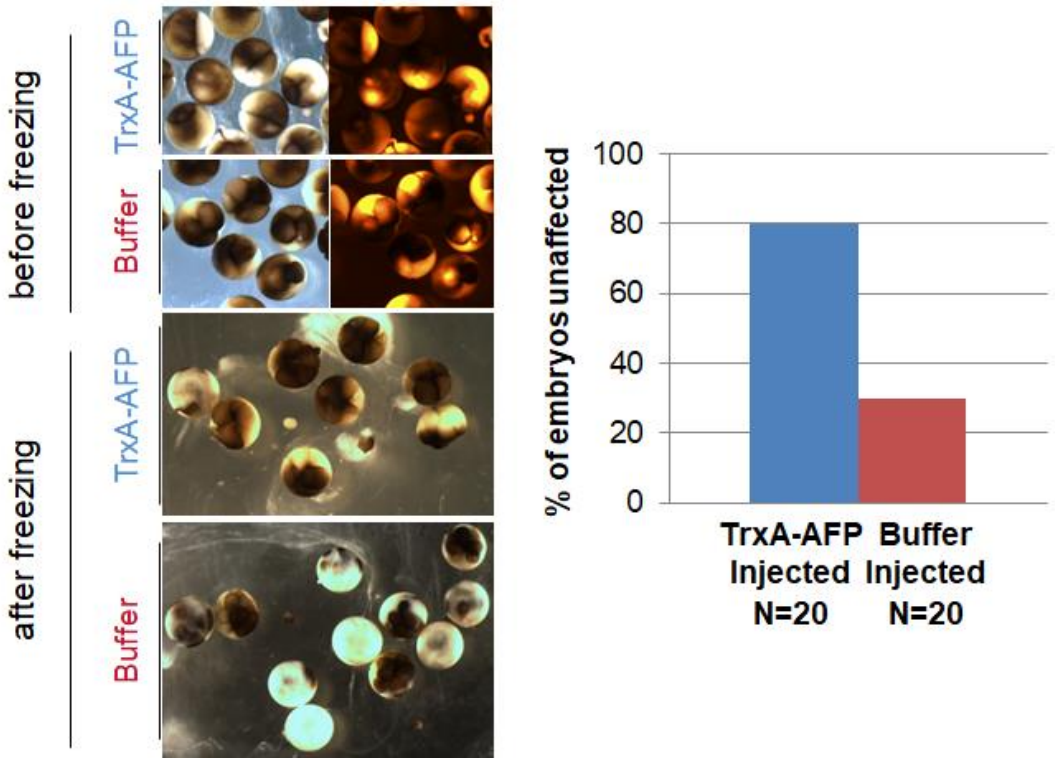

Figure 31: Post fertilization microinjected eggs from *X. laevis*. Eggs injected with TrxA-ApAFP752 had a survival rate of 80.0%. Buffer injected eggs had a survival rate of 30.0%, 2.67 times lower than that of the antifreeze protein study.

Additional studies were performed on *X. laevis* eggs in which one-cell stage embryos were injected with mRNA encoding for the expression of GFP-ApAFP752 or GFP. The eggs were allowed to develop to a later stage in order to allow for the expression of the antifreeze protein and imaged. Eggs containing the GFP-ApAFP752 showed localization of the protein to the membrane. Eggs containing only GFP showed no localization to the plasma membrane (Figure 32). This suggests ApAFP752 may have some interaction with the membrane which may play a further role in its ability to act as an *in vivo* cryoprotectant.

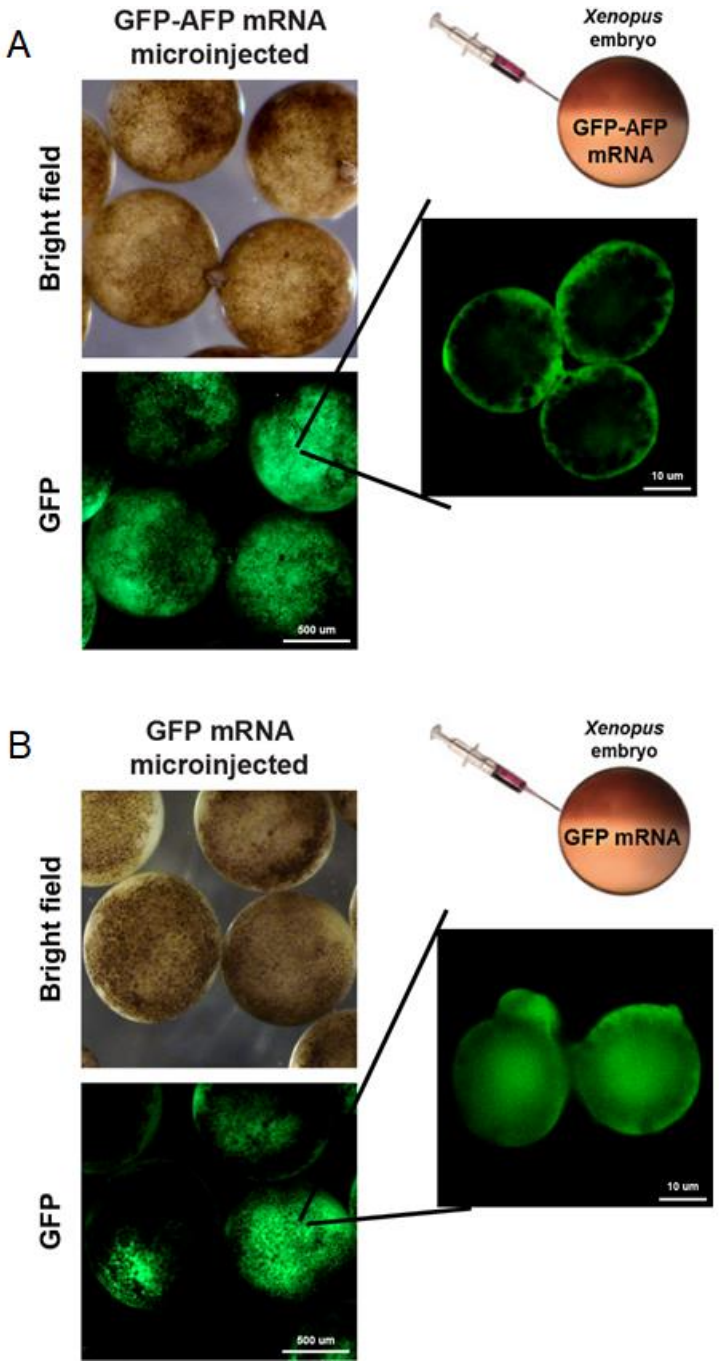

Figure 32: *X. laevis* eggs microinjected with (A) GFP-ApAFP752 mRNA and (B) GFP mRNA. (A) Localization of GFP-ApAFP752 to the membrane portion of the plasma membrane. (B) GFP does not exhibit any visible localization to the plasma membrane.

The cryoprotective capabilities of TrxA-ApAFP752 were further studied in comparison to known chemical cryoprotectants in collaboration with Dr. Irena

Kratochvílová at the Academy of Sciences of the Czech Republic. Human skin fibroblast samples in DMEM medium were mixed with either 0.5 mg mL^{-1} TrxA-ApAFP752, 3.2 % w/w trehalose, 10 % w/w DMSO or a combination of 10 % w/w DMSO and 3.2 % w/w trehalose. The samples were then cooled to -80 °C at a rate of -1 °C min^{-1} and stored at -80 °C for 24 hours. The samples were then thawed, and the viability was evaluated using flow cytometry.

It was found that the cells mixed with DMSO and trehalose had the highest viability at 85.6 %, while the cells mixed with TrxA-ApAFP752 had the lowest viability after freeze-thaw at 32.3 %. 80.7 % of cells mixed with DMSO were viable and 58.5 % of cells mixed with trehalose were viable after freeze-thaw (Figure 33). These results are not unexpected as DMSO is able to penetrate and accumulate in the cell cytoplasm[70] and trehalose is able to enter the cell via pinocytosis[46]. TrxA-ApAFP752 is not able to freely pass through the cell membrane, thus, the cryoprotective effects of the antifreeze protein were entirely external to the cell. It is worth mentioning that the antifreeze protein, while resulting in the lowest survival rate of the tested cryoprotectants, did result in a higher rate of survival than that of the control sample.

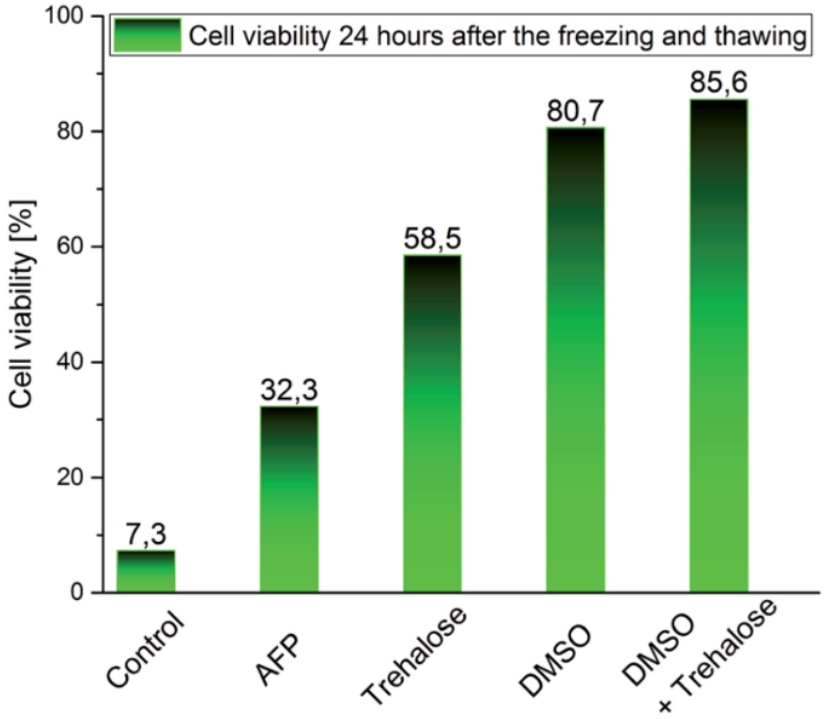

Figure 33: Human skin fibroblast viability after 24 hours mixed with various cryoprotectants. Cell viability was assessed with flow cytometry. Samples exposed to DMSO and trehalose experienced higher survival rates as the cryoprotectants were inside and outside of the cells. TrxA-ApAFP752 was only external to the cells.

IV. Conclusion

Both TrxA-ApAFP752 and ApAFP752 exhibited levels of thermal hysteresis activity. TrxA-ApAFP752 was found to exhibit ice-recrystallization inhibition activity. Our data has shown that the TrxA-ApAFP752 (ApAFP752 joined with thioredoxin) fusion protein does confer partial cryoprotection to *Xenopus* oocytes and human skin fibroblast cells. Our results also suggest that one of the mechanisms by which antifreeze proteins protect cells during freeze/thaw is by protecting the cell membranes. Future studies will focus on determining the ice-recrystallization inhibition activity of ApAFP752 along identifying the mechanism by which the antifreeze protein interacts with cells membranes.

CHAPTER 4

STRUCTURAL STUDIES OF ApAFP752

Nuclear magnetic resonance spectroscopy is a powerful tool in structural biology as it provides useful information in determining the stability, fold, structure and interactions of proteins and their substrates. There have been numerous AFP structures solved and AFPs characterized using NMR techniques[71-74]. As of July 13, 2018, there are 12,282 protein structures reported as solved by NMR spectroscopy in the Protein Data Bank[75]. In this chapter we will examine **Project 1, Aim 1: Structural characterization of ApAFP752 antifreeze protein by solution NMR spectroscopy** (see "Project Aims and Hypothesis"). We have utilized NMR spectroscopy techniques in order to better understand the structural characteristics associated with the protein ApAFP752. In order to study the protein using NMR, ApAFP752 was expressed using stable isotopes of ^{13}C and ^{15}N. Protein samples were purified and isolated as previously mentioned. The resulting ApAFP752 samples were concentrated to a minimum of 350 μM and packed into D_2O matched Shigemi® NMR tubes. ApAFP752 NMR data was acquired at the City University of New York's Advanced Science Research Center, the University of Wyoming and Brandeis University.

I. Backbone and Side-Chain Assignments

As previously stated, a ^{1}H-^{15}N heteronuclear single quantum coherence (HSQC) spectrum was collected as an initial assessment of protein fold and stability. The spectrum

showed well dispersed peaks with relative uniformity in peak intensity and signal (Figure 34). Upon confirmation of protein stability, a standard set of 3-dimensional (3D) NMR spectra were acquired for assignments.

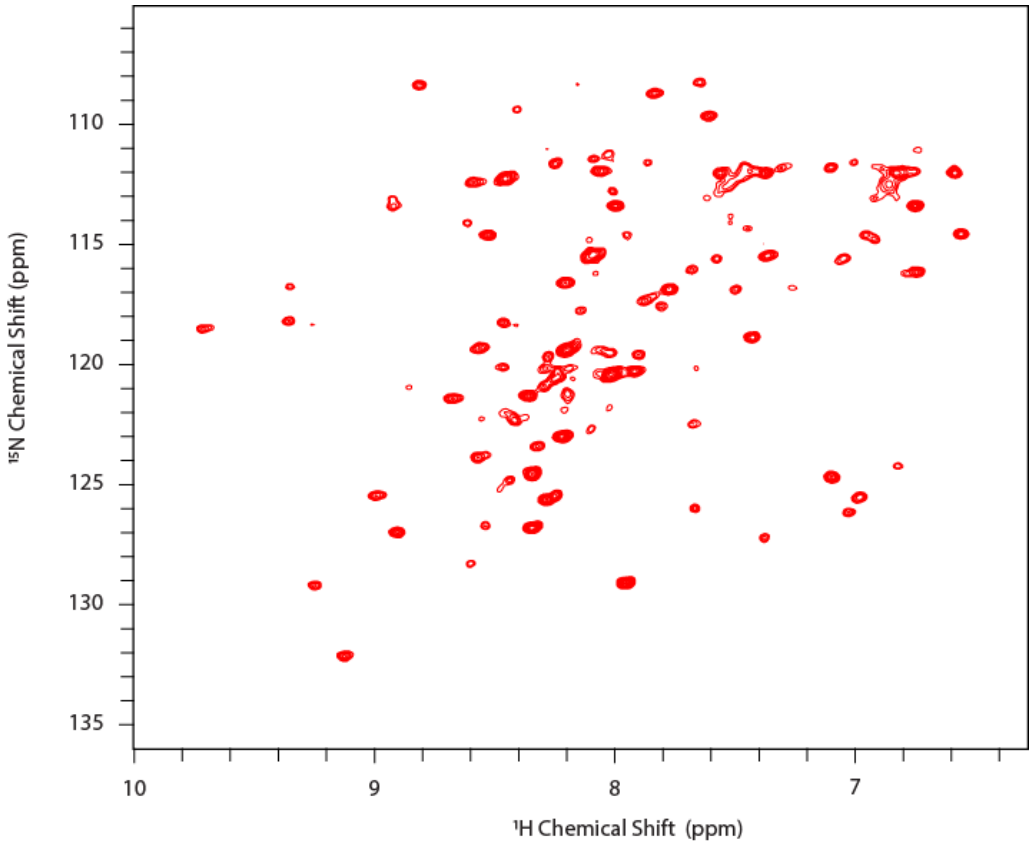

Figure 34: ^{1}H-^{15}N HSQC spectrum of ApAFP752. Each peak indicated either a backbone or side-chain N-H correlation.

The prerequisite of structure determination is spectral assignment, i.e. each peak in the spectrum must be assigned to a specific residue in the protein sequence. Assignments are accomplished based on known characteristic chemical shifts and connectivity patterns of the 20 amino acids and chemical shift connectivity in complementary NMR spectra. The following backbone and side-chain experiments were collected and used to assign the amino acid residues of the uniformly-^{15}N, ^{13}C enriched ApAFP752: ^{1}H-^{15}N HSQC, HNCA, HNCO, HNCACB, CBCA(CO)NH, HN(CO)CA,

CC(CO)NH, HAHBNH, H(CCO)NH (Figure 35). Most acronyms correlate to the magnetization transfer pathway and the resonances that can be identified in each spectrum. For instance, in 3D HNCA experiment, the magnetization of the amide ^{1}H is transferred to the directly bonded amide ^{15}N of the *i* residue and in the next step to the $^{13}C\alpha$ of both the *i* residue and the *i*-1 (previous residue) in the protein's amino acid sequence. Thus, the HNCA spectrum has three chemical shift axes (^{1}H, ^{15}N and ^{13}C) and contains peaks that encode chemical shift data of amide ^{1}H and ^{15}N correlating with $^{13}C\alpha$ of both the *i* and *i*-1 residues. The HNCACB spectrum correlates the amide ^{1}H and ^{15}N of the *i* residue with $^{13}C\alpha$ and the $^{13}C\beta$ of the *i* and *i*-1 residues. The advantage of the HNCACB spectrum is that it contains more information (it encodes the $^{13}C\beta$ resonance in addition to the $^{13}C\alpha$), however the experiment has lower sensitivity and the spectrum typically has lower signal-to-noise. The parentheses in the experimental names, i.e. CBCA(CO)NH, signify that the magnetization transfer pathway included those atoms (in this case the carbonyl, ^{13}CO), however the chemical shift information for these atoms is not encoded in the spectrum. Figure 36 shows an example of the 3D HNCA (amide ^{1}H, ^{15}N, and $^{13}C\alpha$ correlation) spectrum ‘backbone walk’ of the ApAFP752 protein, an assignment strategy to link protein backbone atoms with their sequential amino acid neighbors.

Backbone and side-chain data was acquired at the City University of New York’s Advanced Science Research Center on a Bruker Avance III 800 MHz NMR spectrometer equipped with a triple resonance TCI cryoprobe. All NMR data was processed using the NMRPipe[76] software package available through the National Institute of Standards and Technology (NIST). Spectra were analyzed using the NMRFAM-Sparky[77] software

package available through the National Magnetic Resonance Facility at Madison (NMRFAM).

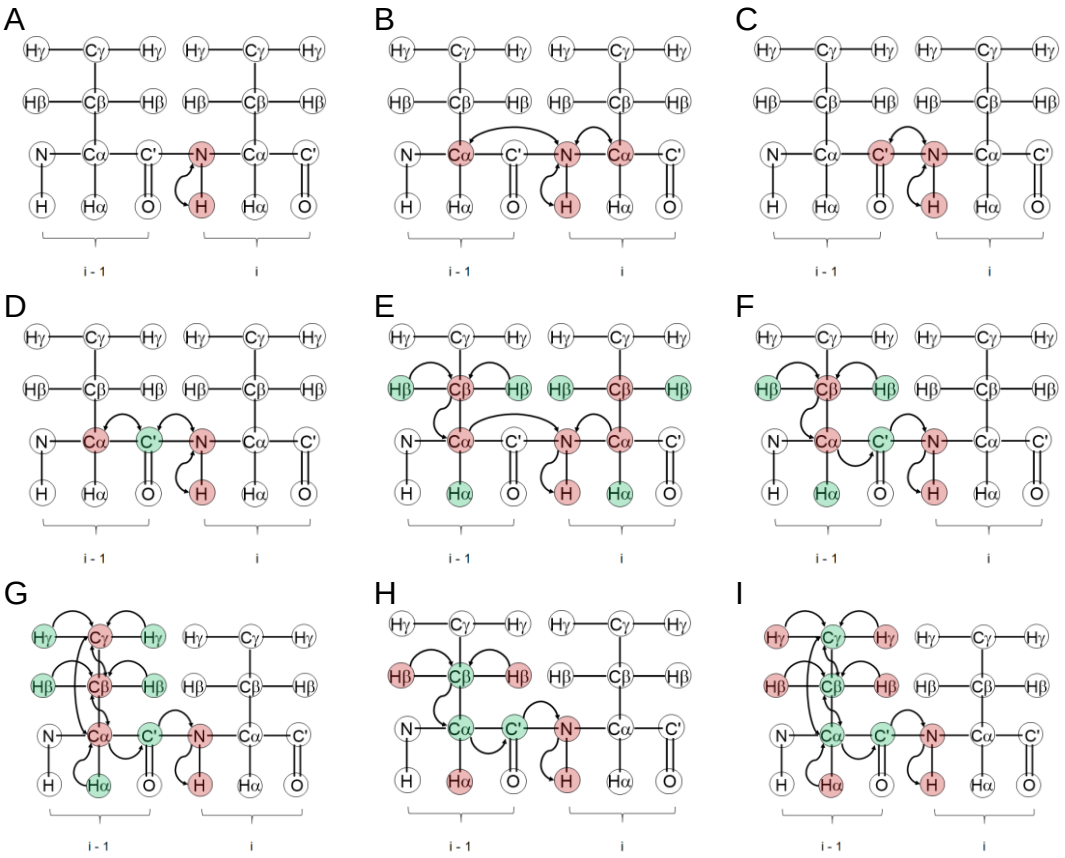

Figure 35: Depiction of NMR backbone and side-chain experiments used to complete the assignments. A) ^{1}H-^{15}N HSQC, B) HNCA, C) HNCO, D) HN(CO)CA, E) HNCACB, F) CBCA(CO)NH, G) CC(CO)NH, H) HAHBNH, and I) H(CCO)NH. Red indicates resonances detected in the experiment. Green indicates resonances not detected by the experiment.

Initial prediction of the chemical shift assignments was made using the I-PINE web server at NMRFAM[78]. Refinement of the I-PINE assignments was performed using chemical shift statistical data available through the Biological Magnetic Resonance Data Bank (BMRB) and data published by Wang and Jardetzky[79]. Chemical shifts of the

backbone spectra were used to assign individual amino acid residues within the protein (Figure 36). Proton side-chain spectra and ^{1}H-^{15}N NOESY-HSQC spectra were used to both confirm backbone assignments and to assign the protons in the side-chain residues. Currently, 91 % of ApAFP752 resonances have been assigned. A full list of the assigned residues can be found in the Appendix under the “Chemical Shift Assignment Table” section. Completion of the assignments is in progress and additional NMR spectra are being acquired to aid in this endeavor. A preliminary structure for the protein using the current assignments has been calculated (Chapter 4.II Structural Characterization of ApAFP752 by NMR Spectroscopy).

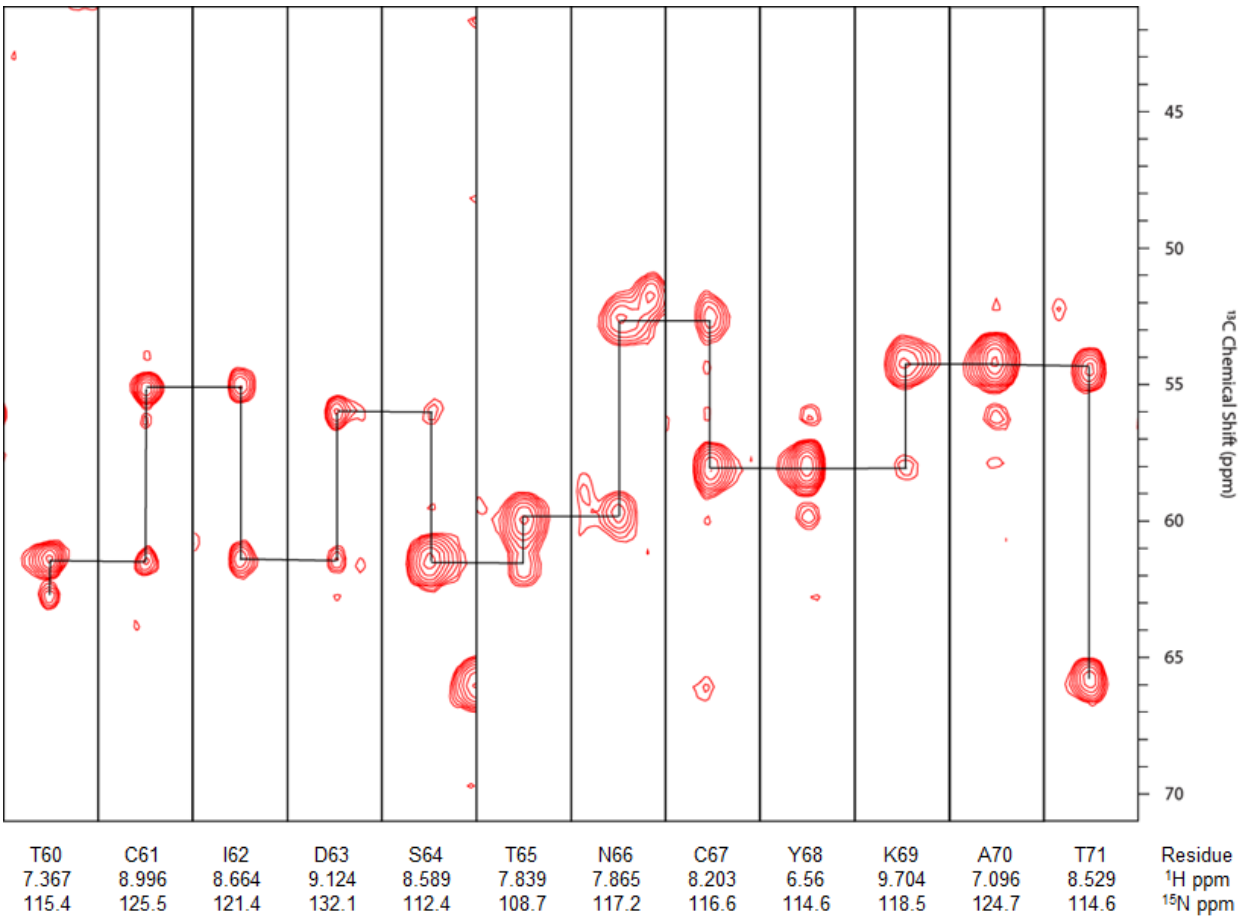

Figure 36: HNCA strip plot showing the Cα chemical assignments for residues T60 through T71 of ApAFP752. HNCA strip plot demonstrates the “backbone walk” for the assignment by linking the *i* and *i*-1 residues through matching Cα chemical shifts. It must be noted that the Cα chemical shifts for C67 and Y68 overlap in the Y68 strip. The same occurs with the Cα chemical shifts for K69 and A70 in the A70 strip. This was confirmed with the use of the CBCA(CO)NH and HN(CO)CA experiments.

II. Structural Characterization of ApAFP752 by NMR Spectroscopy

A preliminary structure of the protein ApAFP752 was calculated using CS-Rosetta[80,81] using backbone and side-chain resonance assignments. The preliminary structural calculations yielded a protein with right handed β-helix secondary structure

(Figure 37). Probabilistic secondary structure calculations using PECAN were performed to corroborate the structural data obtained with CS-Rosetta[82]. The PECAN data indicates the protein has a high probability of β-sheet motifs as well as α-helix motifs (Figure 38). Structural calculations show the interhelical distances between the β-sheets to be between 4.81 Å and 5.00 Å. Distances from threonine Cα to threonine Cα in the TCT repeats were revealed to be 6.86 Å and 6.97 Å. These findings are similar to the previously predicted homology model produced by Mao and collaborators[35]. Additionally, the predicted β-helix is in similar to that of other known insect antifreeze proteins. It has been reported that the intermolecular distance between waters along the c-axis is 7.5 Å and 4.5 Å along the a-axis. While the predicted threonine to threonine distances of ApAFP752, both intra-strand and interhelical, are not a perfect match to the intermolecular distances of water, they are very close. This indicates that the protein is capable of binding to both planes of ice similar to other insect antifreeze proteins. Additional structure refinement is currently being performed.

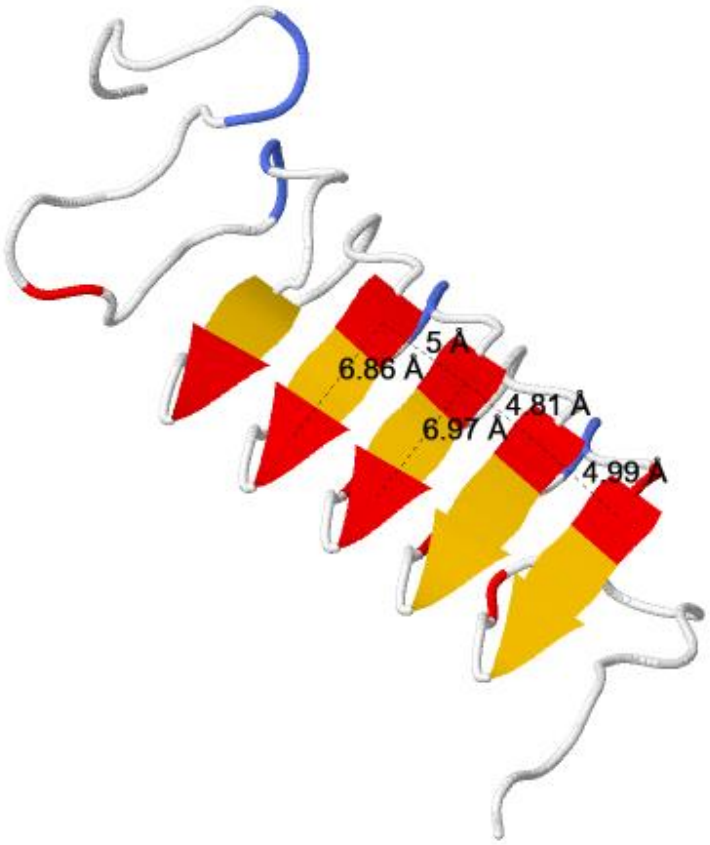

Figure 37: Ribbon backbone diagram of ApAFP752. B-sheet sections are shown in yellow with the threonine residues highlighted in red. Distance measurement were performed using Jmol[83].

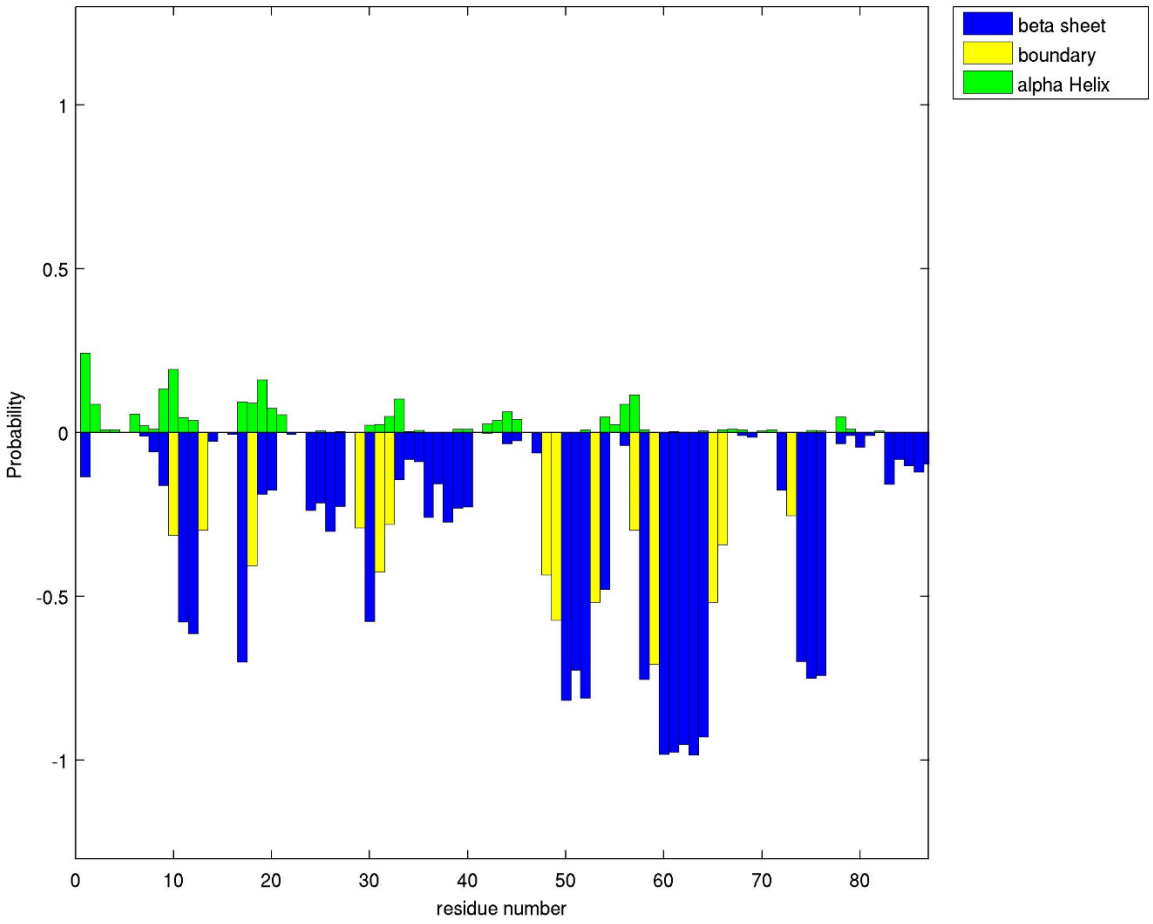

Figure 38: The probabilistic secondary structure of ApAFP752 calculated using PECAN[82]. Blue indicates the probability a given residue is in an extended state (β-sheet). Green is the probability a given residue is in an α-helical state. Yellow indicates the probability the given residue is a boundary residue in either an extended or helical region.

The Cα, Cβ and CO chemical shifts are sensitive reporters of protein secondary structure[84]. Secondary chemical shift statistical analyses were performed in NMRFAM-Sparky[77]. Chemical shifts were compared to the BMRB chemical shift statistics of random coil amino acids. The secondary chemical shift of a given protein nucleus "*i*" is defined as $\Delta\sigma_S^i = \sigma_{obs}^i - \sigma_{r.c.}^i$, where σ_{obs}^i is the chemical shift observed and $\sigma_{r.c.}^i$ is the chemical shift of corresponding nucleus in a random coil state[85]. The secondary chemical shift provides valuable insight in predicting the secondary structure of a protein[85]. Secondary chemical

shift analysis was performed on the ^{1}H-N, C' (carbonyl) and Cα resonances. The ^{1}H-N (Figure 39), C' (Figure 40) and Cα (Figure 41) secondary chemical shifts for ApAFP752 reveal the majority of the residues are associated with a helical state with some of the residues being associated with a β-strand state[79]. While this does not guarantee the secondary structure is that of a β-helix, it does give further merit to the secondary structure of ApAFP752 calculated in CS-Rosetta.

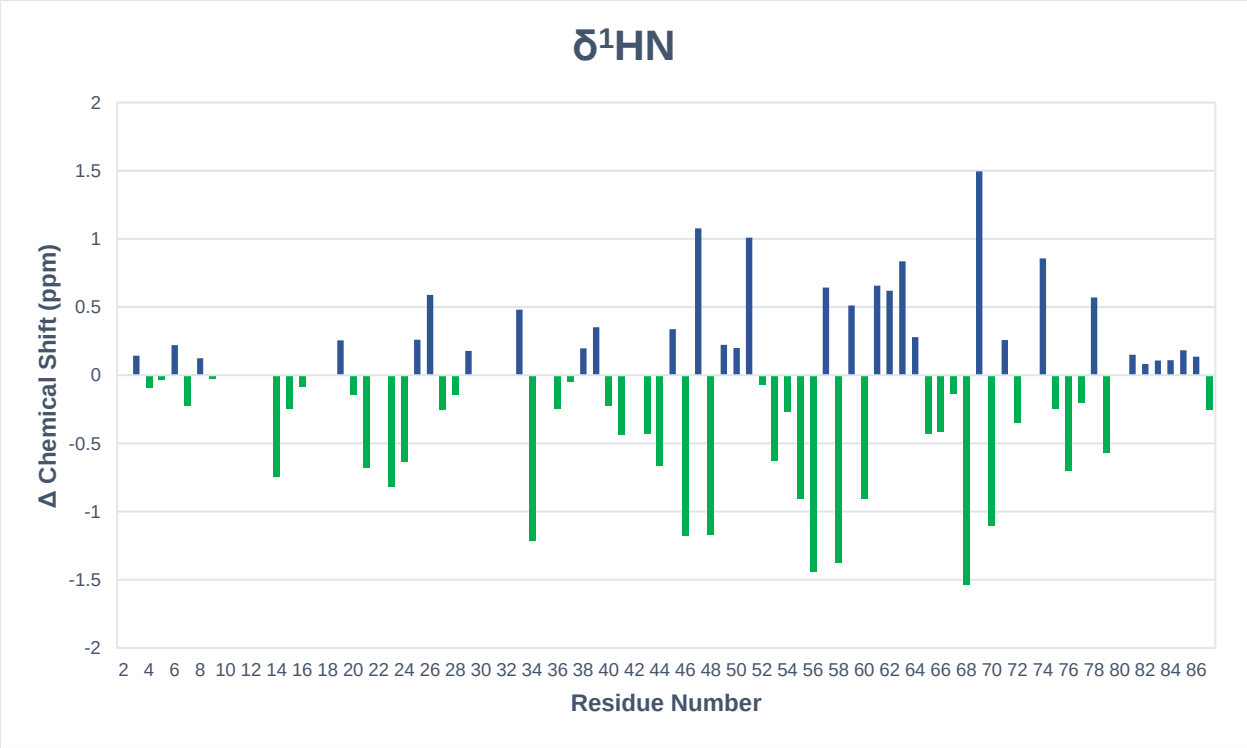

Figure 39: ^{1}HN secondary chemical shift data for ApAFP752. Green bars in the negative region generally indicate residues potentially in an α-helix state[79]. Exceptions include Cys (reduced and oxidized), Glu, Gly, Ile, Phe, Trp, Tyr and Val. Blue bars in the positive region indicate residues potentially in a β-strand conformation. Exceptions are the same as those previously listed. Residues that do not show either blue or green (ΔCS=0) are residues that have yet to be assigned.

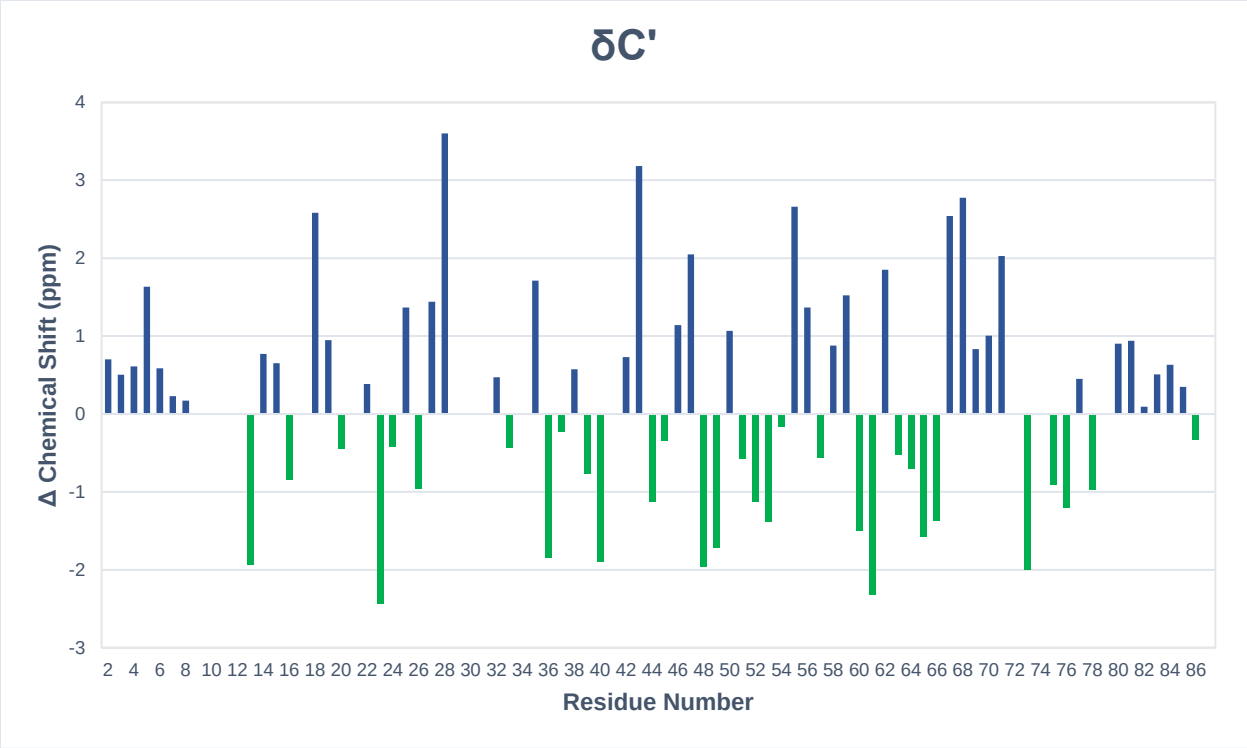

Figure 40: Carbonyl backbone secondary chemical shift data for ApAFP752. Green bars in the negative region indicate residues potentially in a β-strand state[79]. Blue bars in the positive region indicate residues potentially in an α-helix state. Residues that do not show either blue or green (ΔCS=0) are residues that have yet to be assigned.

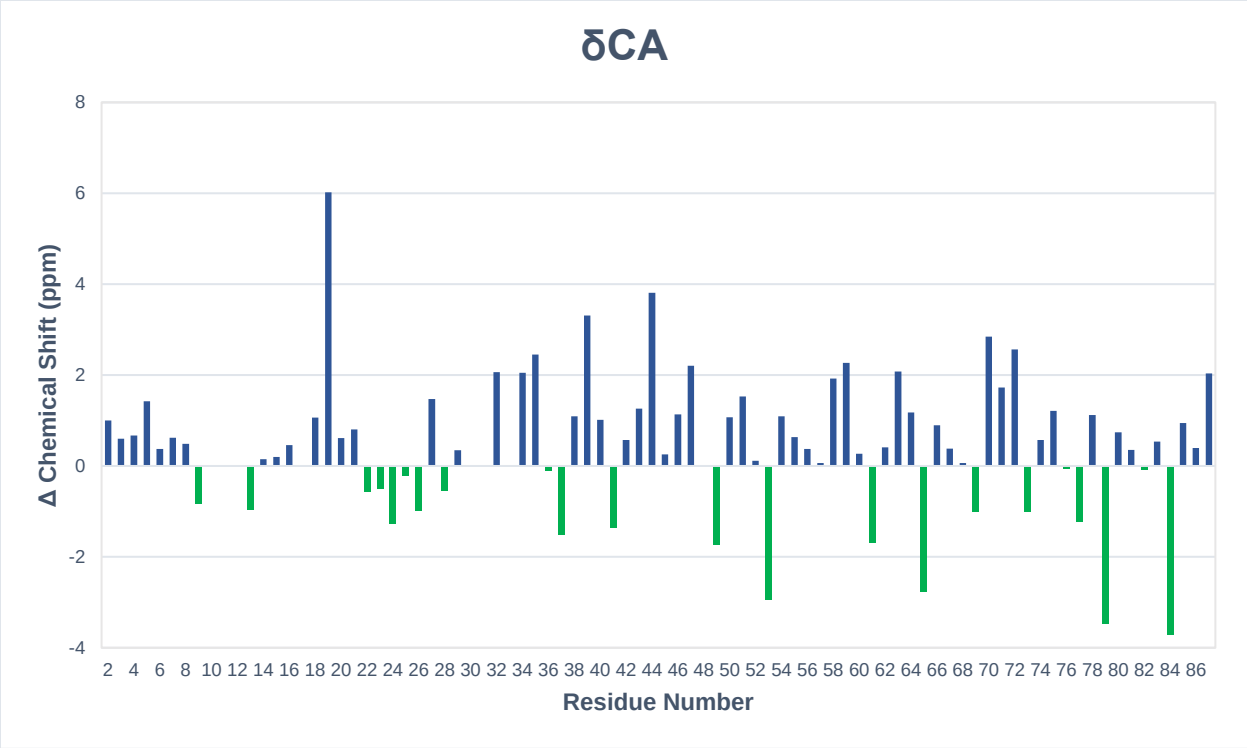

Figure 41: Cα secondary chemical shift data for ApAFP752. Green bars in the negative region indicate residues potentially in an α-helix state[79]. Blue bars in the positive region indicate residues potentially in a β-strand state. Oxidized Cys is an exception to both cases as both the α-helix and β-strand states typically have secondary chemical shifts greater than random coil states. Residues that do not show either blue or green (ΔCS=0) are residues that have yet to be assigned.

III. Hydrogen Bonding Characteristics and Structure of ApAFP752 as an Effect of Temperature

A series of temperature studies were carried out on ApAFP752 in order to see the effects on the secondary structure of the protein and to obtain information on hydrogen bonding. Circular dichroism (CD) spectroscopy experiments were collected at temperatures ranging from 0 °C to 44 °C. ^{1}H-^{15}N HSQC NMR spectroscopy experiments were acquired at temperatures ranging from 5 °C to 45 °C. NMR spectroscopy experiments were not acquired at 0 °C due to the possibility of micro-ice crystal formation. CD and NMR temperature study data was collected at the University of Wyoming. NMR

data was collected on a Bruker Avance III 600 MHz NMR spectrometer equipped with a TXI triple resonance probe. CD data was collected on a JASCO circular dichroism spectrometer.

The NMR spectra revealed linear chemical shift perturbations occurring with every temperature change. These chemical shift perturbations in the proton and nitrogen dimension indicate some form of protein-solvent surface interactions[86] (Figure 42A). In order to rule out that large chemical shift changes were caused by potential protein unfolding, CD spectra were acquired. The CD data showed minimal change in the spectrum between temperatures, indicating the protein did not undergo a change in secondary structure (Figure 42B). This finding is consistent with studies reported by Hong[87] and colleagues in which they state that the amide $^{1}H^{N}$ chemical shift temperature coefficient primarily arises from the hydrogen bond distance change. This coefficient can be the product of intermolecular and intramolecular hydrogen bond distance changes. To this end, amide $^{1}H^{N}$ chemical shift temperature coefficients ($\Delta\sigma H^{N}/\Delta T$) were calculated for each residue using NMR data collected at temperatures of 5 °C, 15 °C, 25 °C, 35 °C and 45 °C. Figure 43 shows residues Ile[5], Gln[41], Thr[48], Lys[69], Cys[79], Val[85] and Lys[87] having the largest chemical shift temperature coefficients. This indicates that these residues experience the greatest change in hydrogen bonding distance per degree Celsius, which indicates solvent exposure.

A

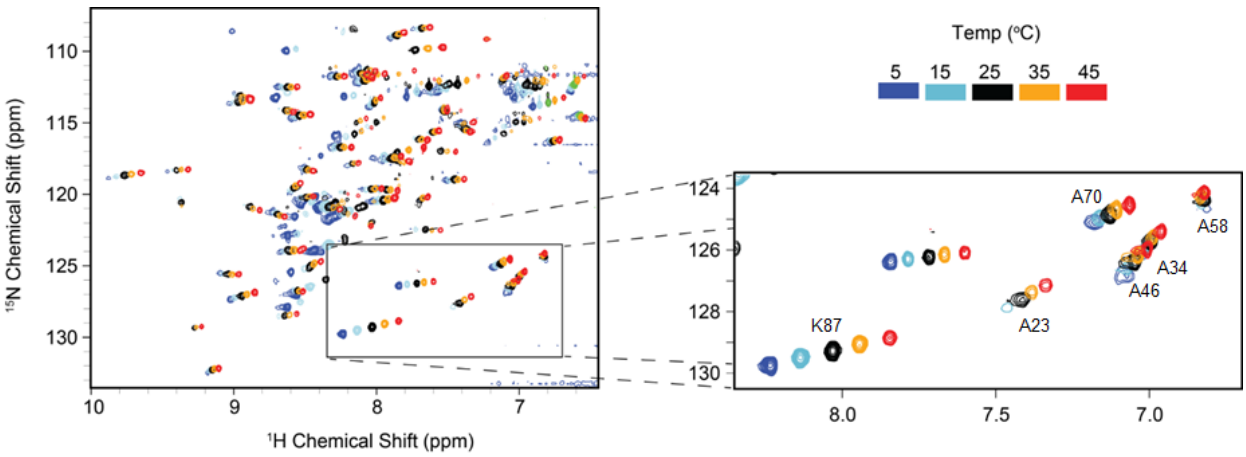

B

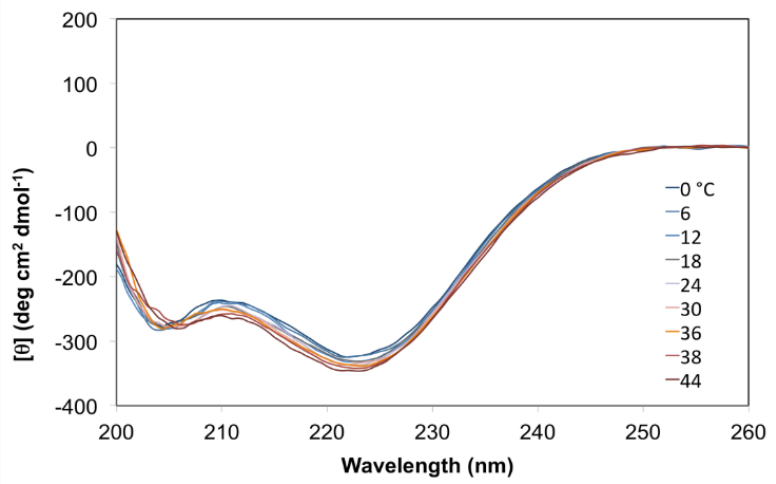

Figure 42: Temperature studies on ApAFP752. A) ^{1}H-^{15}N HSQC spectra collected at temperatures from 5 °C to 45 °C. The highlighted section shows the alanine residues experience large chemical shift perturbations between each temperature. B) Circular dichroism spectra collected from 0 °C to 44 °C. Minimal change in each spectrum between each temperature.

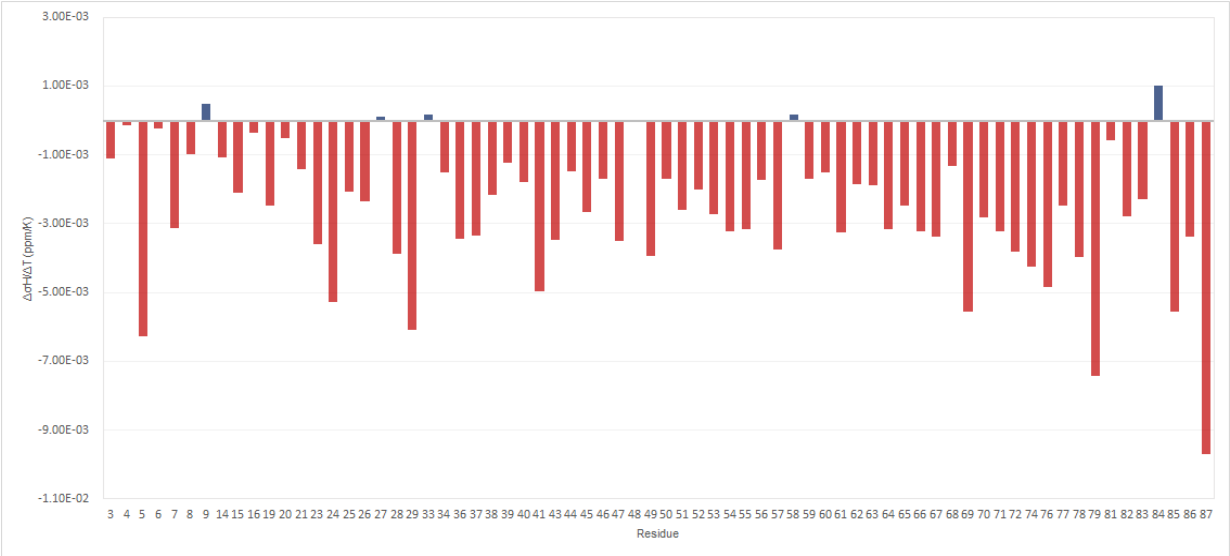

Figure 43: Residue specific amide $^{1}H^{N}$ chemical shift coefficients for ApAFP752 derived from the $^{1}H^{N}$ chemical shifts measured at temperatures of 5 °C, 15 °C, 25 °C, 35 °C and 45 °C.

IV. Conclusion

Our results show that the antifreeze protein ApAFP752 has a β-helical secondary structure, similar to other known insect antifreeze proteins, which plays a role in the protein's ice-binding properties. Using NMR spectroscopy, a preliminary structure of the antifreeze protein was calculated with CS-Rosetta and shows a right handed β-helix, which is also consistent with the predicted homology model. The spacing between the interhelical and intra-strand threonines is consistent with the spacing of waters in ice along the a-axis and c-axis, respectively. Additional refinement of the protein structure is underway using NOESY spectra for additional distance constraints. Temperature studies

of ApAFP752 show the protein does not experience any significant changes in secondary structure at lower temperatures, however, it does experience temperature related changes in hydrogen bonding distances.

CHAPTER 5

IONIC LIQUIDS AND PROTEINS

The effects of high concentrations of ionic liquid on GB1 protein structure and dynamics probed by high-resolution magic-angle-spinning NMR spectroscopy

Lisa Warner,[a,b] Erica Gjersing,[a] Shelby E. Follett,[c] K. Wade Elliott,[c,e] Sergei V. Dzyuba,[d] and Krisztina Varga[c,e*]

[a] National Renewable Energy Laboratory, Golden, CO, 80401, USA

[b] Current address: Biomolecular Research Center, Boise State University, Boise, ID 83725-1511, USA

[c] Department of Chemistry, University of Wyoming, Laramie, WY, 82071, USA

[d] Department of Chemistry and Biochemistry, Texas Christian University, Fort Worth, TX, 76129 USA

[e] Current address*:* Department of Molecular, Cellular, and Biomedical Sciences, University of New Hampshire, Durham, NH, USA

[*] Corresponding author; Email: krisztina.varga@unh.edu

Ionic liquids have great potential in biological applications and biocatalysis, as some ionic liquids can stabilize proteins and enhance enzyme activity, while others have the opposite effect. However, on the molecular level, probing ionic liquid interactions with proteins, especially in solutions containing high concentration of ionic liquids, has been challenging. In the present work the ^{13}C, ^{15}N-enriched GB1 model protein was used to demonstrate applicability of high-resolution magic-angle-spinning (HR-MAS) NMR spectroscopy to investigate ionic liquid –protein interactions. Effect of an ionic liquid (1-butyl-3-methylimidazolium bromide, [C_4-mim]Br) on GB1 was studied over a wide range of the ionic liquid concentrations (0.6 to 3.5 M, which corresponds to 10%-60% v/v). Interactions between GB1 and [C_4-mim]Br were observed from changes in the chemical shifts of the protein backbone as well as the changes in ^{15}N ps-ns dynamics and rotational correlation times. Site-specific interactions between the protein and [C_4-mim]Br were assigned using 3D methods under HR-MAS conditions. Thus, HR-MAS NMR is a viable tool that could aid in elucidation of the molecular mechanism of ionic liquid – protein interactions.

Keywords: imidazolium ionic liquid; GB1; ionic liquid – protein interaction; HR-MAS NMR

Introduction

Ionic liquids are customizable materials that are composed entirely of ions and have phase transitions at or below room temperature. Ionic liquids provide a unique chemical environment and have drawn considerable attention in recent years, with numerous applications as media for chemical and biocatalytic transformations [88,89], preparation of materials [90-92], energy-related processes [93-95], as well as several environmental [96-98] and analytical [99,100] systems. Notably, many recent reports describe the ability of ionic liquids to modulate inter- and intramolecular interactions of small molecules [101-103].

The microenvironment surrounding a protein can greatly affect its folded state (including secondary and tertiary structure), stability, and function. Ionic liquids offer unique environments that can be tuned to alter the structural and biophysical properties of biomacromolecules. Thus, understanding the effect of ionic liquids on the native structure of biomacromolecules is a critical step in the advancement of many areas, including enzymology, biocatalysis, and bioengineering.

While it is evident that ionic liquids can alter the stability and function of proteins, the current mechanistic understanding of protein stability and enzyme activity in ionic liquid-rich environments requires clarification. For example, some ionic liquids were noted to increase the stability of proteins by serving as an anti-aggregation/unfolding media for lysozyme over an extended period of time [104]. However, it was also shown that certain proteins, for example the redox active form of cytochrome *c*, could be denatured by imidazolium-based ionic liquids [105,106], yet choline-based ionic liquids were recently shown to improve the redox activity of cytochrome *c* [107]. While stability and enzymatic

activity of a few proteins in ionic liquid-containing aqueous media correlate with the Hofmeister's series [108,109] others do not [110,111]. Using simulations, it was also suggested that ionic liquids could influence xylanase activity by disturbing the dynamic motion of the protein in addition to affecting protein structure [112].

Protein function is intimately linked to structure and dynamics, thus a molecular-based understanding of ionic liquid-protein interactions is vital for developing efficient applications. Recent studies [113,114] have demonstrated that solution NMR spectroscopy can be utilized to probe direct interactions between ionic liquids and proteins using NMR chemical shift perturbations, which are sensitive reporters of changes in the chemical environment, including protein structural changes. Kaar and coworkers [114] demonstrated interactions between [C_4-mim]Cl and lipase A at up to 0.29 M (*i.e.*, 5% v/v) ionic liquid, and Cabrita and coworkers [113] probed the interaction of various ionic liquids (up to 1 M concentration) with the protein Im. The results from these groups established that chemical shift perturbations in the 2D ^{1}H-^{15}N HSQC spectra could be used to monitor ionic liquid-induced structural changes in the proteins. It was suggested that both electrostatic as well as hydrophobic interactions occurred between proteins and ionic liquids, as a number of charged and nonpolar residues experienced chemical shift perturbations.

Although traditional solution state NMR techniques are applicable for relatively low (≤ 1 M) concentrations of ionic liquids [113,114], the viscosity of the aqueous ionic liquid solutions above concentrations of 1 M are high enough to slow the tumbling of most proteins, thus sufficiently broadening NMR signals and limiting the use of solution state NMR. Importantly, several industrial and biomedical applications require high

concentrations of ionic liquids. For example, ionic liquid-based pretreatment of biomass is being explored for removing lignin and hemicellulose under milder conditions than conventional acid or steam pretreatments [115], however the concentration of ionic liquids are fairly high (above 20% v/v) [115,116]. Another significant application of ionic liquids is to extend the life and quality of protein storage and formulation in the pharmaceutical industry; in these cases even higher concentrations of ionic liquids have been suggested for maintaining long-term maximal protein stability [104,117,118]. Thus, in order to probe ionic liquid – protein interactions at high ionic liquid concentration, pertinent to industrial applications, alternative NMR approaches that are not limited by slow tumbling are required.

High-resolution magic-angle-spinning (HR-MAS) NMR is particularly applicable for analyzing viscous or semi-solid samples using solution NMR methods while spinning at the magic angle in order to remove line-broadening effects. HR-MAS NMR has been shown to be a useful tool in monitoring chemical reactions [119] and in establishing the structure of small (*e.g.*, ≤ 5 amino acids) peptides [120,121] in ionic liquids. HR-MAS reduces the line broadening caused by differences in magnetic susceptibly of the sample and also decreases the dipolar interaction and chemical shift anisotropy, although these effects are less significant in heterogeneous quasi-liquid samples [122].

Here, we demonstrate, for the first time, that a protein with >50 residues could be efficiently studied at atomic scale resolution in solution with high concentrations of ionic liquids using HR-MAS NMR. Specifically, structural and dynamical changes of the model 56-residue protein, immunoglobulin binding domain B1 of streptococcal protein G (GB1) [123] induced by a high concentration of [C_4-mim]Br (up to 3.5 M, which corresponds to 60

%, v/v) were monitored by using 2D ^{1}H-^{15}N HSQC, 3D HNCA, and ^{15}N relaxation spectra of GB1. Significantly, the use of HR-MAS NMR spectroscopy surmounted the problem of line broadening due to the high viscosity of the ionic liquid-containing systems, and thus this technique could provide unique and precise information about site-specific ionic liquid – protein interactions. Arguably, this work provides an important foundation for probing protein secondary structure in ionic liquid-rich media.

Experimental

[C_4-mim]Br [124,125] and GB1 [126] were prepared as previously described. NMR samples were prepared by mixing a 4.4 mM GB1 stock solution in buffer (50 mM sodium phosphate, pH 5.50), D_2O, and neat [C_4-mim]Br in a pre-determined ratio to a 1.3 mM or 0.9 mM concentration of GB1 and a 10-50% v/v or 60% v/v final concentration of [C_4-mim]Br, respectively. Other samples included GB1 in 50% v/v glycerol/aqueous solution and 1.3 mM GB1 in the presence of 2.3 M KBr. A control GB1 sample was prepared without the addition of [C_4-mim]Br, KBr, or glycerol (referred to in the text as 0% v/v [C_4-mim]Br sample). HR-MAS NMR spectra were acquired on a 600 MHz Avance III Bruker NMR spectrometer equipped with a 4 mm HR-MAS probe at 27 °C and 5 kHz MAS frequency. Additional details are given in the SI.

Results and discussion

Selection of protein, ionic liquid, and experimental method

We probed the effects of [C_4-mim]Br on the protein GB1 to gain a better understanding of how ionic liquids impact protein structure, stability, and dynamics. The GB1 structure, folding pathway, and dynamics have been previously well characterized by NMR spectroscopy [84,127-130], which makes it an ideal model protein for assessment by HR-MAS spectroscopy. GB1 is a 56-residue stable protein comprised of one α-helix packed against a four-stranded β-sheet. 1-butyl-3-methylimidazolium bromide, [C_4-mim]Br, was chosen as a model ionic liquid, as it is a common, readily available, water-soluble, and widely used ionic liquid.

GB1 samples were prepared with varying concentrations of [C_4-mim]Br in NMR buffer: 0%, 10% (0.59 M), 25% (1.47 M), 40% (2.36 M), 50% (2.95 M), and 60% v/v (3.53 M) [C_4-mim]Br. To test the effects of high viscosity and high salt concentration media, control samples were also prepared in NMR buffer: GB1 in the presence of 50% glycerol and in the presence of 2.29 M KBr. A table describing the composition of each sample is given in Table S1. The HR-MAS NMR probe was configured for MAS and with a Z-axis gradient aligned along the magic angle to provide access to a wide range of solution NMR experiments. Significantly, using an HR-MAS probe allowed us to use deuterium lock and solvent suppression of the water signal using standard solution NMR pulse sequences. Although MAS induces large pressure especially on the sample near the inner wall of the rotor, the low spinning frequency of 5 kHz in a 4 mm rotor is not expected to destabilize GB1. A concentrated aqueous solution of GB1 was mixed with neat [C_4-mim]Br and D_2O, thus the ionic liquid concentration was limited by the minimum volumes of D_2O and protein

solution. We acquired 1D ^{1}H, 1D ^{13}C, 2D ^{1}H-^{15}N HSQC, 3D HNCA, and ^{15}N relaxation spectra for GB1 utilizing HR-MAS NMR. Although the VT inlet temperature was 27 °C under HR-MAS conditions, we estimated that the actual sample temperature was approximately 30-31 °C (due mostly to frictional heating) based on comparison of GB1 2D ^{1}H-^{15}N HSQC spectra under HR-MAS conditions to conventional solution GB1 2D ^{1}H-^{15}N HSQC spectra at various temperatures (Fig S1).

The effect of [C$_4$-mim]Br on the structure of GB1

1D ^{1}H spectra were not practical to detect changes in protein secondary structure due to the large excess of [C$_4$-mim]Br in solution (data not shown). Since GB1 was uniformly ^{15}N-, ^{13}C-enriched and [C$_4$-mim]Br was not, 1D ^{13}C spectra (Fig. S2) were utilized to monitor large changes in protein secondary structure in spite of the significant signal overlap, as discussed below. The [C$_4$-mim]Br signals were sharp, and their intensity increased as the ionic liquid concentration increased.

2D ^{1}H-^{15}N HSQC GB1 spectra were acquired for all GB1 samples, including GB1 in the presence of 0-60% v/v [C$_4$-mim]Br, 2.3 M KBr, and 50% v/v glycerol) (Fig. 1 and Fig. S3). All 2D ^{1}H-^{15}N HSQC spectra were assigned based on published chemical shifts [127] and 3D HNCA spectra. 3D HNCA GB1 spectra were acquired for 0%, 10%, 25%, and 50% v/v [C$_4$-mim]Br and 2.29 M KBr samples. Fig. S4 shows the assigned ^{1}H-^{15}N HSQC spectra for GB1 in 0% [C$_4$-mim]Br, and Fig. S5 highlights examples of the HNCA strip plots used for assignments of the aqueous GB1 sample under HR-MAS conditions. The HNCA spectra were very well resolved even in the presence of 50% v/v [C$_4$-mim]Br, although the *i*-1 peak was often weak (Fig. S5c). 3D solution NMR methods under HR-

MAS conditions could be a general tool for structural studies of biomacromolecules in viscous, high salt solutions.

Traditional solution NMR 2D ^{1}H-^{15}N HSQC spectra of GB1 in the presence of 50% v/v [C_4-mim]Br were acquired at both 600 and 900 MHz using cryogenically cooled probes (Fig S6). The quality of spectra from samples in solutions containing high concentrations of ionic liquids collected at high field with cryogen probes are often compromised by poor tuning and radiation damping thereby hindering traditional solution-based NMR experiments, especially when using cryogenically cooled probes (*i.e.,* cryo/cold probes), [131] which are commonly used in protein NMR studies. In the case of GB1 in 50% v/v [C_4-mim]Br, the traditional solution NMR spectra were observed to have broader lines and T1 noise artifacts due to radiation damping (Fig S6 b,c). For example, G9 exhibited 23.0 Hz vs 33.9 Hz ^{1}H line width and L12 had a 32.86 Hz vs. 44.48 Hz ^{1}H line widths in the HR-MAS vs. traditional solution NMR spectrum at 600 MHz. Further, radiation damping from 50% v/v [C_4-mim]Br results in significant noise at ca. 7.8 ppm and 9.1 ppm (Fig S6 b,c), completely obscuring several GB1 peaks. Overall, the HR-MAS spectrum has a much better quality than the solution NMR spectrum.

High salt concentrations can induce perturbations in the protein amide ^{1}H and ^{15}N shifts due to a number of effects, including the bulk magnetic susceptibility of the solvent as well as interactions between the solvent and solute molecules [132]. Amide ^{1}H shifts in proteins are especially sensitive to hydrogen bonding [133] and can report on protein secondary structure changes. Therefore, we evaluated the chemical shift changes of the amide moieties in the backbone as a function of [C_4-mim]Br concentration using 2D ^{1}H-^{15}N HSQC. [C_4-mim]Br induced chemical shift changes in both the ^{1}H and ^{15}N dimensions

(Fig. 44, Fig. 45, Fig. S3, and Fig. S7a,b). At 50% v/v [C_4-mim]Br, all GB1 residues showed a significant (0.10-0.54 ppm) downfield ^{1}H chemical shift perturbation. The ^{15}N chemical shift perturbations were more complex and not straightforward, ranging from –2.28 to 1.97 ppm at 50% v/v [C_4-mim]Br. The combined and weighted ^{1}H and ^{15}N chemical shift perturbations [133] (ΔHN) were calculated (Fig. 45a) using equation Eq. S1. The large shift perturbations at high ionic concentrations indicated that the amino acid residue interactions with [C_4-mim]Br were significant along the protein backbone. The residues most affected (more than 0.40 ppm in ΔHN) by [C_4-mim]Br included L7, T17, V21, V29, Q32, N35, and E42 (Fig. 45b). In general, most amino acids with large chemical shift perturbations were nonpolar and charged polar residues. The anion, Br^-, is classified as a mild chaotrope (destabilizer) based on the Hofmeister's series. Bordusa and coworkers observed that neutral and chaotropic inorganic salts could cause significant chemical shift changes due to peptide-anion hydrogen bonding [121]. Thus [C_4-mim]Br – protein interactions are likely driven by both hydrophobic and electrostatic forces. The largest chemical shift perturbations clustered to the α-helical region of GB1. Additional evidence came from Cα chemical shift perturbations (known to be strong reporters of the protein's secondary structure), which were also significantly affected (ΔCα ranged from -0.21 to 1.05 ppm; Fig. S7c) by the increasing concentration of [C_4-mim]Br. Secondary structure predictions from 0, 25, and 50% IL were calculated using Talos+ (Table S4). An increase in loop content was found for residues K13, G14, and E15 and decrease in confidence of secondary structure assignment for residues in E42 and W43. K13, G14 and E15 are located near a turn previously identified as a melting hotspot in a destabilized mutant of GB1 [84].

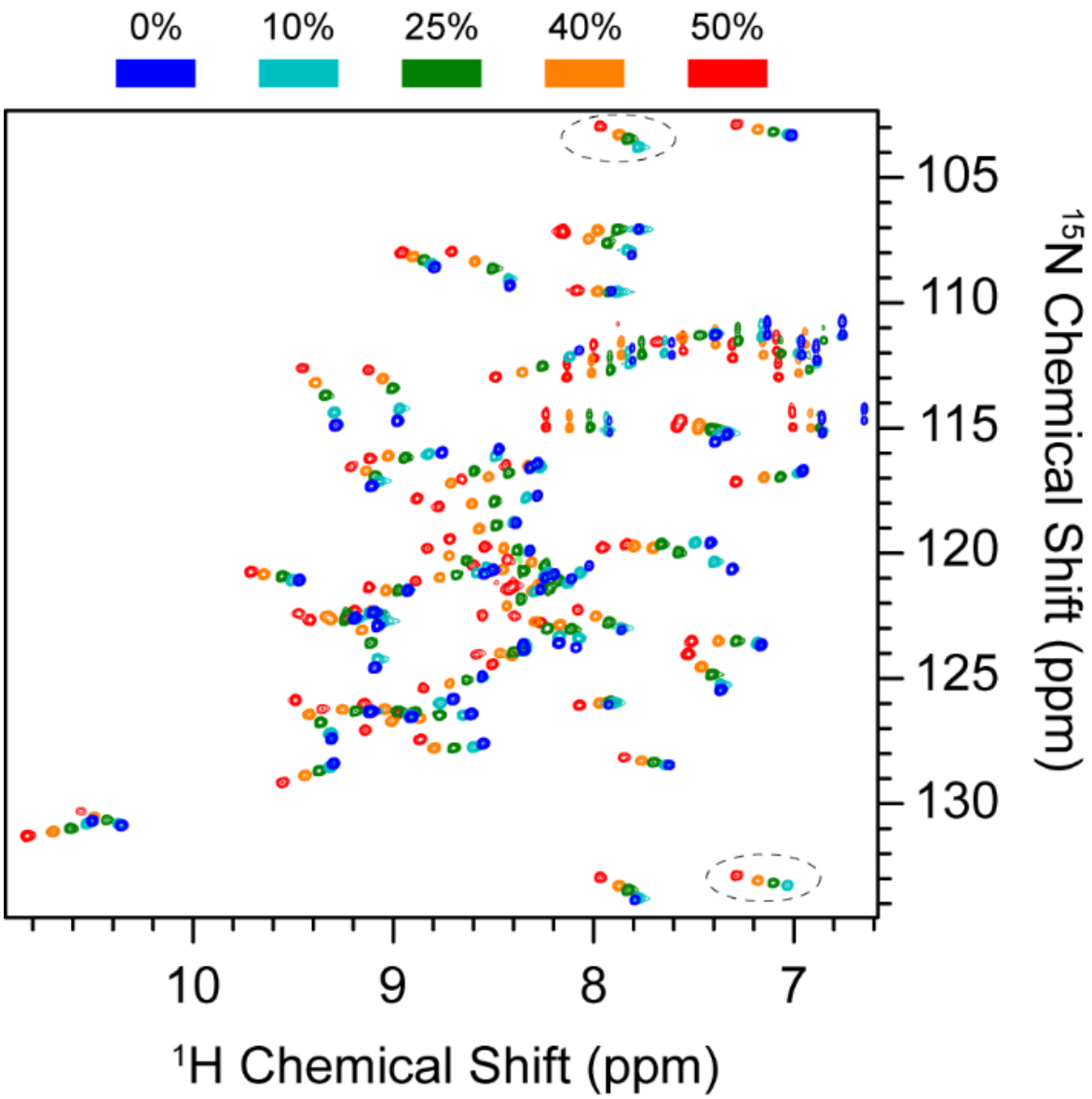

Figure 44: 2D ^{1}H-^{15}N HSQC spectra of GB1 in the presence of [C_4-mim]Br. a) Overlay of spectra with 0% (blue), 10% (cyan), 25% (green), 40% (orange), and 50% (red) v/v [C_4-mim]Br. Aliased peaks are shown in dashed ovals.

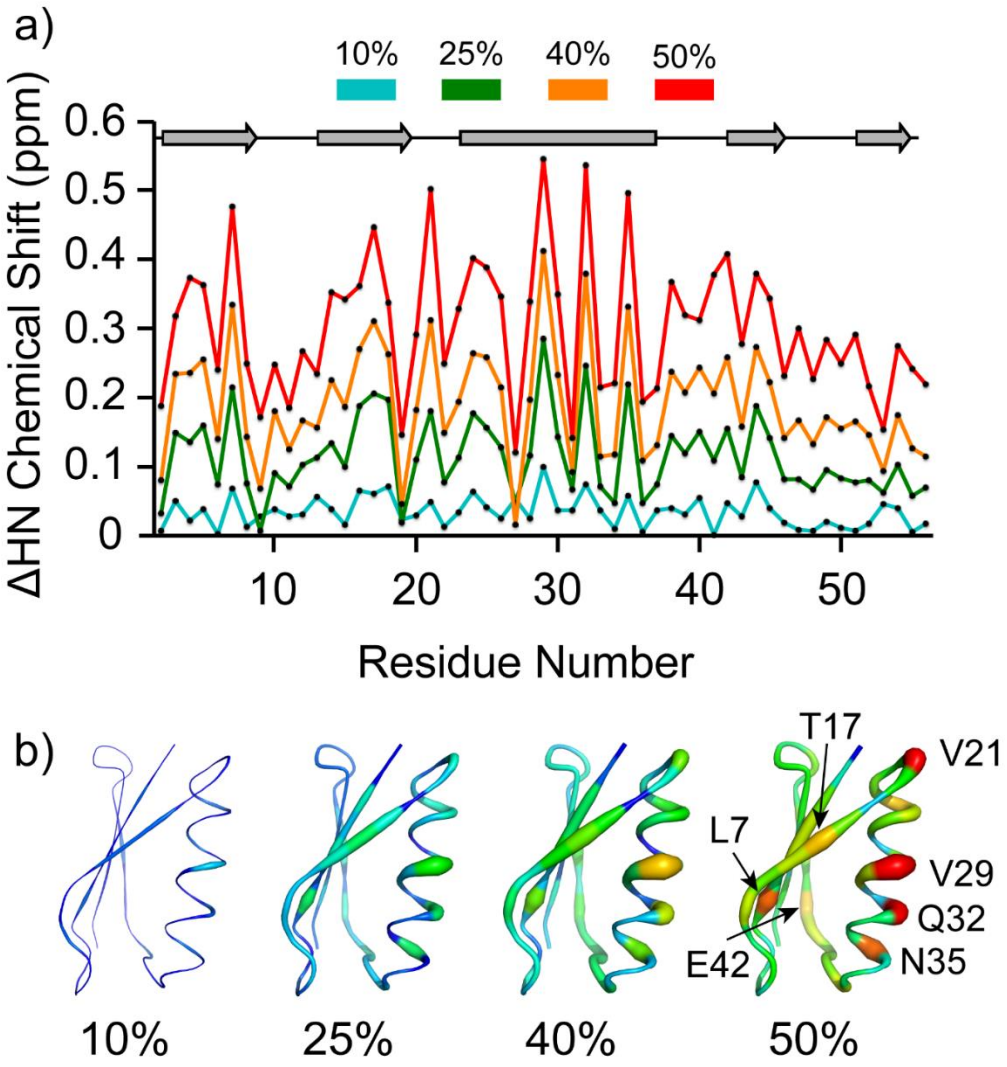

Figure 45: Chemical shift perturbations for each residue in the presence of 10-50% v/v [C_4-mim]Br. a) Combined and weighted ^{1}H and ^{15}N (ΔHN) chemical shift perturbations (CSP) of all residues in the presence of 10% (cyan), 25% (green), 40% (orange), 50% (red) v/v [C_4-mim]Br. b) Cartoon representation of the crystal structure of GB1 (PDB: 2QMT) color coded by amide chemical shifts perturbation (CSP) in 10%-50% v/v [C_4-mim]Br. Chemical shift perturbation is indicated by colors ranging from blue (least, 0.00 ppm) to red (most, 0.55 ppm), and the coloring gradient is scaled to the maximum CSP in the 50% [C_4-mim]Br sample. GB1 residues which have more 0.40 ppm CSP in the 50% v/v [C_4-mim]Br sample are identified. The maximum radius of the putty representation is scaled to maximum CSP in the shown condition (10% v/v [C_4-mim]Br, 25% v/v [C_4-mim]Br, 40% v/v [C_4-mim]Br or 50% v/v [C_4-mim]Br). The figure was generated by PYMOL.

At 60% v/v [C_4-mim]Br, GB1 exhibited multiple peaks in the ^{1}H-^{15}N HSQC for a number of residues and an increased number of peaks appeared in a narrow amide proton chemical shift at around 8.4-8.9 ppm (Fig. S3), which indicated the loss of homogeneous tertiary and secondary protein structure at 60% v/v [C_4-mim]Br. While some peaks shifted more downfield as anticipated based on our previously observed trends at lower concentrations (Fig. S3c), other additional peaks appear (Fig. S3d,e), implying the coexistence of a folded state and unfolded state of GB1.

Previous studies have shown that the thermal unfolding of GB1 is reversible throughout the transition between the folded and unfolded state [134,135]. To test whether the ionic liquid-induced unfolding was reversible, GB1 sample in 60% v/v [C_4-mim]Br was diluted with the buffer to obtain 40% v/v [C_4-mim]Br. Remarkably, the ^{1}H, ^{15}N spectrum of the resulting sample overlaid almost perfectly with the 40% v/v [C_4-mim]Br spectrum (Fig. S9b). In the ^{13}C 1D spectra, most individual amino acids were not well-resolved, however in the 60% v/v [C_4-mim]Br spectrum obvious changes were observed in the GB1 carbonyl region (Fig. S9a), which is a known sensitive reporter of protein secondary structure [136]. After the 60% v/v [C_4-mim]Br protein sample was diluted to 40% v/v [C_4-mim]Br, the carbonyl region displayed the characteristic profile of a 40% v/v [C_4-mim]Br-GB1 sample, consistent also with the observations in the ^{1}H, ^{15}N spectra. Overall, the data indicated that the unfolding of GB1 due to its interaction with [C_4-mim]Br was reversible, and the protein could re-gain its well defined native structure upon decreasing the ionic liquid content.

Molecular tumbling and backbone ^{15}N relaxation of GB1 in [C$_4$-mim]Br

Ionic liquids are much more viscous than most conventional solvents, and solution NMR measurements can be hindered by high viscosity. Although neat [C$_4$-mim]Br exhibited very high viscosity (*i.e.* 433 cP at 27 °C), the presence of water reduced the viscosity substantially (Table S5 and S10a). For instance, the viscosity of 60% v/ v [C$_4$-mim]Br solution at 27 °C was 6.0 cP. For comparison, the viscosity of a 50% v/v glycerol in the NMR buffer was 8.4 cP, slightly higher than the viscosity of the 60% v/v [C$_4$-mim]Br mixture. The 2D ^{1}H-^{15}N HSQC spectrum of GB1 in 50% v/v glycerol appeared to be shifted upfield, while still being of similar resolution and quality as the GB1 spectrum without additives (Fig. S10b), thus the viscosity of the solution medium was not a major factor in protein destabilization.

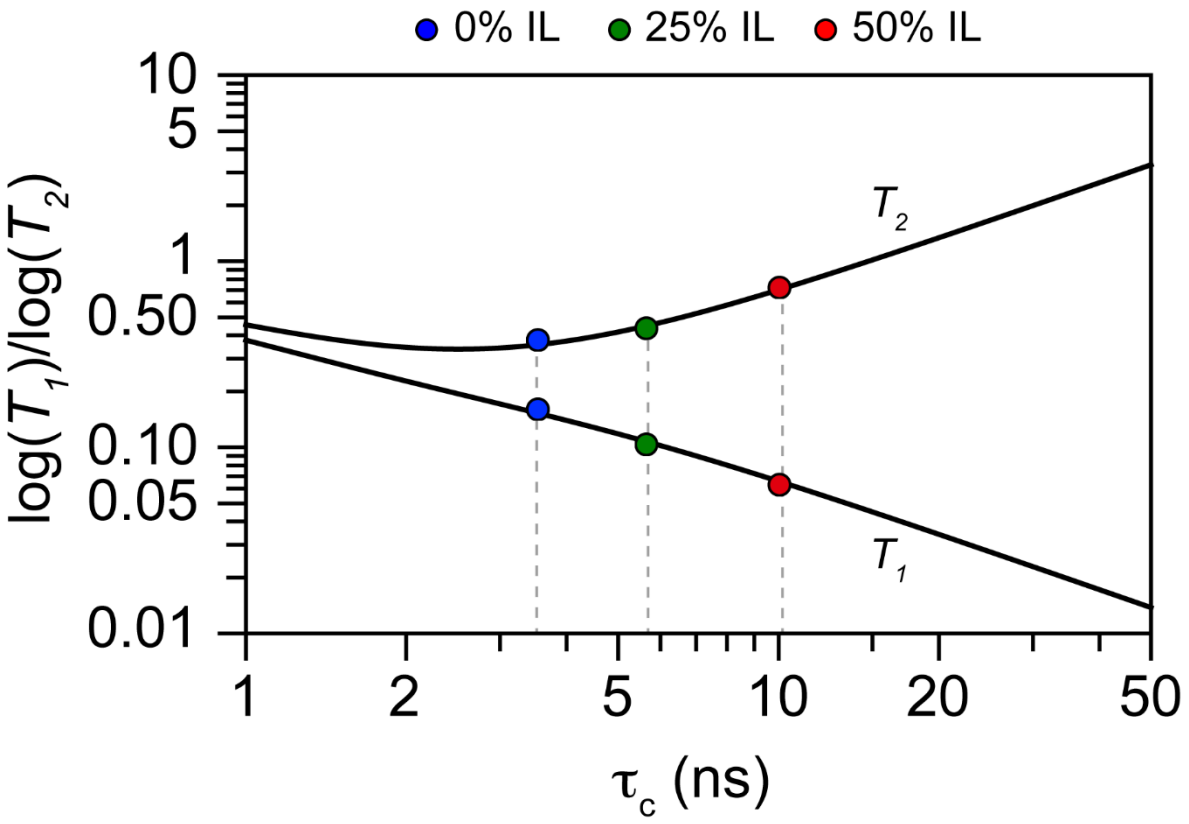

Figure 46: Rotational correlation times (τ_c) for GB1 in 10%, 25% and 50% v/v [C_4-mim]Br. Rotational correlation times were calculated from an average of T_1 and T_2 times of non-flexible residues for GB1 in the presence of 0% (blue), 25% (green), and 50% (red) v/v [C_4-mim]Br. The theoretical T_1 and T_2 curves were calculated using a home written Mathematica script.

Backbone ^{15}N spin relaxation T_1 and T_2 (from which R_1 and R_2 are calculated) were measured in order to determine the tumbling rates τ_c, for GB1 in 0%, 25%, and 50% aqueous [C_4-mim]Br. The residue specific R_1, R_2 and hetNOE relaxation data for 0% [C_4-mim]Br (Fig. S7d, S7e, S7f) supported previously published data of GB1 in solution state experiments [128], demonstrating that the HR-MAS technique did not introduce any observed, unintended effects. The average T_1 and T_2 values of the different solutions at the calculated τ_c values (Tab. 3) of 3.53 ns, 5.64 ns, and 10.37 ns for 0%, 25%, and 50% v/v [C_4-mim]Br were in good agreement with theoretical values (Fig. 46). In addition, they

were in a relatively good agreement with values calculated using Stoke's law (Eq. S2 and S3.), especially at lower viscosities. Although GB1 is a small model protein which tumbles reasonably well even in high viscosity solvents, our results show that the HR-MAS technique can be utilized as an alternative technique to traditional solution NMR to study proteins in high concentrations of ionic liquids, which will be particularly advantageous when applied to large proteins.

The residue specific R_1 and R_2 are sensitive reporters of the ps-ns timescale motions and can be used to measure the backbone motions of a protein. At 25% and 50% v/v [C_4-mim]Br, GB1 showed a relative decrease in R_1 and increase in R_2 rates for residues 20-30, which were found in the N-terminal half of the α-helix, and consistent with previous findings that suggest that the N-terminal part of the helix was part of an unfolding hotspot [84]. These ^{15}N relaxation results support the chemical shift data, which suggests that higher concentrations of [C_4-mim]Br destabilize and promote local unfolding of GB1.

Sample	Ave. T_1/ms	Ave. T_2/ms	T_c, relax /ns	T_c, SL /ns
0% IL	160.6	377.1	3.53	3.46
25% IL	103.7	436.2	5.64	5.88
50% IL	62.9	721.1	10.37	13.27

Table 3: ^{15}N spin relaxation T_1 and T_2 and tumbling rate, τ_c of GB1-[C_4-mim]Br samples. The τ_c values were calculated from the ^{15}N NMR data (relax) or based on Stoke's Law (SL), as described in detail in the Supplemental Information.

In conclusion, we have demonstrated that HR-MAS NMR spectroscopy is a viable tool to study atomic level protein – ionic liquid interactions in a high ionic liquid concentration (3.53 M), high inorganic salt concentration (2.29 M), and high viscosity (7.4 cP). Specifically, the chemical shift perturbation analysis of ΔHN and ΔCα suggested that the α-helical region of GB1 had the strongest interaction with [C_4-mim]Br. Interestingly, even though regions of the protein with the highest CSP did not appear to change their secondary structure dramatically even in 50% IL, where it is clear that in 60% v/v [C_4-mim]Br, GB1 folded and unfolded states coexisted. However, GB1 unfolding was reversible upon dilution to 40% [C_4-mim]Br. Residue specific R_1, R_2 and hetNOE relaxation data obtained for GB1 in the presence of 0%, 25%, and 50% v/v [C_4-mim]Br show that the protein not only experiences decreased tumbling rates due to viscosity, but also shows changes in the ps-ns timeframe consistent with destabilization of a previously reported unfolding hotspot. The GB1 tumbling rates in [C_4-mim]Br solutions were in good agreement with theoretical values, thus supporting the use of HR-MAS as a tool for studying proteins or large molecules in highly viscous and high ionic strength media. Importantly, the results of this study open up many exciting possibilities for further structural and dynamical characterization of others, in high concentration of ionic liquids, which will advance the fundamental understanding of how ionic liquids influence native protein secondary structure and function, a critical step in the development of many applications.

Acknowledgements

This work was supported by the National Science Foundation (awards CHE-1413696, CBET-1403947, and DGE-0948027), by the U.S. Department of Energy under Contract No. DE-AC36-08-GO28308 with the National Renewable Energy Laboratory, and by the University of Wyoming. The BioEnergy Science Center is a U.S. Department of Energy Bioenergy Research Center supported by the Office of Biological and Environmental Research in the DOE Office of Science. LW was partially supported by Institutional Development Awards (IDeA) from the National Institute of General Medical Sciences of the National Institutes of Health under Grants P20GM103432, P20GM103408 and P20GM109095. We thank Chad M. Rienstra at the University of Illinois at Urbana-Champaign for generously providing the GB1 sample. Reprint of this article was done with permission from Elsevier[137].

CHAPTER 6

CONCLUSIONS AND SUMMARY

Project I: Characterization of the antifreeze protein ApAFP752

As previously stated, antifreeze proteins are of great interest in the area of cryopreservation. We have worked to characterize the insect antifreeze protein, ApAFP752. In doing so, we have been able to gain greater insight into the functionality and potential applications of this protein. We have focused on 2 primary aims, and have been able to answer several of the questions associated with these aims.

Aim 1: Structural characterization of ApAFP752 antifreeze protein by solution NMR spectroscopy. We hypothesized that the structure of ApAFP752 would show good surface complementary to ice. The expression and purification of the TrxA-ApAFP752 fusion protein was reported in the literature before, however, we have developed a method for the production of active ApAFP752 (without the fusion partner) for NMR studies and characterized its thermal hysteresis activity. Our results show that the antifreeze protein ApAFP752 has a β-helical secondary structure, similar to other known insect antifreeze proteins, which plays a role in the protein's ice-binding properties. To this end, preliminary structural data indicates the spacing between the interhelical and intra-strand threonines is similar to the spacing of waters in ice along the a-axis and c-axis, respectively. Furthermore, temperature studies of ApAFP752 show the protein does not experience any significant change in secondary structure at lower temperatures, however, it does experience temperature related changes in hydrogen bonding distances.

Additional refinement of the protein structure is underway using distance constraint NOESY spectra. Protein dynamics analysis is also underway and will yield greater insight into protein structural properties.

Aim 2: Investigate the cryoprotective mechanism ApAFP752 in live cells. Our hypothesis was that ApAFP752 can confer cryoprotection to live cells that are otherwise sensitive to freezing. Our data have shown that the TrxA-ApAFP752 (ApAFP752 joined with thioredoxin) fusion protein could confer partial cryoprotection to *Xenopus* oocytes and human skin fibroblast cells. Our results also suggest that one of the mechanisms by which ApAFP752 protects cells during freeze/thaw is by protecting the cell membranes. Additional studies are being performed to characterize the interaction between ApAFP752 and cell membranes. Application of the antifreeze protein's properties are currently being investigated in the form of protein-polymer hybrid constructs for use as anti-icing materials.

Project II. Ionic liquid interactions with proteins

Ionic liquid-protein interactions have been of interest to the scientific community since it was first hypothesized that ionic liquids can be tuned to alter the structural and biophysical properties of proteins. We have worked to characterized the interaction of the ionic liquid, [C4-mim]Br, with a model protein, GB1. Throughout this work we have focused on 2 aims and have obtained useful insight on some of the potential effects ionic liquids have on protein structure.

Aim 1: Utilize high resolution magic angle spinning (HR-MAS) NMR spectroscopy to characterize a protein site specifically in highly viscous

environment. We hypothesized that HR-MAS NMR spectroscopy was a viable tool to study proteins at the atomic level in a highly viscous environment. We have demonstrated that HR-MAS can indeed be applied for studying proteins in highly viscous (as well as high ionic strength media in our example) and could report on protein structure and dynamics site specifically using complex, traditional solution NMR sequences. Site-specific interactions between the protein and [C_4-mim]Br were assigned using 3D methods under HR-MAS conditions.

Aim 2: Investigate whether ionic liquids have the ability to stabilize protein fold. We hypothesized that the ionic liquid [C4-mim]Br could stabilize the structure of the GB1 protein. Our data showed that high concentrations (60% v/v) of [C4-mim]Br had a destabilizing effect on GB1, and folded and unfolded states of GB1 co-existed. We have identified protein unfolding hotspots and reported on protein dynamics. This work provides an important foundation for probing protein secondary structure in ionic liquid-rich media.

APPENDIX

Materials and Methods

Plasmid Constructs: The plasmid construct for the fusion protein TrxA-ApAFP752 was obtained as a gift from Dr. Ji Ma at XinJiang University, Urumqi, China. The fusion protein is engineered in the a pET32a construct and contains a cleavage site for enterokinase engineered between the TrxA and the ApAFP752 with a 6-His histidine tag located on the C-terminus of the TrxA portion of the fusion protein.

An ApAFP752 construct was designed as a non-fusion form of the protein (no TrxA attachment) using a pET23a plasmid vector. A Tobacco Echovirus (TEV) protease cut site and 6-His histidine tag were engineered on to the protein sequence with 6-His histidine tag on the C-terminus and the TEV protease cut site between the protein sequence and the 6-His histidine tag.

Materials Used in the Expression of Trx-ApAFP752: Chemicals were purchased from VWR, Fisher Scientific and Sigma Aldrich. Isopropyl β-D-thiogalactopyranoside (IPTG) and ampicillin were purchased from Gold Biotechnology. EDTA free Halt protease inhibitor was purchased from Fisher Scientific. ^{15}N labeled ammonium hydroxide was purchased from both Sigma Aldrich and Cambridge Isotope Laboratories. Benzonase nuclease (DNase) was purchased from Novagen. HIS-Select® nickel affinity resin was purchased from Sigma Aldrich. HisTrap FF nickel affinity columns were purchased from GE Healthcare Life Sciences. Gel electrophoresis materials were purchased from BioRad.

Method of Expression of Trx-ApAFP752: The following is a general discussion of the techniques employed in the expression of both the fusion protein Trx-ApAFP752 and the protein ApAFP752. As the initial studies were performed on the protein produced from Plasmid 1, this section will reference it in all cases where the techniques used are universal to the three AFP plasmids previously mentioned.

The plasmid of interest was propagated using DH5α competent *Escherichia coli* (*E. coli*)[138]. The plasmid was then transformed into BL21 (DE3) pLysS competent *E. coli*[139-141]. A transformation was performed by incubating a mixture of the plasmid and *E. coli* cell line at 4 °C for 40 minutes. Heat shock was then induced by incubating the mixture at 42 °C for 35 seconds. Following heat shock, the mixture was immediately submerged in ice. SOC media was combined with the plasmid/bacteria mixture and incubated at 37 °C for 1 hour. The resulting culture was plated on luria agar plates with a final ampicillin concentration of 0.3 mM. The plates were incubated overnight at 37 °C.

Following incubation, the plates were removed from the incubator. Single colonies were pulled from the plates and placed in luria broth containing a final ampicillin concentration of 0.3 mM. These pre-cultures were then placed in a coffin shaker and incubated at 37 °C for 12 hours. A small aliquot of the pre-culture was then used to inoculate 1 L of luria broth containing 0.3 mM ampicillin. This mixture was then shaken at 225 rpm and 37 °C until an optical density (OD_{600}) of 0.7 absorbance units at 600 nm was achieved. Cells were harvested via centrifugation at 9559 x g, 4 °C for 20 minutes and the supernatant discarded.

Natural Abundance Protein: Cell pellets were resuspended in 250 mL minimal growth medium. The resulting suspension was then incubated for 1 hour at 15 °C and 225 rpm. Over-expression of the protein was induced by adding 250 µL of a 400 mM stock solution of IPTG to the culture (final concentration 0.4 mM IPTG). The culture was incubated at 15 °C, 225 rpm for 12 hours. The OD_{600} was monitored over the course of the induction phase in order to ensure that the cells remained viable. Upon completion, the cells were harvested via centrifugation. Cells were harvested via centrifugation at 9559 x g, 4 °C for 25 minutes. The remaining supernatant medium was discarded, and the pellet was stored at -80 °C until lysis and purification could be performed.

Stable Isotope Labeling of Protein: Upon reaching an OD_{600} of 0.7 absorbance units, the cells were harvested by centrifugation. The supernatant was discarded, and the remaining pellet was resuspended with 250 mL of isotopically enriched minimal media. The resulting suspension was then incubated for 1 hour at 15 °C and 225 rpm. Following the 1 hour incubation the culture was inoculated with 250 µL 400 mM IPTG to induce protein over-expression and incubated at 15 °C and 225 rpm for 12 hours. The OD_{600} was monitored continuously over the course of the growth in order to ensure cell viability. Upon completion, the cells were harvested by centrifugation. The supernatant was discarded, and the pellets stored at -80 °C until purification could be performed.

Purification: Pellets were removed from the -80 °C freezer, weighed and thawed at 4 °C. Once thawed, the pellets were then resuspended with an EDTA free protease inhibitor solution containing 50 mM sodium phosphate, 150 mM NaCl, pH 8.0 and Benzonase

nuclease. Once the pellets were resuspended, the cells were lysed using a French press at 1500 psi performed in quadruplicate. The lysate was collected and centrifuged 20,217 x g, 4 °C for 30. The protein containing supernatant was collected for further purification. The protein sample was then passed through a 0.22 µm syringe driver filter and then concentrated to 5 mL.

After concentration, the sample was purified using nickel affinity chromatography via a GE Healthcare ÄKTA 900 Fast Protein Liquid Chromatographer (FPLC). The sample was eluted using a 50 mM sodium phosphate, 150 mM NaCl, pH 8.0 buffer containing 500 mM imidazole. Upon completion of the initial, crude His-tag purification the sample's purity was analyzed using Sodium dodecylsulfate polyacrylamide gel electrophoresis (SDS-PAGE). The sample was then dialyzed for a minimum of 14 hours using a 50 mM sodium phosphate, 150 mM NaCl, pH 8.0 buffer. The sample was switched into new buffer at hours 0 and 2 to ensure maximum removal of imidazole from the sample.

Purity was assessed using polyacrylamide gels and additional purification steps were sometimes required. If further purification was required, additional rounds of FPLC were employed in the form of Ni-affinity chromatography, size exclusion chromatography or anion exchange chromatography. Upon completion of each FPLC run, dialysis or buffer exchange of the protein was performed. Analysis of the purity of the protein was performed via SDS-PAGE and protein bands were visualized by Coomassie brilliant blue. Once the sample purity had reached an acceptable level it was ready for experimentation and testing.

Protein sample concentration was estimated using UV-Visible spectrophotometry, monitoring the sample at 280 nm and 275 nm for TrxA-ApAFP752 and ApAFP752,

respectively. Extinction coefficients for each protein were calculated using ExPASy ProtParam tool[48] and were used to calculate the concentration of the sample via UV-Visible spectrophotometry.

Cleavage of TrxA-ApAFP752: ApAFP752 was removed from the fusion protein via proteolytic cleavage using bovine His-enterokinase (Prospec-Tany). TrxA-ApAFP752 cleavage was performed in 50 mM potassium phosphate, 20 mM NaCl, pH 8.0. A small-scale cleavage test was performed with an enzyme to protein mixture ratio of 1 IU bovine His-enterokinase to 400 µg TrxA-ApAFP752 for six hours at 25 °C. Samples were taken every two hours. SDS-PAGE was performed and stained with Coomasie brilliant blue. Full cleavage was performed using 1 IU bovine His-enterokinas per 400 µg TrxA-ApAFP752 for six hours at 25 °C. The cleavage sample was then passed FPLC Ni-affinity and the flow through was collected.

Cryoprotection Studies: Cryoprotection studies were performed in collaboration with Dr. Daniel Levy's group at the University of Wyoming, Department of Molecular Biology. A natural abundance sample of Trx-ApAFP752 was prepared in a buffer of 20 mM Tris HCl, 20 mM NaCl at pH 7.5 by the Varga lab. The final concentration of the produced protein sample was 113 µM. Cryoprotection studies were performed by the Levy lab on unfertilized eggs from the frog *X. laevis*[142].

Nuclear Magnetic Resonance Studies on AFP:

Purified samples were concentrated to a minimum final concentration 100 μM in order to produce enough usable signal for spectrum analysis. Samples were prepared for NMR by adding 5 % deuterium oxide (D_2O) for sample locking, 4,4-dimethyl-4-silapentane-1-sulfonic acid (0.2 mM final concentration) for referencing and sodium azide (final concentration 1 mM) as a biocide. Samples were packed into 3 mm or 5 mm (depending on sample volume) D_2O matched Shigemi® NMR tubes. Sample spectra were collected using a Bruker Avance III 600 MHz NMR spectrometer with a 5 mm BBO solution probe (University of Wyoming), a Bruker Avance III 800 MHz NMR spectrometer with a 5 mm TCI cryoprobe probe (City University of New York Advanced Science Research Center) and a Bruker Avance II 800 MHz NMR spectrometer with a 5 mm TCI cryoprobe probe (Brandeis University).

Differential Scanning Calorimetry:

Samples were tested in a buffer consisting of 50 mM potassium phosphate, 20 mM NaCl. An aliquot of 10 μL of each sample was loaded into Tzero® aluminum hermetic pans (TA Instruments) cooled to -30.0 °C at a rate of 1 °C min^{-1} and held at this temperature for 10 minutes. Samples were then heated at 1 °C min^{-1} up to -1.0 °C, held at this temperature for 5 minutes and cooled to -30.0 °C at 1 °C min^{-1}. This freeze-thaw cycle was repeated from -1.0 °C to +0.5 °C in increments of 0.1 °C in order to vary the percentage of ice present in the sample[43,52]. Thermal hysteresis activity data was collected on a TA Instruments Q2000 Differential Scanning Calorimeter. The percentage of ice was estimated to be $\left|[1-\left(-{}^{\Delta H_r}/_{\Delta H_m}\right)]\right| \times 100\%$, where ΔH_m is the enthalpy of melting and

ΔH_r is the enthalpy of refreezing. The enthalpies of melting and refreezing were calculated using the Universal Analysis software package from TA Instruments. The enthalpy of refreezing was calculated by integrating the area under the curve of the exotherm associated with the refreezing cycle which showed thermal hysteresis activity. The enthalpy of melting was calculated by integrating the area under the curve of the endotherm associated with the melting cycle at a temperature of +0.5 °C, where complete melting of the sample was observed.

Table A1: Chemical Shift Assignment Table for ApAFP752

	Res	Res	Res	Atom		Iso	CS	STD	
1	2	2	MET	C	C	13	175.833	0.00	0
2	2	2	MET	CA	C	13	56.059	0.08	0
3	2	2	MET	CB	C	13	33.092	0.28	0
4	2	2	MET	CE	C	13	20.214	0.00	0
5	2	2	MET	CG	C	13	31.928	0.03	0
6	2	2	MET	HA	H	1	4.432	0.00	0
7	2	2	MET	HB2	H	1	2.147	0.00	0
8	2	2	MET	HB3	H	1	2.137	0.00	0
9	2	2	MET	HE	H	1	1.974	0.00	0
10	2	2	MET	HG2	H	1	2.626	0.00	0
11	2	2	MET	HG3	H	1	2.501	0.00	0
12	3	3	ALA	C	C	13	177.146	0.00	0
13	3	3	ALA	CA	C	13	52.560	0.09	0
14	3	3	ALA	CB	C	13	19.378	0.07	0
15	3	3	ALA	H	H	1	8.344	0.00	0
16	3	3	ALA	HA	H	1	4.345	0.03	0
17	3	3	ALA	HB	H	1	1.399	0.03	0
18	3	3	ALA	N	N	15	124.613	0.08	0
19	4	4	ASP	C	C	13	176.373	0.00	0
20	4	4	ASP	CA	C	13	54.431	0.11	0
21	4	4	ASP	CB	C	13	41.262	0.04	0
22	4	4	ASP	H	H	1	8.199	0.00	0
23	4	4	ASP	HA	H	1	4.616	0.02	0
24	4	4	ASP	HB2	H	1	2.718	0.01	0
25	4	4	ASP	HB3	H	1	2.621	0.00	0
26	4	4	ASP	N	N	15	119.425	0.02	0
27	5	5	ILE	C	C	13	176.846	0.00	0
28	5	5	ILE	CA	C	13	61.586	0.12	0
29	5	5	ILE	CB	C	13	38.640	0.14	0
30	5	5	ILE	CD	C	13	13.235	0.04	0
31	5	5	ILE	CG1	C	13	27.309	0.02	0
32	5	5	ILE	CG2	C	13	17.726	0.03	0
33	5	5	ILE	H	H	1	8.019	0.00	0
34	5	5	ILE	HA	H	1	4.191	0.02	0
35	5	5	ILE	HB	H	1	1.924	0.00	0
36	5	5	ILE	HB3	H	1	1.972	0.00	0
37	5	5	ILE	HD1	H	1	0.912	0.00	0
38	5	5	ILE	HG1	H	1	1.480	0.00	0
39	5	5	ILE	HG12	H	1	1.480	0.00	0
40	5	5	ILE	HG13	H	1	1.480	0.00	0
41	5	5	ILE	HG2	H	1	1.209	0.00	0
42	5	5	ILE	N	N	15	120.471	0.03	0
43	6	6	GLY	C	C	13	174.355	0.00	0
44	6	6	GLY	CA	C	13	45.577	0.07	0
45	6	6	GLY	H	H	1	8.460	0.00	0
46	6	6	GLY	HA1	H	1	4.052	0.00	0
47	6	6	GLY	HA2	H	1	4.028	0.02	0
48	6	6	GLY	HA3	H	1	4.028	0.02	0
49	6	6	GLY	N	N	15	112.268	0.03	0
50	7	7	SER	C	C	13	174.440	0.00	0
51	7	7	SER	CA	C	13	58.508	0.07	0
52	7	7	SER	CB	C	13	64.143	0.05	0
53	7	7	SER	H	H	1	8.086	0.00	0

54	7	7	SER	HA	H	1	4.501	0.00	0
55	7	7	SER	HB2	H	1	4.018	0.00	0
56	7	7	SER	HB3	H	1	3.950	0.07	0
57	7	7	SER	N	N	15	115.425	0.03	0
58	8	8	GLU	C	C	13	175.993	0.00	0
59	8	8	GLU	CA	C	13	56.668	0.12	0
60	8	8	GLU	CB	C	13	30.223	0.05	0
61	8	8	GLU	CG	C	13	36.275	0.00	0
62	8	8	GLU	H	H	1	8.435	0.01	0
63	8	8	GLU	HA	H	1	4.381	0.01	0
64	8	8	GLU	HB2	H	1	2.263	0.00	0
65	8	8	GLU	HB3	H	1	2.067	0.00	0
66	8	8	GLU	N	N	15	122.189	0.08	0
67	9	9	CYS	CA	C	13	55.937	0.00	0
68	9	9	CYS	CB	C	13	33.047	0.00	0
69	9	9	CYS	H	H	1	8.317	0.01	0
70	9	9	CYS	N	N	15	118.792	0.11	0
71	13	13	CYS	C	C	13	172.422	0.00	0
72	13	13	CYS	CA	C	13	55.806	0.11	0
73	13	13	CYS	CB	C	13	44.988	0.03	0
74	13	13	CYS	HA	H	1	4.317	0.00	0
75	13	13	CYS	HB3	H	1	2.794	0.00	0
76	14	14	THR	C	C	13	175.123	0.00	0
77	14	14	THR	CA	C	13	61.156	0.02	0
78	14	14	THR	CB	C	13	72.097	0.00	0
79	14	14	THR	CG2	C	13	19.444	0.00	0
80	14	14	THR	H	H	1	7.524	0.00	0
81	14	14	THR	HA	H	1	4.759	0.00	0
82	14	14	THR	HB	H	1	4.078	0.00	0
83	14	14	THR	N	N	15	113.911	0.10	0
84	15	15	GLY	C	C	13	174.424	0.00	0
85	15	15	GLY	CA	C	13	45.399	0.11	0
86	15	15	GLY	H	H	1	7.997	0.01	0
87	15	15	GLY	HA1	H	1	4.015	0.00	0
88	15	15	GLY	HA2	H	1	4.015	0.00	0
89	15	15	GLY	HA3	H	1	4.015	0.00	0
90	15	15	GLY	N	N	15	111.656	0.06	0
91	16	16	GLY	C	C	13	174.424	0.00	0
92	16	16	VAL	CA	C	13	61.712	0.01	0
93	16	16	VAL	H	H	1	8.017	0.01	0
94	16	16	VAL	HA	H	1	4.480	0.00	0
95	16	16	VAL	N	N	15	112.776	0.03	0
96	18	18	CYS	C	C	13	176.944	0.00	0
97	18	18	CYS	CA	C	13	55.694	0.08	0
98	18	18	CYS	CB	C	13	43.292	0.08	0
99	18	18	CYS	HA	H	1	4.503	0.00	0
100	18	18	CYS	HB2	H	1	2.967	0.00	0
101	18	18	CYS	HB3	H	1	2.223	0.00	0
102	19	19	PHE	C	C	13	175.629	0.00	0
103	19	19	PHE	CA	C	13	63.110	0.06	0
104	19	19	PHE	CB	C	13	39.515	0.05	0
105	19	19	PHE	H	H	1	8.445	0.00	0
106	19	19	PHE	HA	H	1	4.395	0.00	0
107	19	19	PHE	HB2	H	1	3.580	0.00	0
108	19	19	PHE	HB3	H	1	3.048	0.00	0
109	19	19	PHE	N	N	15	125.013	0.16	0
110	20	20	SER	C	C	13	173.766	0.00	0

111	20	20	SER	CA	C	13	58.504	0.05	0
112	20	20	SER	CB	C	13	63.810	0.02	0
113	20	20	SER	H	H	1	8.151	0.01	0
114	20	20	SER	HA	H	1	4.345	0.00	0
115	20	20	SER	HB2	H	1	4.075	0.00	0
116	20	20	SER	HB3	H	1	3.957	0.00	0
117	20	20	SER	N	N	15	108.311	0.04	0
118	21	21	CYS	CA	C	13	57.565	0.10	0
119	21	21	CYS	CB	C	13	43.835	0.00	0
120	21	21	CYS	H	H	1	7.664	0.01	0
121	21	21	CYS	N	N	15	120.203	0.05	0
122	22	22	MET	C	C	13	175.517	0.00	0
123	22	22	MET	CA	C	13	54.508	0.02	0
124	22	22	MET	CB	C	13	32.309	0.00	0
125	22	22	MET	HA	H	1	4.830	0.00	0
126	22	22	MET	HG2	H	1	2.625	0.00	0
127	22	22	MET	HG3	H	1	2.446	0.00	0
128	23	23	ALA	C	C	13	174.211	0.00	0
129	23	23	ALA	CA	C	13	51.464	0.05	0
130	23	23	ALA	CB	C	13	18.878	0.02	0
131	23	23	ALA	H	H	1	7.384	0.00	0
132	23	23	ALA	HA	H	1	4.806	0.01	0
133	23	23	ALA	HB	H	1	1.484	0.02	0
134	23	23	ALA	N	N	15	127.246	0.03	0
135	24	24	GLU	C	C	13	175.401	0.00	0
136	24	24	GLU	CA	C	13	54.914	0.06	0
137	24	24	GLU	CB	C	13	29.591	0.15	0
138	24	24	GLU	CG	C	13	35.802	0.00	0
139	24	24	GLU	H	H	1	7.674	0.01	0
140	24	24	GLU	HA	H	1	4.893	0.03	0
141	24	24	GLU	HB2	H	1	1.933	0.00	0
142	24	24	GLU	HB3	H	1	1.933	0.00	0
143	24	24	GLU	N	N	15	122.508	0.08	0
144	25	25	CYS	C	C	13	175.729	0.00	0
145	25	25	CYS	CA	C	13	56.556	0.04	0
146	25	25	CYS	CB	C	13	47.161	0.06	0
147	25	25	CYS	H	H	1	8.601	0.00	0
148	25	25	CYS	HB2	H	1	3.666	0.00	0
149	25	25	CYS	N	N	15	128.271	0.07	0
150	26	26	THR	C	C	13	173.395	0.00	0
151	26	26	THR	CA	C	13	60.027	0.08	0
152	26	26	THR	CB	C	13	70.679	0.15	0
153	26	26	THR	CG2	C	13	21.702	0.00	0
154	26	26	THR	H	H	1	8.860	0.01	0
155	26	26	THR	HA	H	1	5.193	0.00	0
156	26	26	THR	HB	H	1	3.908	0.00	0
157	26	26	THR	HG2	H	1	1.103	0.00	0
158	26	26	THR	N	N	15	120.983	0.07	0
159	27	27	ASN	C	C	13	176.052	0.00	0
160	27	27	ASN	CA	C	13	54.372	0.12	0
161	27	27	ASN	CB	C	13	38.744	0.24	0
162	27	27	ASN	H	H	1	8.026	0.01	0
163	27	27	ASN	HA	H	1	4.611	0.30	0
164	27	27	ASN	HB2	H	1	3.465	0.00	0
165	27	27	ASN	HB3	H	1	2.841	0.00	0
166	27	27	ASN	N	N	15	121.855	0.06	0
167	28	28	CYS	C	C	13	177.961	0.00	0

168	28	28	CYS	CA	C	13	56.230	1.23	0
169	28	28	CYS	CB	C	13	42.359	0.01	0
170	28	28	CYS	H	H	1	8.198	0.00	0
171	28	28	CYS	HA	H	1	4.363	0.00	0
172	28	28	CYS	HB2	H	1	1.663	0.00	0
173	28	28	CYS	HB3	H	1	0.905	0.00	0
174	28	28	CYS	N	N	15	121.252	0.18	0
175	29	29	CYS	CA	C	13	55.377	0.00	0
176	29	29	GLY	CA	C	13	45.543	0.02	0
177	29	29	GLY	H	H	1	8.418	0.01	0
178	29	29	GLY	HA3	H	1	4.064	0.00	0
179	29	29	GLY	N	N	15	109.441	0.04	0
180	32	32	ARG	C	C	13	176.051	0.00	0
181	32	32	ARG	CA	C	13	57.714	0.06	0
182	32	32	ARG	CB	C	13	39.565	0.09	0
183	32	32	ARG	HD2	H	1	3.125	0.00	0
184	33	33	ASN	C	C	13	174.185	0.00	0
185	33	33	ASN	CA	C	13	52.908	0.03	0
186	33	33	ASN	CB	C	13	41.982	0.08	0
187	33	33	ASN	H	H	1	8.762	0.01	0
188	33	33	ASN	HA	H	1	5.013	0.03	0
189	33	33	ASN	HB2	H	1	2.811	0.00	0
190	33	33	ASN	HB3	H	1	2.429	0.00	0
191	33	33	ASN	N	N	15	112.984	0.10	0
192	34	34	ALA	CA	C	13	54.007	0.04	0
193	34	34	ALA	CB	C	13	19.773	0.00	0
194	34	34	ALA	H	H	1	6.987	0.00	0
195	34	34	ALA	HA	H	1	4.439	0.00	0
196	34	34	ALA	HB	H	1	1.351	0.00	0
197	34	34	ALA	N	N	15	125.616	0.06	0
198	35	35	ARG	C	C	13	177.294	0.00	0
199	35	35	ARG	CA	C	13	58.100	0.04	0
200	35	35	ARG	CB	C	13	31.662	0.16	0
201	35	35	ARG	CG	C	13	27.843	0.00	0
202	35	35	ARG	HA	H	1	4.433	0.00	0
203	35	35	ARG	HB2	H	1	1.957	0.00	0
204	35	35	ARG	HB3	H	1	1.844	0.00	0
205	35	35	ARG	HD2	H	1	2.662	0.00	0
206	35	35	ARG	HD3	H	1	2.683	0.01	0
207	36	36	THR	C	C	13	172.502	0.00	0
208	36	36	THR	CA	C	13	60.916	0.09	0
209	36	36	THR	CB	C	13	71.844	0.19	0
210	36	36	THR	CG2	C	13	22.609	0.00	0
211	36	36	THR	H	H	1	8.027	0.01	0
212	36	36	THR	HA	H	1	5.069	0.02	0
213	36	36	THR	HB	H	1	3.925	0.00	0
214	36	36	THR	HG2	H	1	1.139	0.00	0
215	36	36	THR	N	N	15	111.344	0.19	0
216	37	37	CYS	C	C	13	174.131	0.00	0
217	37	37	CYS	CA	C	13	55.244	0.10	0
218	37	37	CYS	CB	C	13	50.730	0.12	0
219	37	37	CYS	H	H	1	8.293	0.01	0
220	37	37	CYS	HA	H	1	5.205	0.00	0
221	37	37	CYS	HB3	H	1	3.504	0.00	0
222	37	37	CYS	N	N	15	120.866	0.05	0
223	38	38	THR	C	C	13	174.926	0.00	0
224	38	38	THR	CA	C	13	62.104	0.05	0

225	38	38	THR	CB	C	13	70.604	0.09	0
226	38	38	THR	CG2	C	13	21.910	0.00	0
227	38	38	THR	H	H	1	8.466	0.00	0
228	38	38	THR	HA	H	1	5.191	0.00	0
229	38	38	THR	HB	H	1	3.904	0.00	0
230	38	38	THR	HG2	H	1	1.173	0.00	0
231	38	38	THR	N	N	15	120.049	0.06	0
232	39	39	ASP	C	C	13	174.997	0.00	0
233	39	39	ASP	CA	C	13	57.072	0.07	0
234	39	39	ASP	CB	C	13	40.071	0.03	0
235	39	39	ASP	H	H	1	8.641	0.25	0
236	39	39	ASP	HA	H	1	5.050	0.04	0
237	39	39	ASP	HB2	H	1	3.014	0.00	0
238	39	39	ASP	HB3	H	1	2.625	0.00	0
239	39	39	ASP	N	N	15	125.520	2.95	0
240	40	40	SER	C	C	13	172.321	0.00	0
241	40	40	SER	CA	C	13	58.904	0.07	0
242	40	40	SER	CB	C	13	69.651	0.11	0
243	40	40	SER	H	H	1	8.085	0.00	0
244	40	40	SER	HA	H	1	5.641	0.00	0
245	40	40	SER	HB	H	1	4.339	0.00	0
246	40	40	SER	N	N	15	111.437	0.07	0
247	41	41	GLN	CA	C	13	53.981	0.02	0
248	41	41	GLN	CB	C	13	32.284	0.00	0
249	41	41	GLN	H	H	1	7.815	0.01	0
250	41	41	GLN	N	N	15	117.513	0.06	0
251	42	42	TYR	C	C	13	175.509	0.00	0
252	42	42	TYR	CA	C	13	57.684	0.05	0
253	42	42	TYR	CB	C	13	34.302	0.05	0
254	42	42	TYR	HB2	H	1	3.343	0.00	0
255	42	42	TYR	HB3	H	1	3.078	0.00	0
256	43	43	CYS	C	C	13	177.542	0.00	0
257	43	43	CYS	CA	C	13	58.019	0.12	0
258	43	43	CYS	CB	C	13	46.951	0.06	0
259	43	43	CYS	H	H	1	7.912	0.00	0
260	43	43	CYS	HA	H	1	4.799	0.00	0
261	43	43	CYS	HB2	H	1	3.785	0.00	0
262	43	43	CYS	HB3	H	1	2.855	0.00	0
263	43	43	CYS	N	N	15	119.608	0.06	0
264	44	44	ASN	C	C	13	173.488	0.00	0
265	44	44	ASN	CA	C	13	56.708	0.09	0
266	44	44	ASN	CB	C	13	40.330	0.02	0
267	44	44	ASN	H	H	1	7.618	0.15	0
268	44	44	ASN	HA	H	1	4.282	0.01	0
269	44	44	ASN	HB2	H	1	3.145	0.00	0
270	44	44	ASN	HB3	H	1	2.657	0.00	0
271	44	44	ASN	N	N	15	115.840	0.96	0
272	45	45	ASN	C	C	13	174.273	0.00	0
273	45	45	ASN	CA	C	13	53.156	0.10	0
274	45	45	ASN	CB	C	13	40.924	0.07	0
275	45	45	ASN	H	H	1	8.619	0.00	0
276	45	45	ASN	HA	H	1	4.960	0.01	0
277	45	45	ASN	HB2	H	1	2.792	0.01	0
278	45	45	ASN	HB3	H	1	2.574	0.06	0
279	45	45	ASN	N	N	15	114.061	0.06	0
280	46	46	ALA	C	C	13	177.783	0.00	0
281	46	46	ALA	CA	C	13	53.095	0.04	0

282	46	46	ALA	CB	C	13	19.770	0.05	0
283	46	46	ALA	H	H	1	7.024	0.00	0
284	46	46	ALA	HA	H	1	4.341	0.03	0
285	46	46	ALA	HB	H	1	1.321	0.04	0
286	46	46	ALA	N	N	15	126.112	0.05	0
287	47	47	MET	C	C	13	177.178	0.00	0
288	47	47	MET	CA	C	13	57.266	0.04	0
289	47	47	MET	CB	C	13	34.515	0.07	0
290	47	47	MET	CG	C	13	32.157	0.00	0
291	47	47	MET	H	H	1	9.357	0.01	0
292	47	47	MET	HA	H	1	4.668	0.02	0
293	47	47	MET	HB2	H	1	2.349	0.00	0
294	47	47	MET	HB3	H	1	2.284	0.01	0
295	47	47	MET	HE	H	1	2.163	0.00	0
296	47	47	MET	HG2	H	1	2.715	0.00	0
297	47	47	MET	HG3	H	1	2.831	0.00	0
298	47	47	MET	N	N	15	118.209	0.04	0
299	48	48	THR	C	C	13	172.391	0.00	0
300	48	48	THR	CA	C	13	61.021	0.10	0
301	48	48	THR	CB	C	13	71.268	0.08	0
302	48	48	THR	CG	C	13	21.557	0.00	0
303	48	48	THR	H	H	1	7.100	0.00	0
304	48	48	THR	HA	H	1	5.204	0.00	0
305	48	48	THR	HB	H	1	3.968	0.03	0
306	48	48	THR	HG2	H	1	1.166	0.00	0
307	48	48	THR	N	N	15	111.810	0.05	0
308	49	49	CYS	C	C	13	172.647	0.00	0
309	49	49	CYS	CA	C	13	55.024	0.06	0
310	49	49	CYS	CB	C	13	50.532	0.10	0
311	49	49	CYS	H	H	1	8.563	0.01	0
312	49	49	CYS	HA	H	1	5.133	0.00	0
313	49	49	CYS	HB2	H	1	3.691	0.00	0
314	49	49	CYS	HB3	H	1	3.221	0.00	0
315	49	49	CYS	N	N	15	123.852	0.07	0
316	50	50	THR	C	C	13	175.416	0.00	0
317	50	50	THR	CA	C	13	62.083	0.06	0
318	50	50	THR	CB	C	13	70.415	0.13	0
319	50	50	THR	CG2	C	13	21.775	0.00	0
320	50	50	THR	H	H	1	8.469	0.01	0
321	50	50	THR	HA	H	1	5.113	0.01	0
322	50	50	THR	HB	H	1	4.032	0.01	0
323	50	50	THR	HG2	H	1	1.128	0.00	0
324	50	50	THR	N	N	15	118.301	0.07	0
325	51	51	ARG	C	C	13	175.013	0.00	0
326	51	51	ARG	CA	C	13	57.177	0.16	0
327	51	51	ARG	CB	C	13	28.730	0.27	0
328	51	51	ARG	CD	C	13	42.863	0.00	0
329	51	51	ARG	H	H	1	9.249	0.01	0
330	51	51	ARG	HA	H	1	4.683	0.03	0
331	51	51	ARG	HB3	H	1	1.914	0.07	0
332	51	51	ARG	HD2	H	1	3.564	0.00	0
333	51	51	ARG	HD3	H	1	3.564	0.00	0
334	51	51	ARG	HG2	H	1	1.674	0.00	0
335	51	51	ARG	HG3	H	1	1.674	0.00	0
336	51	51	ARG	N	N	15	129.174	0.05	0
337	52	52	SER	C	C	13	173.083	0.00	0
338	52	52	SER	CA	C	13	58.007	0.08	0

339	52	52	SER	CB	C	13	68.706	0.12	0
340	52	52	SER	H	H	1	8.242	0.01	0
341	52	52	SER	HA	H	1	6.058	0.00	0
342	52	52	SER	HB2	H	1	4.127	0.00	0
343	52	52	SER	HB3	H	1	3.051	0.00	0
344	52	52	SER	N	N	15	111.558	0.07	0
345	53	53	THR	C	C	13	172.972	0.00	0
346	53	53	THR	CA	C	13	58.073	0.10	0
347	53	53	THR	CB	C	13	72.487	0.05	0
348	53	53	THR	CG2	C	13	19.342	0.00	0
349	53	53	THR	H	H	1	7.641	0.01	0
350	53	53	THR	HA	H	1	5.322	0.00	0
351	53	53	THR	N	N	15	108.270	0.03	0
352	54	54	ASP	C	C	13	175.597	0.00	0
353	54	54	ASP	CA	C	13	54.855	0.09	0
354	54	54	ASP	CB	C	13	37.825	0.17	0
355	54	54	ASP	H	H	1	8.021	0.00	0
356	54	54	ASP	HA	H	1	3.628	0.00	0
357	54	54	ASP	HB2	H	1	2.185	0.00	0
358	54	54	ASP	HB3	H	1	1.948	0.00	0
359	54	54	ASP	N	N	15	119.599	0.08	0
360	55	55	CYS	C	C	13	177.023	0.00	0
361	55	55	CYS	CA	C	13	57.398	0.10	0
362	55	55	CYS	CB	C	13	46.605	0.02	0
363	55	55	CYS	H	H	1	7.432	0.00	0
364	55	55	CYS	HA	H	1	4.667	0.02	0
365	55	55	CYS	HB2	H	1	3.822	0.00	0
366	55	55	CYS	HB3	H	1	2.789	0.00	0
367	55	55	CYS	N	N	15	118.877	0.03	0
368	56	56	PHE	C	C	13	176.047	0.00	0
369	56	56	PHE	CA	C	13	57.462	0.09	0
370	56	56	PHE	CB	C	13	39.628	0.07	0
371	56	56	PHE	H	H	1	6.749	0.00	0
372	56	56	PHE	HA	H	1	4.627	0.03	0
373	56	56	PHE	HB2	H	1	3.546	0.00	0
374	56	56	PHE	HB3	H	1	3.121	0.00	0
375	56	56	PHE	N	N	15	116.134	0.05	0
376	57	57	ASN	C	C	13	174.048	0.00	0
377	57	57	ASN	CA	C	13	52.964	0.04	0
378	57	57	ASN	CB	C	13	41.202	0.04	0
379	57	57	ASN	H	H	1	8.922	0.01	0
380	57	57	ASN	HA	H	1	5.027	0.00	0
381	57	57	ASN	HB3	H	1	2.354	0.00	0
382	57	57	ASN	N	N	15	113.374	0.07	0
383	58	58	ALA	C	C	13	177.519	0.00	0
384	58	58	ALA	CA	C	13	53.885	0.09	0
385	58	58	ALA	CB	C	13	19.938	0.18	0
386	58	58	ALA	H	H	1	6.825	0.00	0
387	58	58	ALA	HA	H	1	3.205	1.36	0
388	58	58	ALA	HB	H	1	1.609	0.00	0
389	58	58	ALA	N	N	15	124.237	0.04	0
390	59	59	ILE	C	C	13	176.735	0.00	0
391	59	59	ILE	CA	C	13	62.425	0.08	0
392	59	59	ILE	CB	C	13	39.028	0.12	0
393	59	59	ILE	CD1	C	13	13.184	0.00	0
394	59	59	ILE	CG1	C	13	28.160	0.01	0
395	59	59	ILE	CG2	C	13	18.118	0.09	0

396	59	59	ILE	H	H	1	8.561	0.00	0
397	59	59	ILE	HA	H	1	4.411	0.03	0
398	59	59	ILE	HB	H	1	2.070	0.03	0
399	59	59	ILE	HD1	H	1	1.013	0.00	0
400	59	59	ILE	HG12	H	1	1.757	0.00	0
401	59	59	ILE	HG13	H	1	1.446	0.00	0
402	59	59	ILE	HG2	H	1	1.156	0.00	0
403	59	59	ILE	N	N	15	119.290	0.03	0
404	60	60	THR	C	C	13	172.860	0.00	0
405	60	60	THR	CA	C	13	61.279	0.09	0
406	60	60	THR	CB	C	13	71.110	0.19	0
407	60	60	THR	CG	C	13	21.404	0.03	0
408	60	60	THR	H	H	1	7.367	0.00	0
409	60	60	THR	HA	H	1	5.146	0.02	0
410	60	60	THR	HB	H	1	4.013	0.02	0
411	60	60	THR	HG2	H	1	1.102	0.00	0
412	60	60	THR	N	N	15	115.445	0.08	0
413	61	61	CYS	C	C	13	172.046	0.00	0
414	61	61	CYS	CA	C	13	55.080	0.13	0
415	61	61	CYS	CB	C	13	49.960	0.06	0
416	61	61	CYS	H	H	1	8.996	0.00	0
417	61	61	CYS	HA	H	1	5.264	0.00	0
418	61	61	CYS	HB2	H	1	3.317	0.00	0
419	61	61	CYS	HB3	H	1	3.240	0.06	0
420	61	61	CYS	N	N	15	125.486	0.04	0
421	62	62	ILE	C	C	13	177.060	0.00	0
422	62	62	ILE	CA	C	13	60.569	0.08	0
423	62	62	ILE	CB	C	13	40.989	0.03	0
424	62	62	ILE	CD1	C	13	13.557	0.00	0
425	62	62	ILE	CG1	C	13	28.162	0.01	0
426	62	62	ILE	CG2	C	13	17.696	0.10	0
427	62	62	ILE	H	H	1	8.669	0.00	0
428	62	62	ILE	HA	H	1	4.795	0.00	0
429	62	62	ILE	HB	H	1	1.863	0.00	0
430	62	62	ILE	HB12	H	1	1.418	0.00	0
431	62	62	ILE	HB13	H	1	1.428	0.00	0
432	62	62	ILE	HD1	H	1	0.895	0.00	0
433	62	62	ILE	HG12	H	1	1.418	0.00	0
434	62	62	ILE	HG13	H	1	1.428	0.00	0
435	62	62	ILE	HG2	H	1	1.028	0.00	0
436	62	62	ILE	N	N	15	121.433	0.05	0
437	63	63	ASP	C	C	13	175.244	0.00	0
438	63	63	ASP	CA	C	13	55.838	0.07	0
439	63	63	ASP	CB	C	13	40.240	0.10	0
440	63	63	ASP	H	H	1	9.124	0.01	0
441	63	63	ASP	HA	H	1	5.004	0.03	0
442	63	63	ASP	HB2	H	1	3.101	0.00	0
443	63	63	ASP	HB3	H	1	2.699	0.00	0
444	63	63	ASP	N	N	15	132.149	0.04	0
445	64	64	SER	C	C	13	173.510	0.00	0
446	64	64	SER	CA	C	13	59.065	0.08	0
447	64	64	SER	CB	C	13	68.552	0.08	0
448	64	64	SER	H	H	1	8.589	0.00	0
449	64	64	SER	HA	H	1	5.822	0.00	0
450	64	64	SER	HB2	H	1	4.075	0.00	0
451	64	64	SER	HB3	H	1	3.193	0.00	0
452	64	64	SER	N	N	15	112.403	0.03	0

453	65	65	THR	C	C	13	172.784	0.00	0
454	65	65	THR	CA	C	13	58.245	0.10	0
455	65	65	THR	CB	C	13	72.527	0.08	0
456	65	65	THR	CG2	C	13	22.170	0.04	0
457	65	65	THR	H	H	1	7.839	0.00	0
458	65	65	THR	HA	H	1	5.276	0.02	0
459	65	65	THR	HB	H	1	4.080	0.00	0
460	65	65	THR	HG2	H	1	1.075	0.00	0
461	65	65	THR	N	N	15	108.706	0.03	0
462	66	66	ASN	C	C	13	173.238	0.00	0
463	66	66	ASN	CA	C	13	53.795	0.08	0
464	66	66	ASN	CB	C	13	36.477	0.07	0
465	66	66	ASN	H	H	1	7.865	0.01	0
466	66	66	ASN	HA	H	1	4.321	0.00	0
467	66	66	ASN	HB2	H	1	2.533	0.00	0
468	66	66	ASN	HB3	H	1	2.659	0.00	0
469	66	66	ASN	N	N	15	117.246	0.07	0
470	67	67	CYS	C	C	13	176.903	0.00	0
471	67	67	CYS	CA	C	13	57.143	0.08	0
472	67	67	CYS	CB	C	13	46.653	0.07	0
473	67	67	CYS	H	H	1	8.203	0.00	0
474	67	67	CYS	HA	H	1	4.753	0.03	0
475	67	67	CYS	HB2	H	1	3.569	0.00	0
476	67	67	CYS	HB3	H	1	3.013	0.00	0
477	67	67	CYS	N	N	15	116.582	0.04	0
478	68	68	TYR	C	C	13	177.556	0.00	0
479	68	68	TYR	CA	C	13	57.174	0.05	0
480	68	68	TYR	CB	C	13	38.439	0.12	0
481	68	68	TYR	H	H	1	6.560	0.00	0
482	68	68	TYR	HA	H	1	4.814	0.01	0
483	68	68	TYR	HB2	H	1	3.305	0.00	0
484	68	68	TYR	HB3	H	1	2.999	0.00	0
485	68	68	TYR	N	N	15	114.561	0.03	0
486	69	69	LYS	C	C	13	176.383	0.00	0
487	69	69	LYS	CA	C	13	54.863	0.04	0
488	69	69	LYS	CB	C	13	34.199	0.08	0
489	69	69	LYS	CD	C	13	29.477	0.04	0
490	69	69	LYS	CE	C	13	42.381	0.00	0
491	69	69	LYS	CG	C	13	25.191	0.09	0
492	69	69	LYS	H	H	1	9.704	0.01	0
493	69	69	LYS	HA	H	1	4.559	0.02	0
494	69	69	LYS	HB2	H	1	1.978	0.00	0
495	69	69	LYS	HB3	H	1	1.978	0.00	0
496	69	69	LYS	HD2	H	1	1.762	0.00	0
497	69	69	LYS	HD3	H	1	1.735	0.00	0
498	69	69	LYS	HE2	H	1	3.095	0.00	0
499	69	69	LYS	HG2	H	1	1.485	0.00	0
500	69	69	LYS	HG3	H	1	1.485	0.00	0
501	69	69	LYS	N	N	15	118.489	0.06	0
502	70	70	ALA	C	C	13	177.644	0.00	0
503	70	70	ALA	CA	C	13	54.807	0.06	0
504	70	70	ALA	CB	C	13	19.979	0.07	0
505	70	70	ALA	H	H	1	7.096	0.00	0
506	70	70	ALA	HA	H	1	4.434	0.03	0
507	70	70	ALA	HB	H	1	1.402	0.00	0
508	70	70	ALA	N	N	15	124.689	0.04	0
509	71	71	THR	C	C	13	176.380	0.00	0

510	71	71	THR	CA	C	13	62.735	0.07	0
511	71	71	THR	CB	C	13	69.173	0.16	0
512	71	71	THR	CG2	C	13	22.511	0.01	0
513	71	71	THR	H	H	1	8.529	0.01	0
514	71	71	THR	HA	H	1	4.385	0.00	0
515	71	71	THR	HB	H	1	4.385	0.00	0
516	71	71	THR	HG2	H	1	1.302	0.00	0
517	71	71	THR	N	N	15	114.607	0.03	0
518	72	72	THR	CA	C	13	63.574	0.04	0
519	72	72	THR	CB	C	13	69.303	0.00	0
520	72	72	THR	H	H	1	7.920	0.00	0
521	72	72	THR	HA	H	1	4.483	0.00	0
522	72	72	THR	N	N	15	120.284	0.02	0
523	73	73	CYS	C	C	13	172.370	0.00	0
524	73	73	CYS	CA	C	13	55.760	0.08	0
525	73	73	CYS	CB	C	13	45.560	0.09	0
526	73	73	CYS	HA	H	1	5.006	0.02	0
527	73	73	CYS	HB2	H	1	3.617	0.00	0
528	73	73	CYS	HB3	H	1	2.589	0.00	0
529	74	74	ILE	CA	C	13	60.733	0.16	0
530	74	74	ILE	CB	C	13	38.937	0.00	0
531	74	74	ILE	H	H	1	8.907	0.00	0
532	74	74	ILE	HA	H	1	4.420	0.00	0
533	74	74	ILE	N	N	15	126.997	0.03	0
534	75	75	ASN	C	C	13	173.699	0.00	0
535	75	75	ASN	CA	C	13	54.110	0.13	0
536	75	75	ASN	CB	C	13	37.635	0.10	0
537	75	75	ASN	H	H	1	8.036	0.00	0
538	75	75	ASN	HA	H	1	4.476	0.00	0
539	75	75	ASN	HB2	H	1	3.526	0.00	0
540	75	75	ASN	HB3	H	1	2.752	0.00	0
541	75	75	ASN	N	N	15	122.158	0.00	0
542	76	76	SER	C	C	13	173.008	0.00	0
543	76	76	SER	CA	C	13	57.824	0.09	0
544	76	76	SER	CB	C	13	67.963	0.05	0
545	76	76	SER	H	H	1	7.606	0.00	0
546	76	76	SER	HA	H	1	5.765	0.01	0
547	76	76	SER	HB2	H	1	3.923	0.00	0
548	76	76	SER	HB3	H	1	3.525	0.00	0
549	76	76	SER	N	N	15	109.678	0.03	0
550	77	77	THR	C	C	13	174.800	0.00	0
551	77	77	THR	CA	C	13	59.788	0.07	0
552	77	77	THR	CB	C	13	71.023	0.07	0
553	77	77	THR	CG2	C	13	22.508	0.00	0
554	77	77	THR	H	H	1	8.067	0.00	0
555	77	77	THR	HA	H	1	4.662	0.16	0
556	77	77	THR	HG2	H	1	1.232	0.00	0
557	77	77	THR	N	N	15	111.918	0.04	0
558	78	78	GLY	C	C	13	172.805	0.00	0
559	78	78	GLY	CA	C	13	46.323	0.04	0
560	78	78	GLY	H	H	1	8.811	0.00	0
561	78	78	GLY	HA2	H	1	3.829	0.00	0
562	78	78	GLY	HA3	H	1	3.853	0.02	0
563	78	78	GLY	N	N	15	108.349	0.03	0
564	79	79	CYS	CA	C	13	53.294	0.00	0
565	79	79	CYS	CB	C	13	42.152	0.00	0
566	79	79	CYS	H	H	1	7.773	0.00	0

567	79	79	CYS	HA	H	1	4.988	0.00	0
568	79	79	CYS	N	N	15	116.861	0.03	0
569	80	80	PRO	C	C	13	177.063	0.00	0
570	80	80	PRO	CA	C	13	63.434	0.08	0
571	80	80	PRO	CB	C	13	31.896	0.06	0
572	80	80	PRO	CD	C	13	50.674	0.00	0
573	80	80	PRO	CG	C	13	27.459	0.00	0
574	80	80	PRO	HA	H	1	4.440	0.00	0
575	80	80	PRO	HB2	H	1	2.258	0.00	0
576	80	80	PRO	HB3	H	1	2.258	0.00	0
577	80	80	PRO	HD2	H	1	3.912	0.00	0
578	80	80	PRO	HD3	H	1	3.905	0.00	0
579	80	80	PRO	HG2	H	1	1.857	0.00	0
580	80	80	PRO	HG3	H	1	1.857	0.00	0
581	81	81	LYS	C	C	13	176.488	0.00	0
582	81	81	LYS	CA	C	13	56.225	0.12	0
583	81	81	LYS	CB	C	13	32.877	0.10	0
584	81	81	LYS	CD	C	13	27.063	0.00	0
585	81	81	LYS	CG	C	13	19.446	0.00	0
586	81	81	LYS	H	H	1	8.360	0.00	0
587	81	81	LYS	HA	H	1	4.412	0.00	0
588	81	81	LYS	HB2	H	1	1.958	0.00	0
589	81	81	LYS	HB3	H	1	1.943	0.00	0
590	81	81	LYS	HD2	H	1	1.715	0.00	0
591	81	81	LYS	HD3	H	1	1.705	0.00	0
592	81	81	LYS	HE3	H	1	2.271	0.00	0
593	81	81	LYS	HG2	H	1	1.381	0.00	0
594	81	81	LYS	HG3	H	1	1.381	0.00	0
595	81	81	LYS	N	N	15	121.297	0.06	0
596	82	82	HIS	C	C	13	174.703	0.00	0
597	82	82	HIS	CA	C	13	55.627	0.15	0
598	82	82	HIS	CB	C	13	30.425	0.11	0
599	82	82	HIS	H	H	1	8.281	0.01	0
600	82	82	HIS	HA	H	1	4.682	0.00	0
601	82	82	HIS	HB2	H	1	3.150	0.00	0
602	82	82	HIS	HB3	H	1	3.150	0.00	0
603	82	82	HIS	N	N	15	120.020	0.20	0
604	83	83	LYS	C	C	13	176.057	0.00	0
605	83	83	LYS	CA	C	13	56.409	0.20	0
606	83	83	LYS	CB	C	13	33.156	0.15	0
607	83	83	LYS	CD	C	13	29.115	0.00	0
608	83	83	LYS	CE	C	13	42.183	0.00	0
609	83	83	LYS	CG	C	13	24.559	0.00	0
610	83	83	LYS	H	H	1	8.319	0.01	0
611	83	83	LYS	HA	H	1	4.333	0.00	0
612	83	83	LYS	HB2	H	1	1.751	0.00	0
613	83	83	LYS	HB3	H	1	1.751	0.00	0
614	83	83	LYS	HD1	H	1	1.547	0.00	0
615	83	83	LYS	HD2	H	1	1.544	0.00	0
616	83	83	LYS	HE2	H	1	2.983	0.00	0
617	83	83	LYS	HE3	H	1	2.983	0.00	0
618	83	83	LYS	HG2	H	1	1.383	0.00	0
619	83	83	LYS	HG3	H	1	1.383	0.00	0
620	83	83	LYS	N	N	15	123.382	0.07	0
621	84	84	VAL	C	C	13	175.904	0.00	0
622	84	84	VAL	CA	C	13	57.531	11.03	0
623	84	84	VAL	CB	C	13	32.843	0.06	0

624	84	84	VAL	CG1	C	13	21.251	0.00	0
625	84	84	VAL	CG2	C	13	20.778	0.00	0
626	84	84	VAL	H	H	1	8.211	0.01	0
627	84	84	VAL	N	N	15	122.965	0.05	0
628	85	85	VAL	C	C	13	175.617	0.00	0
629	85	85	VAL	CA	C	13	62.197	0.11	0
630	85	85	VAL	CB	C	13	33.110	0.24	0
631	85	85	VAL	CG1	C	13	21.200	0.00	0
632	85	85	VAL	CG2	C	13	20.494	0.00	0
633	85	85	VAL	H	H	1	8.282	0.00	0
634	85	85	VAL	HA	H	1	4.132	0.00	0
635	85	85	VAL	HB	H	1	2.033	0.00	0
636	85	85	VAL	HG2	H	1	0.986	0.00	0
637	85	85	VAL	HG3	H	1	0.850	0.00	0
638	85	85	VAL	N	N	15	125.638	0.03	0
639	86	86	LYS	C	C	13	175.218	0.00	0
640	86	86	LYS	CA	C	13	56.268	0.07	0
641	86	86	LYS	CB	C	13	33.213	0.08	0
642	86	86	LYS	CD	C	13	29.026	0.00	0
643	86	86	LYS	CE	C	13	42.340	0.00	0
644	86	86	LYS	CG	C	13	24.553	0.00	0
645	86	86	LYS	H	H	1	8.347	0.00	0
646	86	86	LYS	HA	H	1	4.353	0.00	0
647	86	86	LYS	HB2	H	1	1.870	0.00	0
648	86	86	LYS	HB3	H	1	1.885	0.00	0
649	86	86	LYS	HD2	H	1	1.672	0.00	0
650	86	86	LYS	HD3	H	1	1.672	0.00	0
651	86	86	LYS	HE2	H	1	2.977	0.00	0
652	86	86	LYS	HE3	H	1	2.977	0.00	0
653	86	86	LYS	HG2	H	1	1.419	0.00	0
654	86	86	LYS	HG3	H	1	1.419	0.00	0
655	86	86	LYS	N	N	15	126.823	0.03	0
656	87	87	LYS	CA	C	13	57.909	0.12	0
657	87	87	LYS	CB	C	13	33.753	0.00	0
658	87	87	LYS	H	H	1	7.960	0.00	0
659	87	87	LYS	N	N	15	129.111	0.02	0

Supplemental Information

The effects of high concentrations of an ionic liquid on GB1 protein structure and dynamics probed by high-resolution magic-angle-spinning NMR spectroscopy

Lisa R. Warner[a,b], Erica Gjersing[a], Shelby E. Follett[c], K. Wade Elliott[c], Sergei V. Dzyuba[d], and Krisztina Varga[c,e*]

[a] National Renewable Energy Laboratory, Golden, CO, 80401, USA

[b] Current address: Biomolecular Research Center, Boise State University, Boise, ID 83725-1511, USA

[c] Department of Chemistry, University of Wyoming, Laramie, WY, 82071, USA

[d] Department of Chemistry and Biochemistry, Texas Christian University, Fort Worth, TX, 76129 USA

[e] Current address: Department of Molecular, Cellular, and Biomedical Sciences, University of New Hampshire, Durham, NH, USA

* Corresponding author; Email: krisztina.varga@unh.edu

Table of contents

Materials and Methods

Synthesis of [C_4-mim]Br

[C_4-mim]Br was prepared according to literature procedures [124,125]. It was treated with charcoal and repetitive dissolutions into CH_2Cl_2, followed by filtration and removal of CH_2Cl_2 to get rid of colored impurities; subsequently it was dried using an EtOH azeotrope, and left on the vacuum for at least 12 hours prior to use to remove residual solvents.

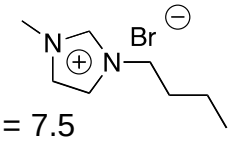

[C_4-mim]Br: ^{1}H NMR (Varian 300 MHz; *acetone-d_6*) δ = 10.21 (1H, s), 7.88 (1H, s), 7.80 (1H, s), 4.44 (2H, t, *J* = 7.5 Hz), 4.10 (s, 3H), 1.93 (2H, pent, *J* = 7.5 Hz), 1.37 (2H, sept, *J* = 7.5 Hz), 0.94 (3H, t, *J* = 7.5 Hz) [124,125].

Viscosity measurements

Viscosities of neat [C_4-mim]Br and all solutions used in this study were measured using an Anton-Paar Lovis 4500M microviscometer. Following the viscosity measurements, the water content of [C_4-mim]Br was measured using Aquamax KF coulometric titrator from GRS Scientific according to manufacturer provided protocols, using 0.8 mL of the sample; the average of two runs was reported. Sodium phosphate buffer (50 mM, pH 5.5) was prepared as follows: a 1 M solution of NaH_2PO_4 was diluted to 50 mM and the pH was adjusted to 5.5 using a freshly prepared 10 M solution of NaOH. See Table S5 for more details.

NMR experiments

GB1 was prepared as previously described [126]. The GB1 stock solution contained 27.2 mg/mL (4.4 mM) protein in 50 mM sodium phosphate buffer, pH 5.50. For HR-MAS experiments, NMR samples were packed into 50 µL Bruker rotors. Each 50 µL sample was prepared by mixing 15 µL of 4.4 mM GB1 stock (1.3 mM final concentration), 10 µL of D_2O (20% v/v final concentration), and 25 µL of various concentrations of [C_4-mim]Br (10%, 25%, 40%, and 50% v/v final concentration) mixed with phosphate buffer (50 mM sodium phosphate buffer, pH 5.5). For the 60% v/v [C_4-mim]Br sample, 30 µL of [C_4-mim]Br had to be added, thus only 10 µL of the GB1 stock was used (to 0.9 mM final concentration). Other samples included GB1 in glycerol/water (50% v/v) and 4.6 M KBr in H_2O (2.3 M final concentration). A control GB1 sample was prepared without the addition of [C_4-mim]Br or KBr (referred to in the text as aqueous control or 0% v/v [C_4-mim]Br sample). It was found that a minimum of 10 µL of D_2O (20% v/v final concentration) was required to maintain a stable lock signal over several days. There was no significant pH variation between the [C_4-mim]Br mixtures. See Table S1 for summary of sample conditions. Samples were stored at -20 °C in the rotor between experiments. The GB1 samples were stable for at least two years under these conditions.

HR-MAS NMR spectra were acquired on a 600 MHz Avance III Bruker NMR spectrometer equipped with a 4 mm HR-MAS probe. 1D ^{1}H, 1D ^{13}C, 2D ^{1}H-^{15}N Heteronuclear Single Quantum Coherence (HSQC) and 3D HNCA spectra were acquired at 27 °C and 5 kHz MAS frequency using standard Bruker pulse sequences (with sensitivity improvement for multi-dimensional spectra). The ^{1}H 90° pulse increased from 4.66 µs at 0% v/v [C_4-mim]Br to 7.5 µs and 8.1 µs in the presence of 2.3 M KBr and 60%

v/v (3.53 M) [C_4-mim]Br, respectively. 1D ^{13}C spectra of GB1 in 0-50% v/v [C_4-mim]Br were acquired by averaging 2018 scans with a 2-s pulse delay over 1 h 13 min using a 108 ms acquisition. As the concentration of GB1 in the 60% v/v [C_4-mim]Br was lower, 4096 scans were acquired. The 2D ^{1}H-^{15}N HSQC spectra and 3D HNCA spectra at 600 MHz were collected with parameters shown in Table S2. Relaxation datasets were collected with parameters shown in Table S3. Solution NMR 2D ^{1}H-^{15}N HSQC spectrum of GB1 in 50% v/v [C_4-mim]Br was acquired using a Cold probe on a VNMRS 900 MHz spectrometer.

Spectra were externally referenced to DSS (27 °C and 5 kHz MAS frequency). ^{1}H 90° pulse lengths ranged from 4.66 µs (0% v/v [C_4-mim]Br) to 7.93 µs (60% v/v [C_4-mim]Br). GB1 chemical shifts were assigned based on published chemical shifts (BMRB [143] entry 7280 [127]) and analysis of the 3D HNCA spectra.

All data were processed using NMRPipe [144]. Analysis and assignments of the 2D and 3D data sets were carried out using CCPNMR [145] and Sparky [146]. Chemical shift perturbations were determined by subtracting the chemical shift (ppm) of each residue of GB1 in aqueous solution (control) from the chemical shift (ppm) of GB1 in the presence of [C_4-mim]Br, glycerol, or KBr. Combined ^{1}H and ^{15}N chemical shift perturbations (ΔHN) were calculated using the following equation:

Eq. S1. $$\Delta HN = ((\Delta H)^2 + (0.15 \times \Delta N)^2)^{0.5}$$

where ΔH and ΔN are the chemical shift perturbations in ppm for ^{1}H and ^{15}N respectively [133,147].

Relaxation parameters, T_1 or T_2, were calculated by fitting the peak heights of the HSQC spectra at different relaxation delays to an exponential decay equation. Specifically, the peak heights were measured using the nlinLS module included in the NMRPipe analysis package[144]. The values and errors for the residue specific T_1 and T_2's were calculated from the average and standard deviations after 10,000 Monte Carlo trials of fitting an exponential decay equation to the peak heights using a home written python script. The ideal number of Monte Carlo trials was determined empirically as the minimum number of trials necessary for convergence of 50% [C_4-mim]Br data, as this was the lowest quality dataset.

The residue specific τ_c was calculated by numerically solving for the ratio of the average T_1 and T_2 relaxation rates of rigid amide ^{15}N spins, given by equation 8 in Kay *et al.* [148], using the simplified spectral density function (equation 9 in Kay *et al.* [148]) and assuming a rigid, isotropically tumbling N-H bond vector (S^2=1), a bond length of 1.02 Å and a nitrogen frequency of 60.8209826 MHz. The average τ_c was calculated using experimental T_1 and T_2 data that were pruned to include only rigid residues with hetNOE values greater than 0.7.

T_1 and T_2 relaxation are due to dipolar coupling of a ^{15}N amide covalently bound to a proton and by chemical shift anisotropy and can be described using the spectral density function [149]. The theoretical T_1 and T_2 curves in Fig. 3 were calculated with a home written Mathematica script from the relaxation rates of an amide ^{15}N spin relaxed by dipolar coupling to a directly bonded proton and by chemical shift anisotropy given by Abragam [149] using the Lipari-Szabo formalism [150,151] and described in detail by Kay [148]. The simulated T_1 and T_2 lines were plotted as a function of the τ_c.

The tumbling rate was also estimated using Stoke's law following the equation [152]:

Eq.S2. $$\tau_c = \frac{4\pi\eta r^3}{3KT}$$

using the effective hydrodynamic radius equation:

Eq. S3. $$r = \sqrt[3]{\frac{3M}{4\pi\rho N_a}} + r_w$$

where η is the viscosity, r is the effective hydrodynamic radius, K is the Boltzmann constant, T is the temperature, M is the molar mass, ρ is the density, N_a is Avogadro's number, and r_w is the radius of hydration. The NMR based τ_c values were in a relatively good agreement with values calculated using Stoke's law, especially at lower viscosities. Thus, while it was reported that GB1 had an ellipsoid shape with a $D_{\parallel}/D_{\perp}$ ratio of 1.6-1.7 [153], for the simple analyses of the relaxation data presented here, a spherical approximation was adequate.

In order to estimate the actual sample temperature under HR-MAS conditions (27 °C and 5 kHz MAS frequency), traditional solution 2D ^{1}H-^{15}N HSQC NMR spectra of GB1 protein were acquired using a 5 mm SmartProbe™ at various temperatures: 24 °C, 27 °C, 30 °C, 33 °C, and 36 °C. HSQC NMR spectra of GB1 acquired under HR-MAS conditions was compared to the traditional solution NMR spectra.

Although the experiments were carried out at 27 °C VT inlet gas temperature, the MAS rotation increased the actual sample temperature slightly. It is well known that amide chemical shifts are sensitive to temperature [154,155]. We estimated that the actual sample temperature was approximately 30-31 °C based on comparison of GB1 2D ^{1}H-^{15}N HSQC spectra under HR-MAS conditions to conventional solution GB1 2D ^{1}H-^{15}N HSQC spectra at various temperatures (Fig. S1).

Table S1. Composition of the samples

GB1 (mM)	[C_4-mim]Br		Glycerol (%, v/v)	KBr (M)	D_2O (%, v/v)
	% (v/v)	M			
1.3	–	–	–	–	20
1.3	10	0.59	–	–	20
1.3	25	1.47	–	–	20
1.3	40	2.36	–	–	20
1.3	50	2.95	–	–	20
0.9	60	3.53	–	–	20
1.3			50	–	20
1.3			–	2.29	20

Table S2. Experimental parameters for 2D and 3D datasets.

I.			^{1}H			^{15}N			^{13}C		
Sample Name*	# of scans	# of points	sweep width (ppm)	acquisition time (ms)	# of points	sweep width (ppm)	acquisition time (ms)	# of points	sweep width (Hz)	acquisition time (ms)	interscan delay (s)
HSQC 0IL	32	2048	18.0326	94.6	200	30	51.38	--	--	--	1.0
HSQC 10IL	32	2048	18.0326	94.6	200	32	54.8	--	--	--	1.0
HSQC 25IL	32	2048	18.0326	94.6	200	32	54.8	--	--	--	1.0
HSQC 50IL	32	2048	18.0326	94.6	200	32	54.8	--	--	--	1.0
HSQC 50IL											
HSQC 60IL	128	2048	18.0326	94.6	256	30	70.1	--	--	--	1.0
HSQC 60IL	256	2048	18.0326	94.6	256	30	70.1	--	--	--	1.0
HSQC 40IL	32	2048	18.0326	94.6	200	32	54.8	--	--	--	1.0
HSQC 40IL diluted	32	2048	18.0326	94.6	200	32	54.8	--	--	--	1.0
HSQC glycerol	32	2048	18.0326	94.6	200	32	54.8	--	--	--	1.0
HSQC KBr	16	2048	18.0326	94.6	256	32	65.8	--	--	--	1.0
HSQC 600cryo	32	2048	18.0326	94.6	200	32	51.38	--	--	--	1.0
HSQC 900cryo	8	2604	14.466	100	128	27.8	30	--	--	--	1.7
HNCA 0IL	8	2048	18.0326	94.6	64	23.5	22.4	128	25.0	17.0	1.0
HNCA 10IL	8	2048	18.0326	94.6	60	30	16.4	121	25.0	16.0	1.0
HNCA 25IL	16	2048	18.0326	94.6	80	30	21.9	150	25.0	19.8	1.0
HNCA 50IL	16	2048	18.0326	94.6	64	23.5	22.4	128	25.0	17.0	1.0

* "% v/v [C_4-mim]Br" is abbreviated to "IL"

Table S3. Experimental parameters for relaxation experiments

			^{1}H			^{15}N		
Sample Name*	# of scans	# of points	sweep width (ppm)	acquisition time (ms)	# of points	sweep width (ppm)	acquisition time (ms)	interscan delay (s)
T1 0IL	24	1024	16.0213	53.2	256	23.5	89.5	1.0
T1 25IL	32	1024	16.0213	53.2	256	30	70.2	1.0
T1 50IL	40	1024	16.0213	53.2	234	30	64.1	1.0
T2 0IL	24	1024	16.0213	53.2	154	30	42.2	1.0
T2 25IL	64	1024	16.0213	53.2	154	30	42.2	1.0
T2 50IL	64	1024	16.0213	53.2	154	30	42.2	1.0

	T1 times (ms)	48.13	**T2 times (ms)**	15.22	* indicates duplicated experiment
		148.13*		30.4*	
		248.13		45.32	
		348.13		76.1	
		448.13*		106.54*	
		548.13		136.98	

			^{1}H			^{15}N		
Sample Name*	# of scans	# of points	sweep width (ppm)	acquisition time (ms)	# of points	sweep width (ppm)	acquisition time (ms)	interscan delay (s)
hetNOE 0IL	32	2048	18.0326	94.6	256	23.5	44.75	3.0
hetNOE 25IL	80	2048	18.0326	94.6	256	23.5	44.75	3.0
hetNOE 50IL	160	2048	18.0326	94.6	256	23.5	44.75	3.0

* "% v/v [C_4-mim]Br" is abbreviated to "IL"

Table S4. Talos+ predicted secondary structure for 0, 25, and 50% v/v [C_4-mim]Br.

		0IL		10IL		25IL		50IL	
Residue	**Name**	**Confidence**	**SS**	**Confidence**	**SS**	**Confidence**	**SS**	**Confidence**	**SS**
1	M	0	X	0	X	0	X	0	X
2	Q	0.76	E	0.79	E	0.74	E	0.77	E
3	Y	0.7	E	0.77	E	0.66	E	0.71	E
4	K	0.94	E	0.95	E	0.95	E	0.96	E
5	L	0.99	E	0.99	E	0.99	E	0.98	E
6	I	0.98	E	0.98	E	0.98	E	0.98	E
7	L	0.88	E	0.89	E	0.88	E	0.9	E
8	N	0.33	E	0.36	E	0.34	E	0.48	E
9	G	0.81	L	0.8	L	0.8	L	0.77	L
10	K	0.91	L	0.91	L	0.91	L	0.91	L
11	T	0.68	L	0.73	L	0.74	L	0.74	L
12	L	0.1	L	0.32	L	0.42	L	0.56	L
13	K	0.5	E	0.45	E	0.44	E	0.26	L
14	G	0.49	E	0.49	E	0.43	E	0.63	L
15	E	0.4	E	0.36	E	0.23	E	0.43	L
16	T	0.09	L	0.17	L	0.33	L	0.34	L
17	T	0.16	L	0.29	L	0.09	L	0.15	L
18	T	0.52	E	0.2	E	0.54	E	0.47	E
19	E	0.73	E	0.56	E	0.73	E	0.65	E
20	A	0.32	E	0.32	E	0.31	E	0.28	E
21	V	0.76	L	0.75	L	0.75	L	0.69	L
22	D	0.85	L	0.84	L	0.82	L	0.78	L
23	A	0.47	H	0.49	H	0.67	H	0.63	H
24	A	0.94	H	0.94	H	0.98	H	0.96	H
25	T	1	H	1	H	1	H	1	H
26	A	0.99	H	0.99	H	0.99	H	0.99	H
27	E	0.99	H	0.99	H	0.98	H	0.99	H
28	K	0.97	H	0.97	H	0.98	H	0.98	H
29	V	0.89	H	0.9	H	0.92	H	0.95	H
30	F	0.83	H	0.84	H	0.89	H	0.93	H
31	K	0.97	H	0.97	H	0.98	H	0.99	H
32	Q	0.98	H	0.98	H	0.98	H	0.98	H
33	Y	0.99	H	0.99	H	0.99	H	0.99	H
34	A	1	H	1	H	1	H	1	H
35	N	0.94	H	0.94	H	0.96	H	0.96	H
36	D	0.55	H	0.55	H	0.61	H	0.63	H
37	N	0.58	L	0.58	L	0.5	L	0.47	L
38	G	0.85	L	0.85	L	0.85	L	0.86	L
39	V	0.74	L	0.77	L	0.77	L	0.73	L
40	D	0.57	L	0.66	L	0.63	L	0.57	L
41	G	0.74	L	0.77	L	0.7	L	0.64	L
42	E	0.36	L	0.34	L	0.08	L	0.2	E
43	W	0.3	L	0.3	L	0.21	L	0.06	E
44	T	0.46	E	0.41	E	0.49	E	0.62	E
45	Y	0.65	E	0.6	E	0.64	E	0.69	E
46	D	0.03	L	0.12	L	0.03	E	0.07	E
47	D	0.73	L	0.74	L	0.72	L	0.7	L
48	A	0.8	L	0.8	L	0.79	L	0.73	L
49	T	0.88	L	0.87	L	0.87	L	0.84	L
50	K	0.83	L	0.83	L	0.85	L	0.84	L
51	T	0.2	E	0.19	E	0.08	E	0.02	L
52	F	0.82	E	0.81	E	0.78	E	0.69	E
53	T	0.93	E	0.92	E	0.92	E	0.89	E
54	V	0.89	E	0.89	E	0.89	E	0.89	E
55	T	0.83	E	0.83	E	0.83	E	0.83	E
56	E	0	L	0	L	0	L	0	L

Table S5. Viscosities of [C_4-mim]Br, its solutions and glycerol-containing sample as a function of temperature.

Solvent system	T / ^{o}C	Viscosity / cP
[C_4-mim]Br[a]	27 32 37	433 306 223
[C_4-mim]Br (60 %, v/v) D_2O (20 %, v/v) Buffer[b] (20 %, v/v)	27 32 37	6.0 5.2 4.5
[C_4-mim]Br (50 %, v/v) D_2O (20 %, v/v) Buffer[b] (30 %, v/v)	27 32 37	4.1 3.6 3.1
[C_4-mim]Br (40 %, v/v) D_2O (20 %, v/v) Buffer[b] (70 %, v/v)	27 32 37	2.8 2.4 2.2
[C_4-mim]Br (25 %, v/v) D_2O (20 %. v/v) Buffer[b] (70 %, v/v)	27 32 37	1.8 1.6 1.4
[C_4-mim]Br (10 %, v/v) D_2O (20 %, v/v) Buffer[b] (70 %, v/v)	27 32 37	1.3 1.2 1.1
[C_4-mim]Br (0 %, v/v) D_2O (20 %, v/v) Buffer[b] (70 %, v/v)	27 32 37	1.1 0.9 0.8
glycerol (50 %, v/v) D_2O (20 %, v/v) Buffer[b] (30 %, v/v)	27 32 37	8.4 7.4 5.9

[a] – density: 1.2907 g/ ml (at 27^{o}C); water content: 33000 ppm

[b] – 50 mM sodium phosphate buffer, pH 5.5

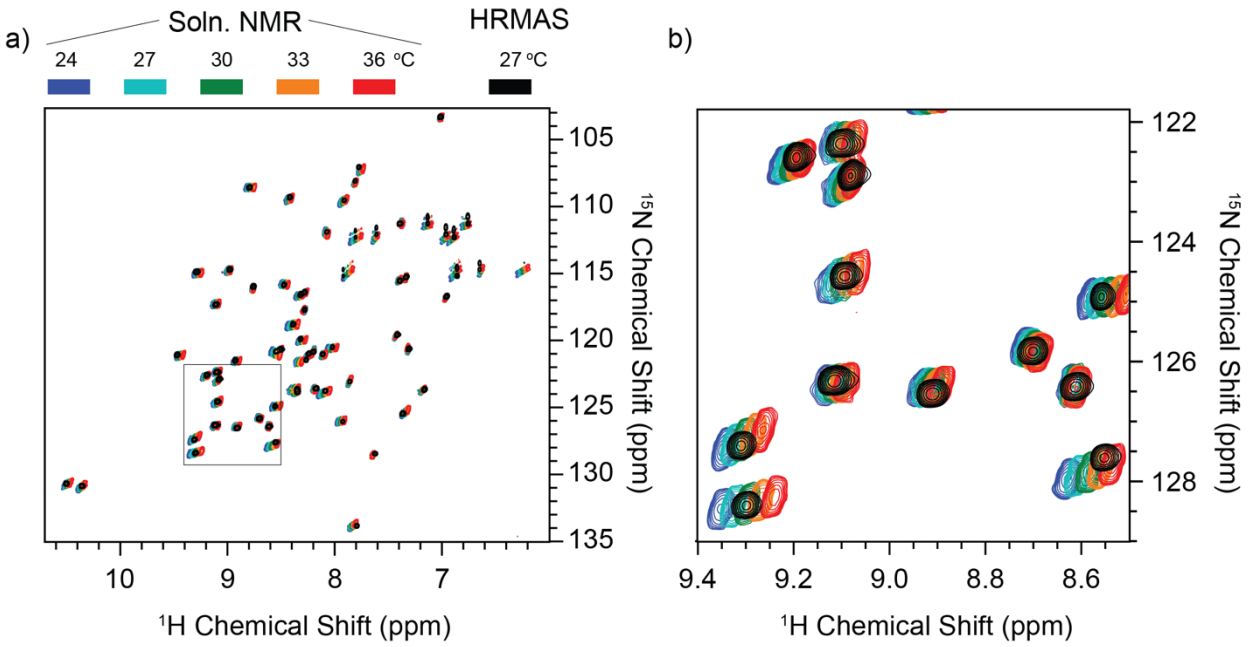

Figure S1. Temperature calibration of 2D ^{1}H-^{15}N HSQC HRMAS spectra of GB1. a) Solution NMR 2D ^{1}H-^{15}N HSQC spectra were acquired using a traditional solution NMR BBO probe at 24-36 °C and compared to an HRMAS spectrum acquired at 27 °C VT inlet gas temperature. b) The HRMAS GB1 spectrum best overlays with the traditional solution NMR spectra obtained at 30 °C (slightly shifted towards the 33 °C spectrum). Therefore, it is estimated that the true sample temperature of the GB1 sample under 5 kHz magic angle spinning is approximately 30-31 °C. All spectra were acquired on a 600 MHz Avance III Bruker NMR spectrometer.

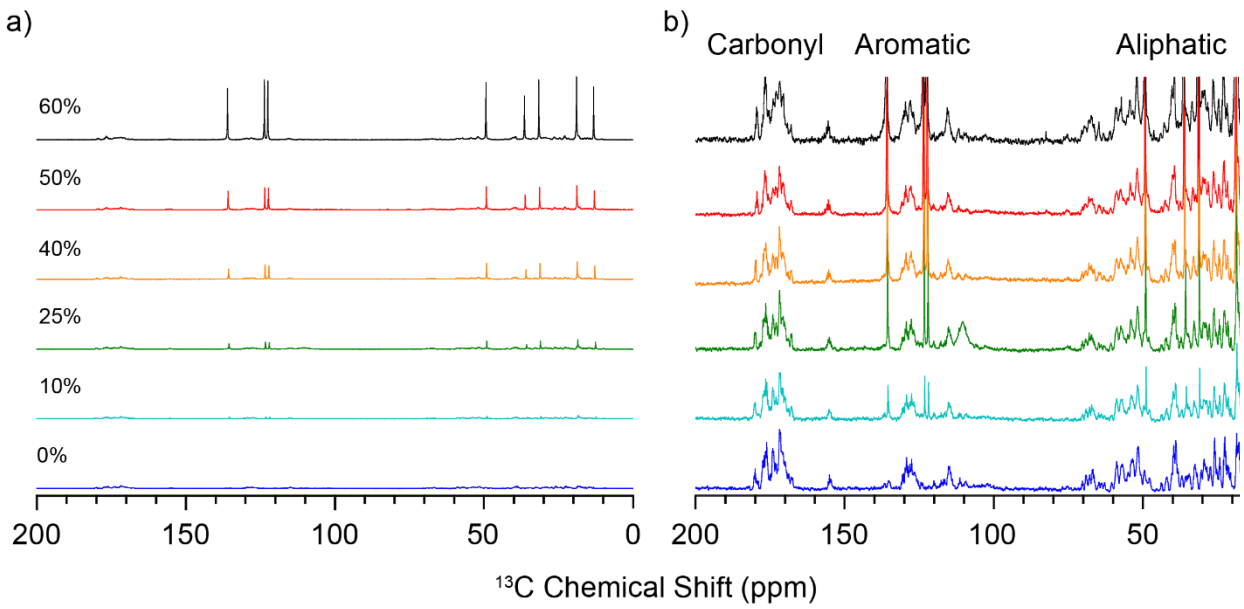

Fig. S2 1D ^{13}C HR-MAS spectra of GB1 in the presence of [C_4-mim]Br. a) GB1 with 0% (blue), 10% (cyan), 25% (green), 40% (orang), 50% (red), and 60% (black) v/v [C_4-mim]Br. The dominant peaks are assigned to [C_4-mim]Br. b) 1D ^{13}C enlarged views to show protein ^{13}C peaks. The [C_4-mim]Br peaks were cut in the ≥25% v/v [C_4-mim]Br spectra. The scaling factor was approximately 10 in panel b) relative spectra shown in panel a). The most obvious changes were observed in the carbonyl region of the GB1 spectrum in the presence of 60% v/v [C_4-mim]Br.

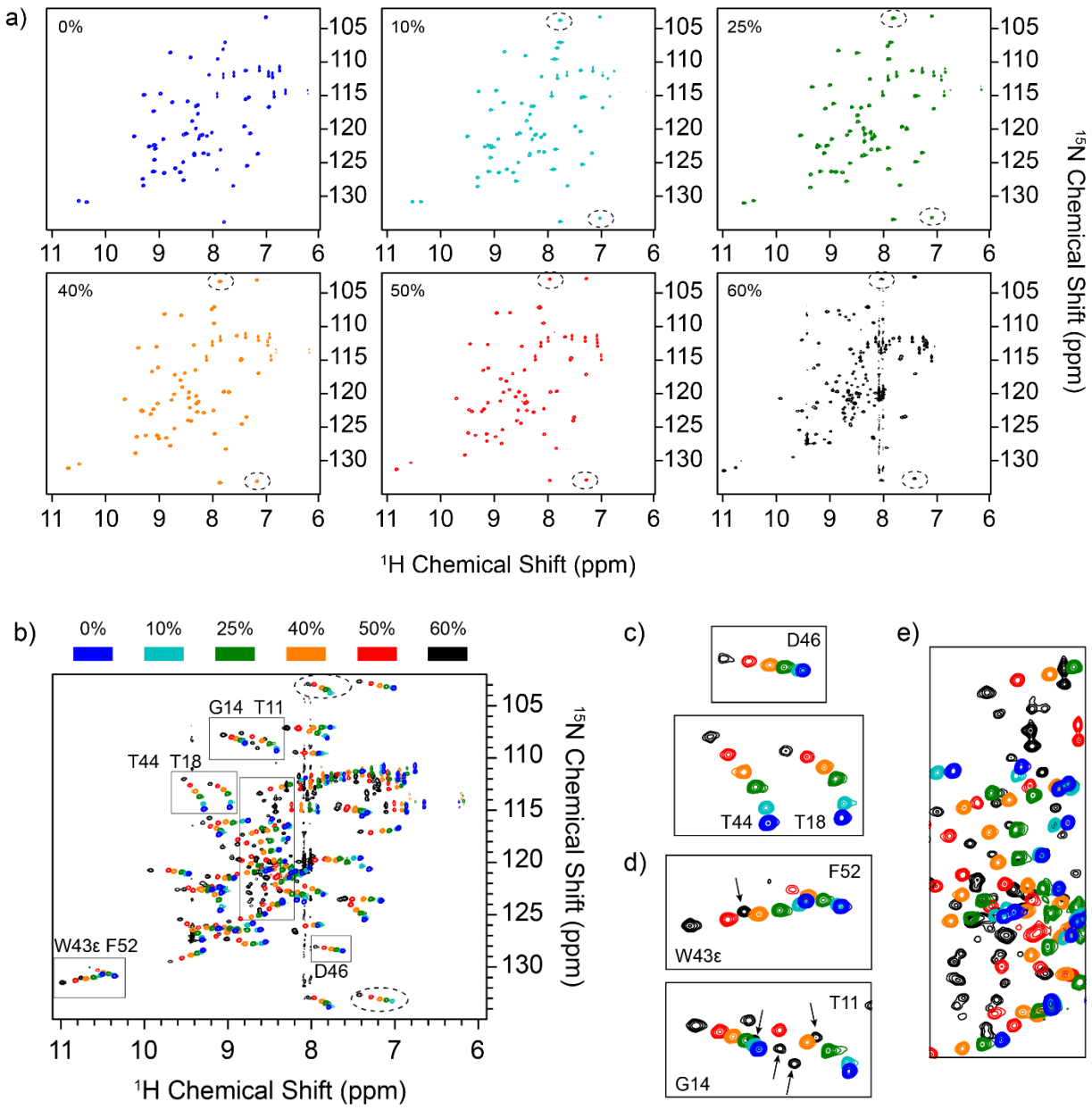

Figure S3. 2D ^{1}H-^{15}N HSQC spectra of GB1 in the presence of 0-60% v/v [C$_4$-mim]Br. a) Individual 2D ^{1}H-^{15}N HSQC spectra. b) Overlay of 2D ^{1}H-^{15}N HSQC spectra. c) Some peaks shifted more downfield in the 60% v/v [C$_4$-mim]Br spectrum as anticipated based on the observed trend. d) For some amino acids, additional peaks also appeared, as indicated by arrows. e) There was a notable increase of the number of the peaks in the 8.4-8.9 ppm ^{1}H region of the 60% v/v [C$_4$-mim]Br spectrum, which indicates random coil conformation. The data implies the coexistence of a folded state and an unfolded state of GB1 in the presence of 60% v/v [C$_4$-mim]Br. Aliased peaks are shown in dashed ovals.

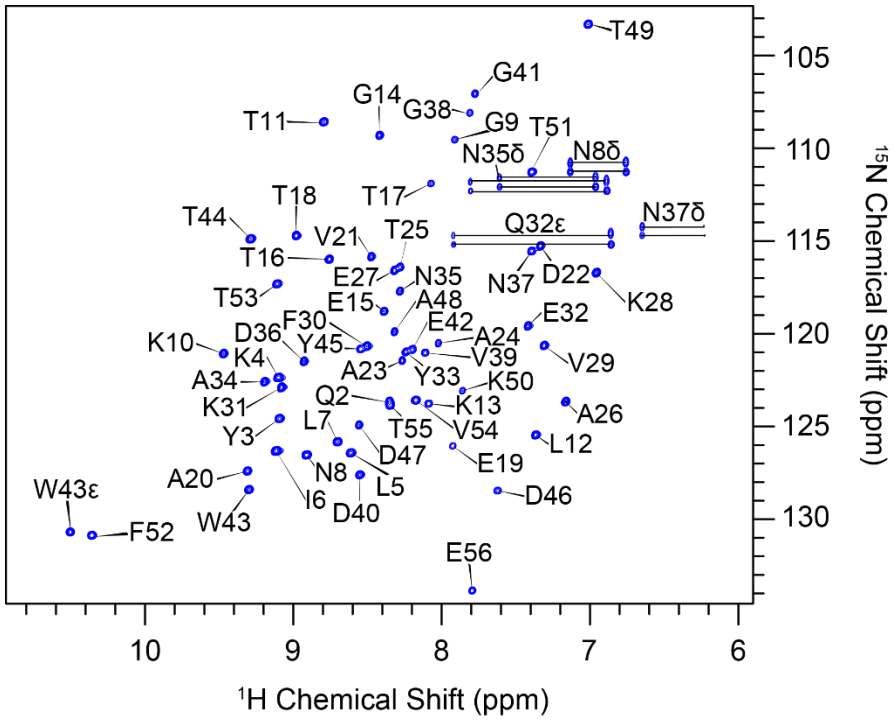

Fig. S4 Resonance assignments of 0% IL GB1 2D ^{1}H-^{15}N HSQC spectrum.

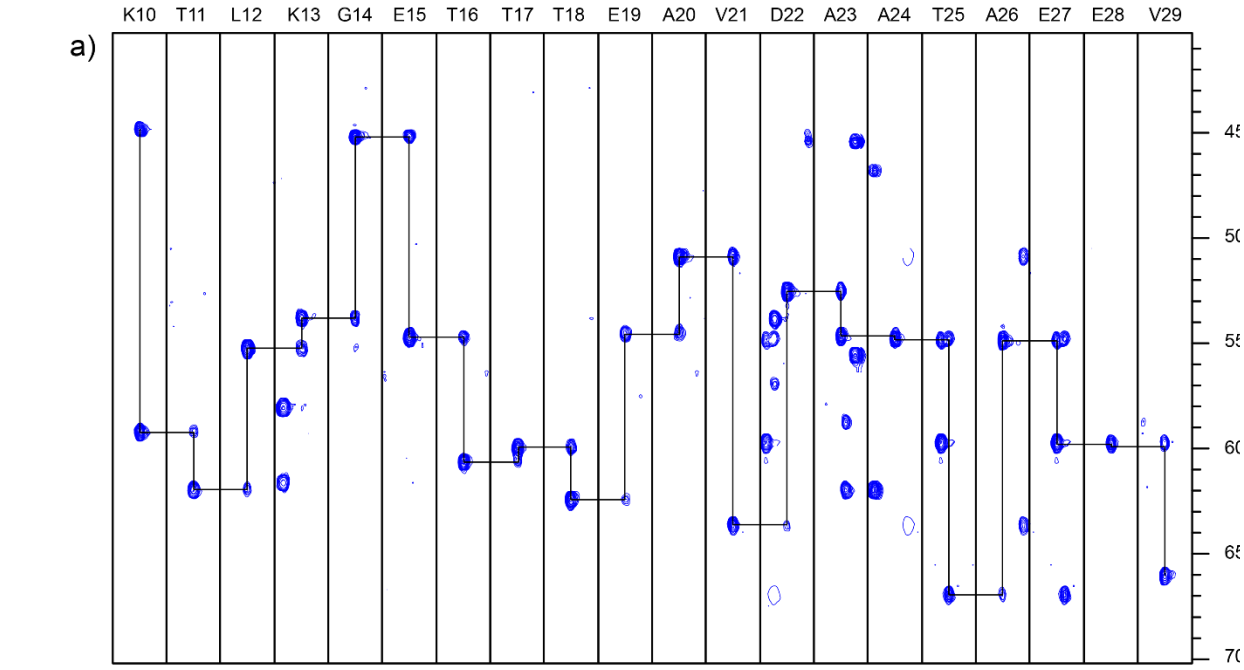
a)
K10 T11 L12 K13 G14 E15 T16 T17 T18 E19 A20 V21 D22 A23 A24 T25 A26 E27 E28 V29
^{1}H (ppm) 9.47 8.79 7.37 8.09 8.42 8.39 8.76 8.07 8.98 7.92 9.31 8.48 7.34 8.27 8.02 8.28 7.16 8.32 6.96 7.31
^{15}N (ppm) 121.0 108.5 125.4 123.7 109.3 118.7 115.9 111.9 114.7 126.0 127.4 115.8 115.2 121.4 120.5 116.4 123.6 116.5 116.7 120.6

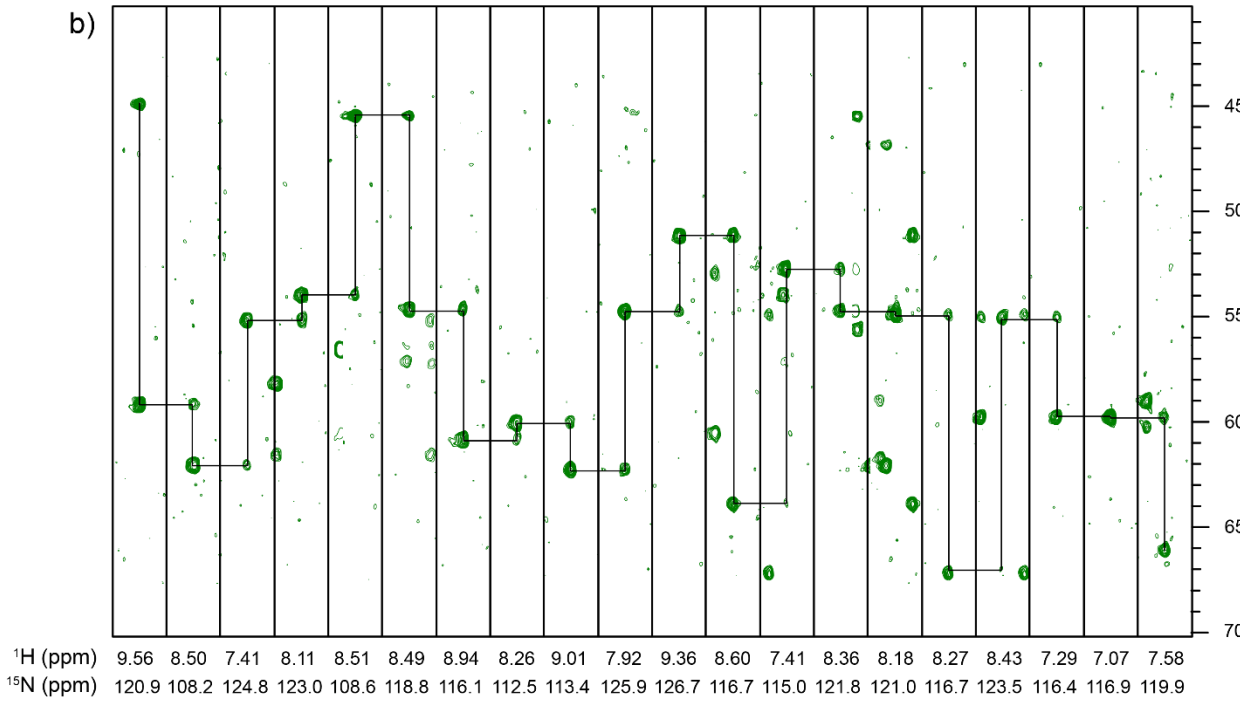
b)
^{1}H (ppm) 9.56 8.50 7.41 8.11 8.51 8.49 8.94 8.26 9.01 7.92 9.36 8.60 7.41 8.36 8.18 8.27 8.43 7.29 7.07 7.58
^{15}N (ppm) 120.9 108.2 124.8 123.0 108.6 118.8 116.1 112.5 113.4 125.9 126.7 116.7 115.0 121.8 121.0 116.7 123.5 116.4 116.9 119.9

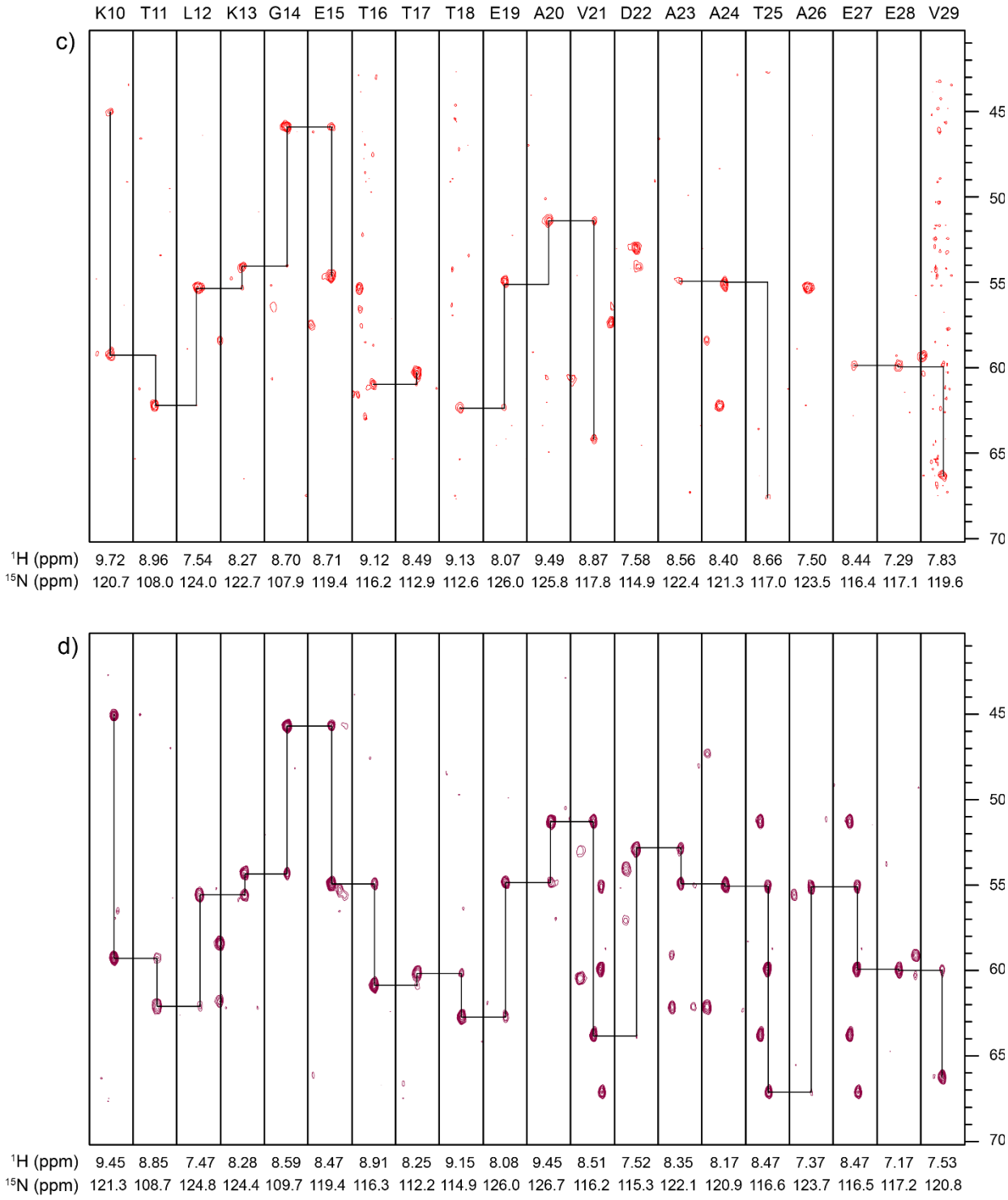

Fig. S5 Representative 3D HNCA strip plots of GB1 for residues K10-V29: a) aqueous solution (0% v/v [C_4-mim]Br), b) in 25% v/v [C_4-mim]Br, c) in 50% v/v [C_4-mim]Br, and d) in 2.29 M KBr. The Cα peaks of the *i* and *i*-1 residues are connected to guide the eye.

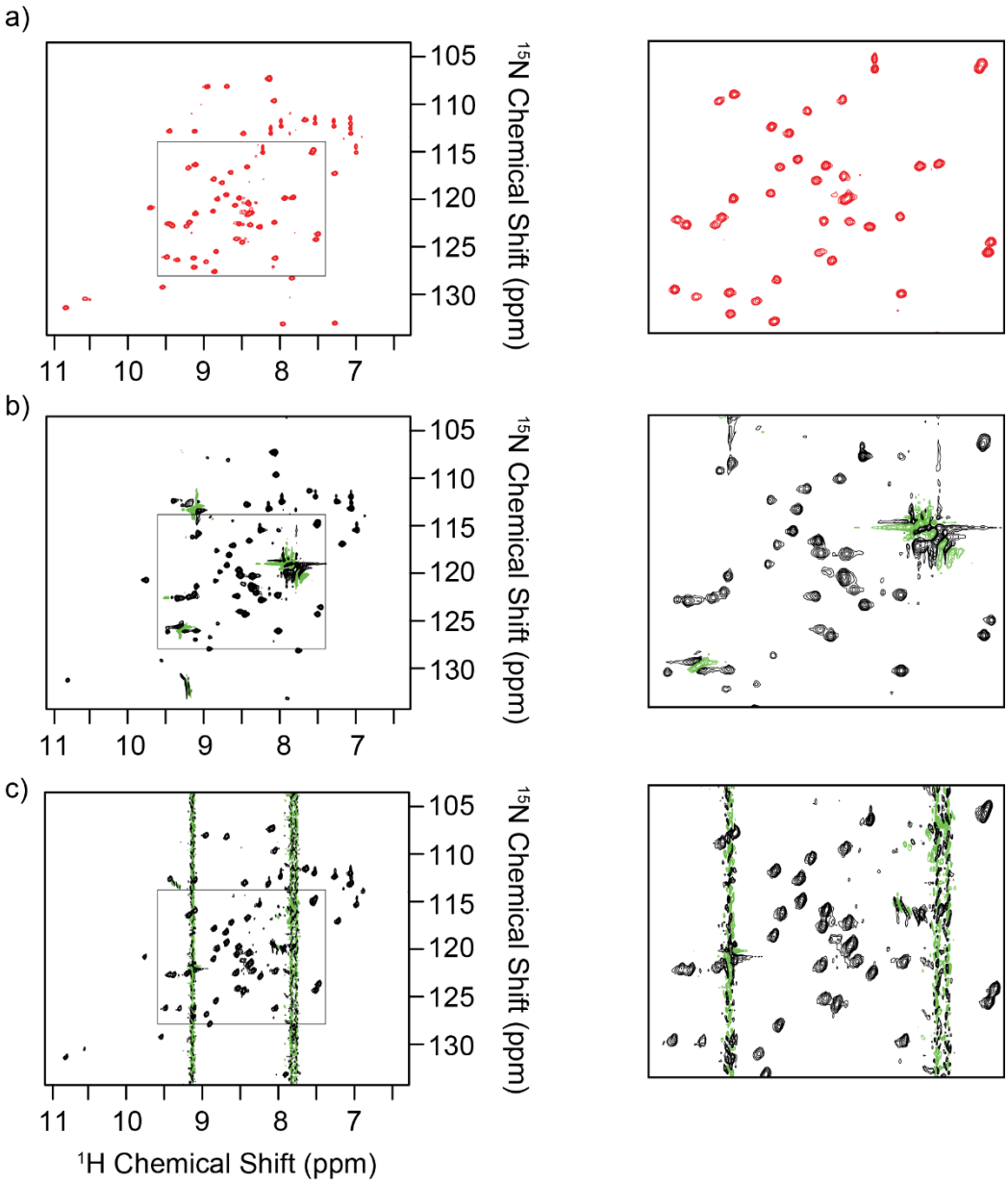

Figure S6. Comparison of 2D ^{1}H-^{15}N HSQC HRMAS vs. traditional solution NMR spectra of GB1 in the presence of 50% v/v [C_4-mim]Br. a) HRMAS 2D ^{1}H-^{15}N HSQC spectrum acquired on a 600 MHz Avance III Bruker NMR spectrometer. b) Solution NMR 2D ^{1}H-^{15}N HSQC spectrum acquired using a Cryoprobe on a 600 MHz Avance III Bruker NMR spectrometer. c) Solution NMR 2D ^{1}H-^{15}N HSQC spectrum acquired using a Cold probe on a VNMRS 900 MHz spectrometer. The expanded regions (in squares) are shown to the right.

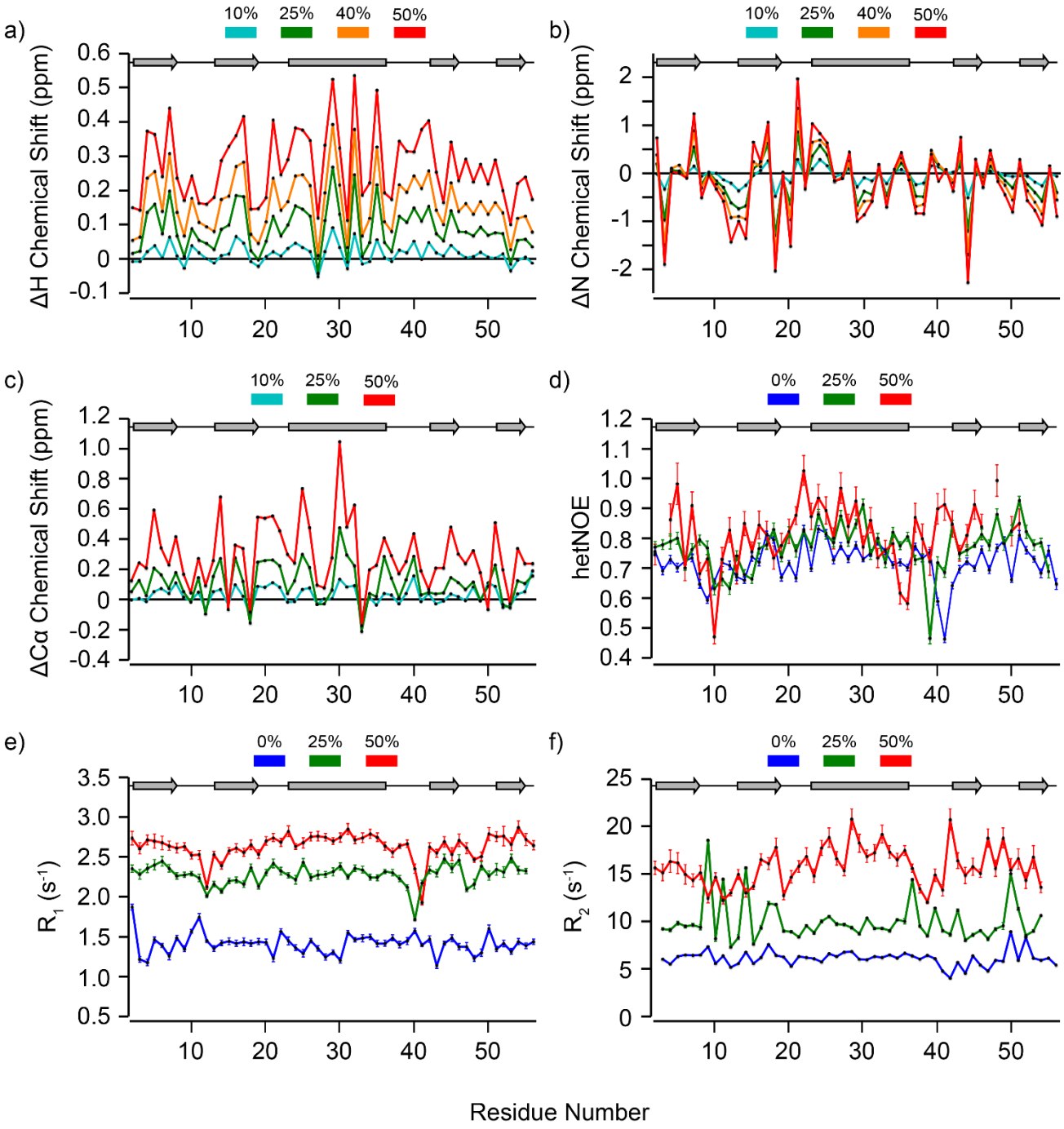

Fig. S7 Chemical shift perturbations and NMR relaxation data of all residues of GB1. a) ^{1}H chemical shift perturbations, ΔH. b) ^{15}N chemical shift perturbations, ΔN. c) ^{13}Cα chemical shift perturbations, ΔCα. d) hetNOE relaxation data e) R_1 calculated from Backbone ^{15}N spin relaxation T_1, f) R_2 calculated from Backbone ^{15}N spin relaxation T_2. In all diagrams, graphs are color coded according to the % [C$_4$-mim]Br present in solution: 0% (blue), 10% (cyan), 25% (green), 40% (orange), and 50% (red) v/v [C$_4$-mim]Br.

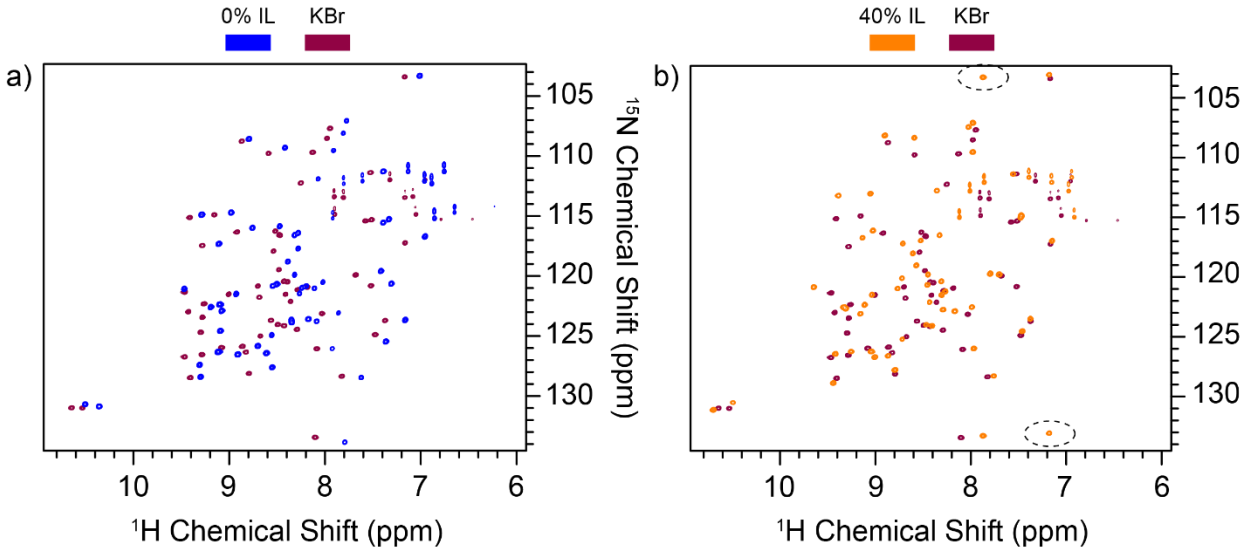

Fig. S8 The effect of KBr vs. [C_4-mim]Br on GB1. a) Overlay of 0% [C_4-mim]Br GB1 2D ^{1}H-^{15}N HSQC spectrum (blue) with spectrum of GB1 in the presence of 2.29 M KBr (maroon). b) Overlay of GB1 spectrum in the presence of 2.29 M KBr (maroon) and 40% v/v (2.36 M) [C_4-mim]Br. Aliased peaks are shown in dashed ovals.

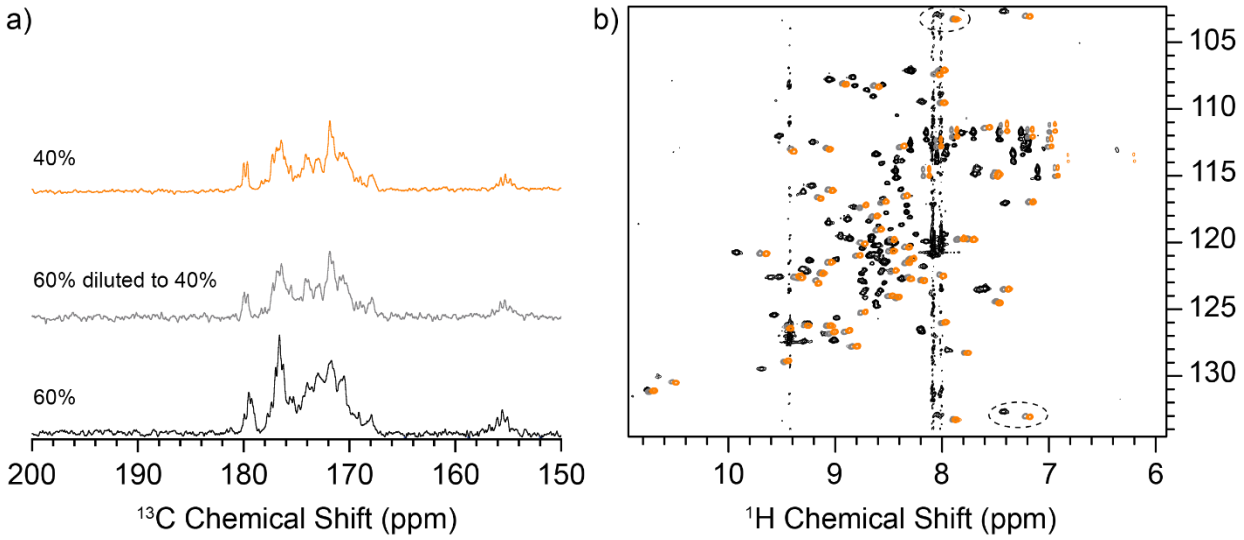

Fig. S9 GB1 unfolding in 60% v/v [C_4-mim]Br solution is reversible by dilution. a) Carbonyl region of 1D ^{13}C HR-MAS spectra of GB1 and b) overlay of 2D ^{1}H-^{15}N HSQC GB1 spectra in the presence of 40% v/v [C_4-mim]Br (orange), 60% v/v [C_4-mim]Br (black), and 40% v/v [C_4-mim]Br that was diluted from the 60% v/v [C_4-mim]Br sample by addition of the buffer (grey). GB1 in presence 60% v/v [C_4-mim]Br showed distinct changes in the 2D ^{1}H-^{15}N HSQC and in the ^{13}C 1D carbonyl region. Upon dilution of the 60% v/v [C_4-mim]Br sample with buffer, the spectrum overlaid almost perfectly with the 40% v/v [C_4-mim]Br spectrum. Aliased peaks are shown in dashed ovals.

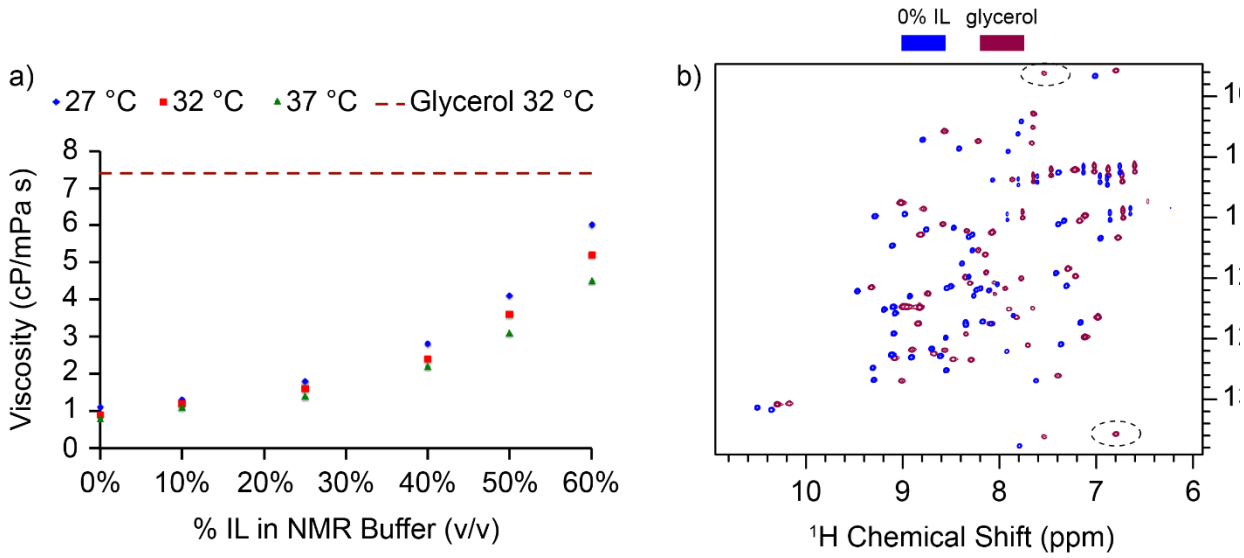

Fig. S10. The effect of viscosity. a) The viscosity of aqueous [C_4-mim]Br solutions (10%-60% v/v concentration) at 27 °C, 32 °C, and 37 °C (viscosity of 50% aqueous glycerol at 32 °C, indicated with a dashed red, line is given for comparison). b) Overlay of 0% IL GB1 2D ^{1}H-^{15}N HSQC spectrum (blue) with spectrum of GB1 in the presence of 50% glycerol (maroon). Aliased peaks are shown in dashed ovals.

REFERENCES

1 Drori, R., Celik, Y., Davies, P. L. & Braslavsky, I. Ice-binding proteins that accumulate on different ice crystal planes produce distinct thermal hysteresis dynamics. *Journal of the Royal Society, Interface / the Royal Society* **11**, 20140526 (2014).

2 Venketesh, S. & Dayananda, C. Properties, potentials, and prospects of antifreeze proteins. *Critical reviews in biotechnology* **28**, 57-82 (2008).

3 Bale, J. S. & Hayward, S. A. Insect overwintering in a changing climate. *The Journal of experimental biology* **213**, 980-994 (2010).

4 Clark, M. S. & Worland, M. R. How insects survive the cold: molecular mechanisms-a review. *Journal of comparative physiology. B, Biochemical, systemic, and environmental physiology* **178**, 917-933 (2008).

5 Doucet, D., Walker, V. K. & Qin, W. The bugs that came in from the cold: molecular adaptations to low temperatures in insects. *Cellular and molecular life sciences : CMLS* **66**, 1404-1418 (2009).

6 Amir, G. Preservation of myocyte structure and mitochondrial integrity in subzero cryopreservation of mammalian hearts for transplantation using antifreeze proteins—an electron microscopy study. *European Journal of Cardio-Thoracic Surgery* **24**, 292-297 (2003).

7 Amir, G., Rubinsky, B., Horowitz, L., Miller, L., Leor, J., Kassif, Y., Mishaly, D., Smolinsky, A. K. & Lavee, J. Prolonged 24-hour subzero preservation of heterotopically transplanted rat hearts using antifreeze proteins derived from arctic fish. *The Annals of thoracic surgery* **77**, 1648-1655 (2004).

8 Griffith, M. & Yaish, M. W. Antifreeze proteins in overwintering plants: a tale of two activities. *Trends in plant science* **9**, 399-405 (2004).

9 Brockbank, K. G., Campbell, L. H., Greene, E. D., Brockbank, M. C. & Duman, J. G. Lessons from nature for preservation of mammalian cells, tissues, and organs. *In vitro cellular & developmental biology. Animal* **47**, 210-217 (2011).

10 Tomczak, M. M., Hincha, D. K., Estrada, S. D., Wolkers, W. F., Crowe, L. M., Feeney, R. E., Tablin, F. & Crowe, J. H. A Mechanism for Stabilization of Membranes at Low Temperatures by an Antifreeze protein. *Biophysical journal* **82**, 874-881 (2002).

11 Devries, A. L. & Wohlschlag, D. E. Freezing resistance in some antarctic fishes. *Science* **163**, 1073-+ (1969).

12 Marshall, C. B., Chakrabartty, A. & Davies, P. L. Hyperactive antifreeze protein from winter flounder is a very long rod-like dimer of alpha-helices. *The Journal of biological chemistry* **280**, 17920-17929 (2005).

13 Zhang, W. Structure-function relationships in a type I antifreeze polypeptide: the role of threonine methyl and hydroxyl groups in antifreeze activity. *Journal of Biological Chemistry* **273**, 34806-34812 (1998).

14 Graether, S. P. in *Biochemistry and Function of Antifreeze Proteins* (ed Vladimir N. Uversky) 221 (Nova Science Publishers, Inc., New York, 2010).

15 Kajava, A. V. Tandem repeats in proteins: from sequence to structure. *Journal of structural biology* **179**, 279-288 (2012).

16 Kwan, A. H. Y., Fairley, K., Anderberg, P. I., Liew, C. W., Harding, M. M. & Mackay, J. P. Solution structure of a recombinant type I sculpin antifreeze protein. *Biochemistry* **44**, 1980-1988 (2005).
17 Nishimiya, Y., Kondo, H., Takamichi, M., Sugimoto, H., Suzuki, M., Miura, A. & Tsuda, S. Crystal structure and mutational analysis of Ca2+-independent type II antifreeze protein from longsnout poacher, Brachyopsis rostratus. *Journal of Molecular Biology* **382**, 734-746 (2008).
18 Ko, T. P., Robinson, H., Gao, Y. G., Cheng, C. H. C., DeVries, A. L. & Wang, A. H. J. The refined crystal structure of an eel pout type III antifreeze protein RD1 at 0.62-A resolution reveals structural microheterogeneity of protein and solvation. *Biophysical journal* **84**, 1228-1237 (2003).
19 Gronwald, W., Loewen, M. C., Lix, B., Daugulis, A. J., Sonnichsen, F. D., Davies, P. L. & Sykes, B. D. The solution structure of type II antifreeze protein reveals a new member of the lectin family. *Biochemistry* **37**, 4712-4721 (1998).
20 Siemer, A. B. & McDermott, A. E. Solid-state NMR on a type III antifreeze protein in the presence of ice. *Journal of the American Chemical Society* **130**, 17394-17399 (2008).
21 Siemer, A. B., Huang, K. Y. & McDermott, A. E. Protein-ice interaction of an antifreeze protein observed with solid-state NMR. *Proceedings of the National Academy of Sciences of the United States of America* **107**, 17580-17585 (2010).
22 Lee, J. K., Kim, Y. J., Park, K. S., Shin, S. C., Kim, H. J., Song, Y. H. & Park, H. Molecular and comparative analyses of type IV antifreeze proteins (AFPIVs) from two Antarctic fishes, Pleuragramma antarcticum and Notothenia coriiceps. *Comp. Biochem. Physiol. B-Biochem. Mol. Biol.* **159**, 197-205 (2011).
23 Walters, K. R., Jr., Serianni, A. S., Voituron, Y., Sformo, T., Barnes, B. M. & Duman, J. G. A thermal hysteresis-producing xylomannan glycolipid antifreeze associated with cold tolerance is found in diverse taxa. *Journal of comparative physiology. B, Biochemical, systemic, and environmental physiology* **181**, 631-640 (2011).
24 Li, J. Q., Ma, W. J. & Ma, J. HEAT INDUCIBLE EXPRESSION OF ANTIFREEZE PROTEIN GENES FROM THE BEETLES Tenebrio molitor AND Microdera punctipennis. *CryoLetters* **37**, 10-18 (2016).
25 Liou, Y. C., Daley, M. E., Graham, L. A., Kay, C. M., Walker, V. K., Sykes, B. D. & Davies, P. L. Folding and structural characterization of highly disulfide-bonded beetle antifreeze protein produced in bacteria. *Protein expression and purification* **19**, 148-157 (2000).
26 Midya, U. S. & Bandyopadhyay, S. Hydration Behavior at the Ice-Binding Surface of the Tenebrio molitor Antifreeze Protein. *J. Phys. Chem. B* **118**, 4743-4752 (2014).
27 Bar Dolev, M., Braslavsky, I. & Davies, P. L. in *Annual Review of Biochemistry, Vol 85* Vol. 85 *Annual Review of Biochemistry* (ed R. D. Kornberg) 515-542 (Annual Reviews, 2016).
28 Davies, P. L., Baardsnes, J., Kuiper, M. J. & Walker, V. K. Structure and function of antifreeze proteins. *Philosophical transactions of the Royal Society of London. Series B, Biological sciences* **357**, 927-935 (2002).

29 Zhang, D. Q., Liu, B., Feng, D. R., He, Y. M. & Wang, J. F. Expression, purification, and antifreeze activity of carrot antifreeze protein and its mutants. *Protein expression and purification* **35**, 257-263 (2004).
30 Walters, K. R., Jr., Pan, Q., Serianni, A. S. & Duman, J. G. Cryoprotectant biosynthesis and the selective accumulation of threitol in the freeze-tolerant Alaskan beetle, Upis ceramboides. *The Journal of biological chemistry* **284**, 16822-16831 (2009).
31 Jia, Z. C. & Davies, P. L. Antifreeze proteins: an unusual receptor-ligand interaction. *Trends in Biochemical Sciences* **27**, 101-106 (2002).
32 Scotter, A. J., Marshall, C. B., Graham, L. A., Gilbert, J. A., Garnham, C. P. & Davies, P. L. The basis for hyperactivity of antifreeze proteins. *Cryobiology* **53**, 229-239 (2006).
33 Celik, Y., Graham, L. A., Mok, Y. F., Bar, M., Davies, P. L. & Braslavsky, I. Superheating of ice crystals in antifreeze protein solutions. *Proceedings of the National Academy of Sciences of the United States of America* **107**, 5423-5428 (2010).
34 Pertaya, N., Marshall, C. B., Celik, Y., Davies, P. L. & Braslavsky, I. Direct visualization of spruce budworm antifreeze protein interacting with ice crystals: basal plane affinity confers hyperactivity. *Biophysical journal* **95**, 333-341 (2008).
35 Mao, X., Liu, Z., Ma, J., Pang, H. & Zhang, F. Characterization of a novel beta-helix antifreeze protein from the desert beetle Anatolica polita. *Cryobiology* **62**, 91-99 (2011).
36 Wang, Y., Qiu, L., Dai, C., Wang, J., Luo, J., Zhang, F. & Ma, J. Expression of insect (Microdera puntipennis dzungarica) antifreeze protein MpAFP149 confers the cold tolerance to transgenic tobacco. *Plant cell reports* **27**, 1349-1358 (2008).
37 Marchand, P. J. *Life in the Cold: An Introduction to Winter Ecology*. 3rd edn, (University Press of New England, 1996).
38 Chao, H. M., Houston, M. E., Hodges, R. S., Kay, C. M., Sykes, B. D., Loewen, M. C., Davies, P. L. & Sonnichsen, F. D. A diminished role for hydrogen bonds in antifreeze protein binding to ice. *Biochemistry* **36**, 14652-14660 (1997).
39 Haymet, A. D. J., Ward, L. G., Harding, M. M. & Knight, C. A. Valine substituted winter flounder 'antifreeze': preservation of ice growth hysteresis. *Febs Letters* **430**, 301-306 (1998).
40 Garnham, C. P., Campbell, R. L. & Davies, P. L. Anchored clathrate waters bind antifreeze proteins to ice. *Proceedings of the National Academy of Sciences of the United States of America* **108**, 7363-7367 (2011).
41 Sun, T. J., Lin, F. H., Campbell, R. L., Allingham, J. S. & Davies, P. L. An Antifreeze Protein Folds with an Interior Network of More Than 400 Semi-Clathrate Waters. *Science* **343**, 795-798 (2014).
42 Ma, J., Wang, J., Mao, X. F. & Wang, Y. Differential expression of two antifreeze proteins in the desert beetle Anatolica polita (coleoptera: tenebriondae): seasonal variation and environmental effects. *CryoLetters* **33**, 337-348 (2012).
43 Mao, X., Liu, Z., Li, H., Ma, J. & Zhang, F. Calorimetric studies on an insect antifreeze protein ApAFP752 from Anatolica polita. *Journal of Thermal Analysis and Calorimetry* **104**, 343-349 (2010).

44 Liu, Z. Y., Li, H. L., Pang, H., Ma, J. & Mao, X. F. Enhancement effect of solutes of low molecular mass on the insect antifreeze protein ApAFP752 from Anatolica polita. *Journal of Thermal Analysis and Calorimetry* **120**, 307-315 (2015).
45 Wallace, B. J. & Kushner, S. R. Genetic and physical analysis of the thioredoxin (TrxA) gene of Escherichia-coli K-12. *Gene* **32**, 399-408 (1984).
46 Kratochvilova, I., Golan, M., Pomeisl, K., Richter, J., Sedlakova, S., Sebera, J., Micova, J., Falk, M., Falkova, I., Reha, D., Elliott, K. W., Varga, K., Follett, S. E. & Simek, D. Theoretical and experimental study of the antifreeze protein AFP752, trehalose and dimethyl sulfoxide cryoprotection mechanism: correlation with cryopreserved cell viability. *RSC Adv.* **7**, 352-360 (2017).
47 Beaven, G. H. & Holiday, E. R. Ultraviolet Absorption Spectra of Proteins and Amino Acids. *Adv.Protein Chem.* **7**, 319-386 (1952).
48 Gasteiger, E., Hoogland, C., Gattiker, A., Duvaud, S., Wilkins, M. R., Appel, R. D. & Bairoch, A. in *The Proteomics Protocols Handbook* (ed J.M. Walker) Ch. 52, 571-607 (Hamana Press, 2005).
49 Wishart, D. S., Bigam, C. G., Yao, J., Abildgaard, F., Dyson, H. J., Oldfield, E., Markley, J. L. & Sykes, B. D. 1H, 13C and 15N chemical shift referencing in biomolecular NMR. *Journal of biomolecular NMR* **6**, 135-140 (1995).
50 Marley, J., Lu, M. & Bracken, C. A method for efficient isotopic labeling of recombinant proteins. *Journal of biomolecular NMR* **20**, 71-75 (2001).
51 Zeng-Elmore, X., Gao, X. Z., Pellarin, R., Schneidman-Duhovny, D., Zhang, X. J., Kozacka, K. A., Tang, Y., Sali, A., Chalkley, R. J., Cote, R. H. & Chu, F. Molecular architecture of photoreceptor phosphodiesterase elucidated by chemical cross-linking and integrative modeling. *J Mol Biol* **426**, 3713-3728 (2014).
52 Amornwittawat, N., Wang, S., Banatlao, J., Chung, M., Velasco, E., Duman, J. G. & Wen, X. Effects of polyhydroxy compounds on beetle antifreeze protein activity. *Biochimica et biophysica acta* **1794**, 341-346 (2009).
53 Liu, Z. H., Muldrew, K., Wan, R. G. & Elliott, J. A. W. Measurement of freezing point depression of water in glass capillaries and the associated ice front shape. *Phys. Rev. E* **67**, 9 (2003).
54 Lin, X., Wisniewski, M. E. & Duman, J. G. Expression of Two Self-enhancing Antifreeze Proteins from the Beetle Dendroides canadensis in Arabidopsis thaliana. *Plant Mol. Biol. Rep.* **29**, 802-813 (2011).
55 Duman, J. G. & Wisniewski, M. J. The use of antifreeze proteins for frost protection in sensitive crop plants. *Environ. Exp. Bot.* **106**, 60-69 (2014).
56 Rubinsky, L., Raichman, N., Lavee, J., Frenk, H., Ben-Jacob, E. & Bickler, P. E. Antifreeze protein suppresses spontaneous neural activity and protects neurons from hypothermia/re-warming injury. *Neuroscience research* **67**, 256-259 (2010).
57 Yeh, C. M., Kao, B. Y. & Peng, H. J. Production of a recombinant type 1 antifreeze protein analogue by L. lactis and its applications on frozen meat and frozen dough. *Journal of agricultural and food chemistry* **57**, 6216-6223 (2009).
58 Wheeler, G. N. & Brändli, A. W. Simple vertebrate models for chemical genetics and drug discovery screens: Lessons from zebrafish and Xenopus. *Developmental Dynamics* **238**, 1287-1308 (2009).

59 Guenther, J. F., Seki, S., Kleinhans, F. W., Edashige, K., Roberts, D. M. & Mazur, P. Extra- and intra-cellular ice formation in Stage I and II Xenopus laevis oocytes. *Cryobiology* **52**, 401-416 (2006).
60 Kleinhans, F. W., Guenther, J. F., Roberts, D. M. & Mazur, P. Analysis of intracellular ice nucleation in Xenopus oocytes by differential scanning calorimetry. *Cryobiology* **52**, 128-138 (2006).
61 Yamaji, Y., Valdez, D. M., Seki, S., Yazawa, K. I., Urakawa, C., Jin, B., Kasai, M., Kleinhans, F. W. & Edashige, K. Cryoprotectant permeability of aquaporin-3 expressed in Xenopus oocytes. *Cryobiology* **53**, 258-267 (2006).
62 Edens, L. J. & Levy, D. L. cPKC regulates interphase nuclear size during Xenopus development. *J Cell Biol* **206**, 473-483 (2014).
63 Gillespie, P. J., Gambus, A. & Blow, J. J. Preparation and use of Xenopus egg extracts to study DNA replication and chromatin associated proteins. *Methods* **57**, 203-213 (2012).
64 Tokmakov, A. A., Iguchi, S., Iwasaki, T. & Fukami, Y. Unfertilized frog eggs die by apoptosis following meiotic exit. *Bmc Cell Biology* **12** (2011).
65 Iguchi, S., Iwasaki, T., Fukami, Y. & Tokmakov, A. A. Unlaid Xenopus eggs degrade by apoptosis in the genital tract. *Bmc Cell Biology* **14** (2013).
66 Johnson, C. E., Freel, C. D. & Kornbluth, S. Features of programmed cell death in intact Xenopus oocytes and early embryos revealed by near-infrared fluorescence and real-time monitoring. *Cell Death and Differentiation* **17**, 170-179 (2010).
67 Du Pasquier, D., Dupre, A. & Jessus, C. Unfertilized Xenopus Eggs Die by Bad-Dependent Apoptosis under the Control of Cdk1 and JNK. *Plos One* **6** (2011).
68 Willis, J., DeStephanis, D., Patel, Y., Gowda, V. & Yan, S. Study of the DNA Damage Checkpoint using Xenopus Egg Extracts. *Jove-Journal of Visualized Experiments* (2012).
69 Broadus, M. R., Yew, P. R., Hann, S. R. & Lee, E. in *Chemical Biology: Methods and Protocols* Vol. 1263 *Methods in Molecular Biology* (eds J. E. Hempel, C. H. Williams, & C. C. Hong) 63-73 (2015).
70 Dong, J. P., Malsam, J., Bischof, J. C., Hubel, A. & Aksan, A. Spatial Distribution of the State of Water in Frozen Mammalian Cells. *Biophysical journal* **99**, 2453-2459 (2010).
71 Hong, J., Hu, Y., Li, C., Jia, Z., Xia, B. & Jin, C. NMR characterizations of the ice binding surface of an antifreeze protein. *PloS one* **5**, e15682 (2010).
72 Garner, J., Inglis, S. R., Hook, J., Separovic, F. & Harding, M. M. A solid-state NMR study of the interaction of fish antifreeze proteins with phospholipid membranes. *European biophysics journal : EBJ* **37**, 1031-1038 (2008).
73 Inglis, S. R., McGann, M. J., Price, W. S. & Harding, M. M. Diffusion NMR studies on fish antifreeze proteins and synthetic analogues. *FEBS Lett* **580**, 3911-3915 (2006).
74 Li, C., Guo, X., Jia, Z., Xia, B. & Jin, C. Solution structure of an antifreeze protein CfAFP-501 from Choristoneura fumiferana. *Journal of biomolecular NMR* **32**, 251-256 (2005).

75 Berman, H. M., Westbrook, J., Feng, Z., Gilliland, G., Bhat, T. N., Weissig, H., Shindyalov, I. N. & Bourne, P. E. The Protein Data Bank. *Nucleic Acids Res.* **28**, 235-242 (2000).
76 Delaglio, F., Grzesiek, S., Vuister, G. W., Zhu, G., Pfeifer, J. & Bax, A. NMRPipe - A Multidimensional Spectral Processing System Based on UNIX Pipes. *Journal of biomolecular NMR* **6**, 277-293 (1995).
77 Lee, W., Tonelli, M. & Markley, J. L. NMRFAM-SPARKY: enhanced software for biomolecular NMR spectroscopy. *Bioinformatics* **31**, 1325-1327 (2015).
78 Lee, W., Tonelli, M., Dashti, H., Eghbalnia, H. & Markley, J. L. *I-Pine, An Integrative Probabilistic NMR assignment system* (National Magnetic Resonance Facility at Madison).
79 Wang, Y. J. & Jardetzky, O. Probability-based protein secondary structure identification using combined NMR chemical-shift data. *Protein Sci.* **11**, 852-861 (2002).
80 Shen, Y., Lange, O., Delaglio, F., Rossi, P., Aramini, J. M., Liu, G. H., Eletsky, A., Wu, Y. B., Singarapu, K. K., Lemak, A., Ignatchenko, A., Arrowsmith, C. H., Szyperski, T., Montelione, G. T., Baker, D. & Bax, A. Consistent blind protein structure generation from NMR chemical shift data. *Proceedings of the National Academy of Sciences of the United States of America* **105**, 4685-4690 (2008).
81 Shen, Y., Vernon, R., Baker, D. & Bax, A. De novo protein structure generation from incomplete chemical shift assignments. *Journal of biomolecular NMR* **43**, 63-78 (2009).
82 Eghbalnia, H. R., Wang, L. Y., Bahrami, A., Assadi, A. & Markley, J. L. Protein energetic conformational analysis from NMR chemical shifts (PECAN) and its use in determining secondary structural elements. *Journal of biomolecular NMR* **32**, 71-81 (2005).
83 McMahon, B. & Hanson, R. M. A toolkit for publishing enhanced figures. *J. Appl. Crystallogr.* **41**, 811-814 (2008).
84 Ding, K. Y., Louis, J. M. & Gronenborn, A. M. Insights into conformation and dynamics of protein GB1 during folding and unfolding by NMR. *Journal of Molecular Biology* **335**, 1299-1307 (2004).
85 Mielke, S. P. & Krishnan, V. V. Characterization of protein secondary structure from NMR chemical shifts. *Progress in Nuclear Magnetic Resonance Spectroscopy* **54**, 141-165 (2009).
86 Rovo, P., Straner, P., Lang, A., Bartha, I., Huszar, K., Nyitray, L. & Perczel, A. Structural Insights into the Trp-Cage Folding Intermediate Formation. *Chemistry-a European Journal* **19**, 2628-2640 (2013).
87 Hong, J. B., Jing, Q. Q. & Yao, L. S. The protein amide H-1(N) chemical shift temperature coefficient reflects thermal expansion of the N-H center dot center dot center dot O=C hydrogen bond. *Journal of biomolecular NMR* **55**, 71-78 (2013).
88 Hallett, J. P. & Welton, T. Room-Temperature Ionic Liquids: Solvents for Synthesis and Catalysis. 2. *Chem. Rev.* **111**, 3508-3576 (2011).
89 van Rantwijk, F. & Sheldon, R. A. Biocatalysis in ionic liquids. *Chem. Rev.* **107**, 2757-2785 (2007).

90 Santos, E., Albo, J. & Irabien, A. Magnetic ionic liquids: synthesis, properties and applications. *RSC Adv.* **4**, 40008-40018 (2014).
91 Neouze, M. A., Kronstein, M. & Tielens, F. Ionic nanoparticle networks: development and perspectives in the landscape of ionic liquid based materials. *Chem. Commun.* **50**, 10929-10936 (2014).
92 Ma, M. G., Zhu, J. F., Zhu, Y. J. & Sun, R. C. The Microwave-Assisted Ionic-Liquid Method: A Promising Methodology in Nanomaterials. *Chem-Asian J.* **9**, 2378-2391 (2014).
93 Gebresilassie Eshetu, G., Armand, M., Scrosati, B. & Passerini, S. Energy Storage Materials Synthesized from Ionic Liquids. *Angew. Chem. Int. Edit.* **53**, 13342-13359 (2014).
94 Kar, M., Simons, T. J., Forsyth, M. & MacFarlane, D. R. Ionic liquid electrolytes as a platform for rechargeable metal-air batteries: a perspective. *Phys. Chem. Chem. Phys.* **16**, 18658-18674 (2014).
95 MacFarlane, D. R., Tachikawa, N., Forsyth, M., Pringle, J. M., Howlett, P. C., Elliott, G. D., Davis, J. H., Watanabe, M., Simon, P. & Angell, C. A. Energy applications of ionic liquids. *Energ. Environ. Sci.* **7**, 232-250 (2014).
96 Medina-Gonzalez, Y., Camy, S. & Condoret, J.-S. ScCO2/Green Solvents: Biphasic Promising Systems for Cleaner Chemicals Manufacturing. *ACS Sustain. Chem. Eng.* **2**, 2623-2636 (2014).
97 Abro, R., Abdeltawab, A. A., Al-Deyab, S. S., Yu, G., Qazi, A. B., Gao, S. & Chen, X. A review of extractive desulfurization of fuel oils using ionic liquids. *RSC Adv.* **4**, 35302-35317 (2014).
98 Cevasco, G. & Chiappe, C. Are ionic liquids a proper solution to current environmental challenges? *Green Chem.* **16**, 2375-2385 (2014).
99 Kapnissi-Christodoulou, C. P., Stavrou, I. J. & Mavroudi, M. C. Chiral ionic liquids in chromatographic and electrophoretic separations. *J. Chromatogr. A* **1363**, 2-10 (2014).
100 Payagala, T. & Armstrong, D. W. Chiral ionic liquids: A compendium of syntheses and applications (2005–2012). *Chirality* **24**, 17-53 (2012).
101 Jameson, L. P., Kimball, J. D., Gryczynski, Z., Balaz, M. & Dzyuba, S. V. Effect of ionic liquids on the conformation of a porphyrin-based viscometer. *RSC Adv.* **3**, 18300-18304 (2013).
102 Jameson, L. P. & Dzyuba, S. V. Ionic liquid-controlled conformational bias of tetracycline. *RSC Advances* **3**, 4582-4587 (2013).
103 Jameson, L. P. & Dzyuba, S. V. Circular Dichroism Studies on Intermolecular Interactions of Amphotericin B in Ionic Liquid-Rich Environments. *Chirality* **25**, 427-432 (2013).
104 Byrne, N., Wang, L.-M., Belieres, J.-P. & Angell, C. A. Reversible folding-unfolding, aggregation protection, and multi-year stabilization, in high concentration protein solutions, using ionic liquids. *Chem. Commun.*, 2714-2716 (2007).
105 Bihari, M., Russell, T. P. & Hoagland, D. A. Dissolution and Dissolved State of Cytochrome c in a Neat, Hydrophilic Ionic Liquid. *Biomacromolecules* **11**, 2944-2948 (2010).

106 Baker, G. A. & Heller, W. T. Small-angle neutron scattering studies of model protein denaturation in aqueous solutions of the ionic liquid 1-butyl-3-methylimidazolium chloride. *Chem. Eng. J.* **147**, 6-12 (2009).
107 Bharmoria, P., Trivedi, T. J., Pabbathi, A., Samanta, A. & Kumar, A. Ionic liquid-induced all-[small alpha] to [small alpha] + [small beta] conformational transition in cytochrome c with improved peroxidase activity in aqueous medium. *Phys. Chem. Chem. Phys.* **17**, 10189-10199 (2015).
108 Constantinescu, D., Weingärtner, H. & Herrmann, C. Protein Denaturation by Ionic Liquids and the Hofmeister Series: A Case Study of Aqueous Solutions of Ribonuclease A. *Angew. Chem. Int. Edit.* **46**, 8887-8889 (2007).
109 Lai, J.-Q., Li, Z., Lu, Y.-H. & Yang, Z. Specific ion effects of ionic liquids on enzyme activity and stability. *Green Chem.* **13**, 1860-1868 (2011).
110 Yang, Z., Yue, Y.-J., Huang, W.-C., Zhuang, X.-M., Chen, Z.-T. & Xing, M. Importance of the Ionic Nature of Ionic Liquids in Affecting Enzyme Performance. *J. Biochem. (Tokyo).* **145**, 355-364 (2009).
111 Kumar, A. & Venkatesu, P. Does the stability of proteins in ionic liquids obey the Hofmeister series? *Int. J. Biol. Macromol.* **63**, 244-253 (2014).
112 Jaeger, V. W. & Pfaendtner, J. Structure, Dynamics, and Activity of Xylanase Solvated in Binary Mixtures of Ionic Liquid and Water. *ACS Chemical Biology* **8**, 1179-1186 (2013).
113 Figueiredo, A. M., Sardinha, J., Moore, G. R. & Cabrita, E. J. Protein destabilisation in ionic liquids: the role of preferential interactions in denaturation. *Phys. Chem. Chem. Phys.* **15**, 19632-19643 (2013).
114 Nordwald, E. M., Armstrong, G. S. & Kaar, J. L. NMR-Guided Rational Engineering of an Ionic-Liquid-Tolerant Lipase. *ACS Catal.* **4**, 4057-4064 (2014).
115 Brandt, A., Grasvik, J., Hallett, J. P. & Welton, T. Deconstruction of lignocellulosic biomass with ionic liquids. *Green Chem.* **15**, 550-583 (2013).
116 Li, C., Knierim, B., Manisseri, C., Arora, R., Scheller, H. V., Auer, M., Vogel, K. P., Simmons, B. A. & Singh, S. Comparison of dilute acid and ionic liquid pretreatment of switchgrass: Biomass recalcitrance, delignification and enzymatic saccharification. *Bioresource Technology* **101**, 4900-4906 (2010).
117 Fujita, K., Forsyth, M., MacFarlane, D. R., Reid, R. W. & Eiliott, G. D. Unexpected improvement in stability and utility of cytochrome c by solution in biocompatible ionic liquids. *Biotechnol. Bioeng.* **94**, 1209-1213 (2006).
118 Micaelo, N. M. & Soares, C. M. Protein structure and dynamics in ionic liquids. Insights from molecular dynamics simulation studies. *Journal of Physical Chemistry B* **112**, 2566-2572 (2008).
119 Rencurosi, A., Lay, L., Russo, G., Prosperi, D., Poletti, L. & Caneva, E. HRMAS NMR analysis in neat ionic liquids: a powerful tool to investigate complex organic molecules and monitor chemical reactions. *Green Chem.* **9**, 216-218 (2007).
120 Mrestani-Klaus, C., Richardt, A., Wespe, C., Stark, A., Humpfer, E. & Bordusa, F. Structural Studies on Ionic Liquid/Water/Peptide Systems by HR-MAS NMR Spectroscopy. *ChemPhysChem* **13**, 1836-1844 (2012).
121 Richardt, A., Mrestani-Klaus, C. & Bordusa, F. Impact of ionic liquids on the structure of peptides proved by HR-MAS NMR spectroscopy. *J. Mol. Liq.* **192**, 9-18 (2014).

122 Elbayed, K., Dillmann, B., Raya, J., Piotto, M. & Engelke, F. Field modulation effects induced by sample spinning: application to high-resolution magic angle spinning NMR. *J. Magn. Reson.* **174**, 2-26 (2005).
123 Gronenborn, A., Filpula, D., Essig, N., Achari, A., Whitlow, M., Wingfield, P. & Clore, G. A novel, highly stable fold of the immunoglobulin binding domain of streptococcal protein G. *Science* **253**, 657-661 (1991).
124 Dzyuba, S. V., Kollar, K. D. & Sabnis, S. S. Synthesis of imidazolium room-temperature ionic liquids. Exploring green chemistry and click chemistry paradigms in undergraduate organic chemistry laboratory. *J. Chem. Educ.* **86**, 856-858 (2009).
125 Dzyuba, S. V. & Bartsch, R. A. Efficient synthesis of 1-alkyl(aralkyl)-3-methyl(ethyl)imidazolium halides: Precursors for room-temperature ionic liquids. *J. Heterocycl. Chem.* **38**, 265-268 (2001).
126 Franks, W. T., Zhou, D. H., Wylie, B. J., Money, B. G., Graesser, D. T., Frericks, H. L., Sahota, G. & Rienstra, C. M. Magic-angle spinning solid-state NMR spectroscopy of the beta 1 immunoglobulin binding domain of protein G (GB1): N-15 and C-13 chemical shift assignments and conformational analysis. *J. Am. Chem. Soc.* **127**, 12291-12305 (2005).
127 Wilton, D. J., Tunnicliffe, R. B., Kamatari, Y. O., Akasaka, K. & Williamson, M. P. Pressure-induced changes in the solution structure of the GB1 domain of protein G. *Proteins: Structure, Function, and Bioinformatics* **71**, 1432-1440 (2008).
128 Idiyatullin, D., Nesmelova, I., Daragan, V. A. & Mayo, K. H. Heat Capacities and a Snapshot of the Energy Landscape in Protein GB1 from the Pre-denaturation Temperature Dependence of Backbone NH Nanosecond Fluctuations. *J. Mol. Biol.* **325**, 149-162 (2003).
129 Tomlinson, J. H. & Williamson, M. P. Amide temperature coefficients in the protein G B1 domain. *J. Biomol. NMR* **52**, 57-64 (2012).
130 Frank, M. K., Clore, G. M. & Gronenborn, A. M. Structural and dynamic characterization of the urea denatured state of the immunoglobulin binding domain of streptococcal protein G by multidimensional heteronuclear NMR spectroscopy. *Protein Sci.* **4**, 2605-2615 (1995).
131 Kelly, A. E., Ou, H. D., Withers, R. & D√∂tsch, V. Low-Conductivity Buffers for High-Sensitivity NMR Measurements. *J. Am. Chem. Soc.* **124**, 12013-12019 (2002).
132 Kukic, P., O'Meara, F., Hewage, C. & Erik Nielsen, J. Coupled effect of salt and pH on proteins probed with NMR spectroscopy. *Chemical Physics Letters* **579**, 114-121 (2013).
133 Williamson, M. P. Using chemical shift perturbation to characterise ligand binding. *Prog. Nucl. Mag. Res. Sp.* **73**, 1-16 (2013).
134 Alexander, P., Fahnestock, S., Lee, T., Orban, J. & Bryan, P. Thermodynamic analysis of the folding of the streptococcal protein-g igg-binding domains b1 and b2 - why small proteins tend to have high denaturation temperatures. *Biochemistry* **31**, 3597-3603 (1992).
135 Chiu, H. P., Kokona, B., Fairman, R. & Cheng, R. P. Effect of Highly Fluorinated Amino Acids on Protein Stability at a Solvent-Exposed Position on an Internal Strand of Protein G B1 Domain. *J. Am. Chem. Soc.* **131**, 13192-13193 (2009).

136 Yao, J., Dyson, H. J. & Wright, P. E. Chemical shift dispersion and secondary structure prediction in unfolded and partly folded proteins. *FEBS Lett.* **419**, 285-289 (1997).
137 Warner, L., Gjersing, E., Follett, S. E., Elliott, K. W., Dzyuba, S. V. & Varga, K. The effects of high concentrations of ionic liquid on GB1 protein structure and dynamics probed by high-resolution magic-angle-spinning NMR spectroscopy. *Biochem Biophys Rep* **8**, 75-80 (2016).
138 Qiu, L., Wang, Y., Wang, J., Zhang, F. & Ma, J. Expression of biologically active recombinant antifreeze protein His-MpAFP149 from the desert beetle (Microdera punctipennis dzungarica) in Escherichia coli. *Molecular biology reports* **37**, 1725-1732 (2010).
139 Bar, M., Bar-Ziv, R., Scherf, T. & Fass, D. Efficient production of a folded and functional, highly disulfide-bonded beta-helix antifreeze protein in bacteria. *Protein expression and purification* **48**, 243-252 (2006).
140 de Marco, A. Strategies for successful recombinant expression of disulfide bond-dependent proteins in Escherichia coli. *Microbial cell factories* **8**, 26 (2009).
141 Stewart, E. J., Aslund, F. & Beckwith, J. Disulfide bond formation in the Escherichia coli cytoplasm: an in vivo role reversal for the thioredoxins. *Embo Journal* **17**, 5543-5550 (1998).
142 Selenko, P. & Wagner, G. Looking into live cells with in-cell NMR spectroscopy. *Journal of structural biology* **158**, 244-253 (2007).
143 Ulrich, E. L., Akutsu, H., Doreleijers, J. F., Harano, Y., Ioannidis, Y. E., Lin, J., Livny, M., Mading, S., Maziuk, D., Miller, Z., Nakatani, E., Schulte, C. F., Tolmie, D. E., Kent Wenger, R., Yao, H. & Markley, J. L. BioMagResBank. *Nucleic Acids Res.* **36**, D402-D408 (2008).
144 Delaglio, F., Grzesiek, S., Vuister, G. W., Zhu, G., Pfeifer, J. & Bax, A. NMRPipe: A multidimensional spectral processing system based on UNIX pipes. *J. Biomol. NMR* **6**, 277-293 (1995).
145 Vranken, W. F., Boucher, W., Stevens, T. J., Fogh, R. H., Pajon, A., Llinas, M., Ulrich, E. L., Markley, J. L., Ionides, J. & Laue, E. D. The CCPN data model for NMR spectroscopy: Development of a software pipeline. *Proteins: Structure, Function, and Bioinformatics* **59**, 687-696 (2005).
146 Goddard, D. t. & Kneller, D. G. *Sparky 3.*
147 Schumann, F. H., Riepl, H., Maurer, T., Gronwald, W., Neidig, K.-P. & Kalbitzer, H. R. Combined chemical shift changes and amino acid specific chemical shift mapping of protein–protein interactions. *J. Biomol. NMR* **39**, 275-289 (2007).
148 Kay, L. E., Torchia, D. A. & Bax, A. Backbone dynamics of proteins as studied by nitrogen-15 inverse detected heteronuclear NMR spectroscopy: application to staphylococcal nuclease. *Biochemistry* **28**, 8972-8979 (1989).
149 Abragam, A. *Principles of Nuclear Magnetism*. (Clarendon Press, 1961).
150 Lipari, G. & Szabo, A. Model-free approach to the interpretation of nuclear magnetic resonance relaxation in macromolecules. 1. Theory and range of validity. *J. Am. Chem. Soc.* **104**, 4546-4559 (1982).
151 Lipari, G. & Szabo, A. Model-free approach to the interpretation of nuclear magnetic resonance relaxation in macromolecules. 2. Analysis of experimental results. *J. Am. Chem. Soc.* **104**, 4559-4570 (1982).

152 Cavanagh, J., Fairbrother, W. J., Palmer, A. G., Rance, M. & Skelton, N. J. *Protein NMR Spectroscopy: Principles and Practice*. (Elsevier, 2007).
153 Walsh, J. D., Meier, K., Ishima, R. & Gronenborn, A. M. NMR Studies on Domain Diffusion and Alignment in Modular GB1 Repeats. *Biophys. J.* **99**, 2636-2646 (2010).
154 Andersen, N. H., Neidigh, J. W., Harris, S. M., Lee, G. M., Liu, Z. H. & Tong, H. Extracting information from the temperature gradients of polypeptide NH chemical shifts .1. The importance of conformational averaging. *J. Am. Chem. Soc.* **119**, 8547-8561 (1997).
155 Baxter, N. J. & Williamson, M. P. Temperature dependence of H-1 chemical shifts in proteins. *J. Biomol. NMR* **9**, 359-369 (1997).